

Analyses of Quasar 3C 273 using *XMM–Newton* and RXTE

Dissertation
zur Erlangung des Grades eines
Doktors der Naturwissenschaften
der Fakultät für Mathematik und Physik
der Eberhard-Karls-Universität Tübingen

vorgelegt von

Martin Stuhlinger

aus Pforzheim
2004

Selbstverlegt von: M. Stuhlinger
Calle del Parque de Eugenia de Montijo 62 III E
E-28047 Madrid

Tag der mündlichen Prüfung: 02. Dezember 2004

Dekan: Prof. Dr. P. Schmid
1. Berichterstatter: Prof. Dr. R. Staubert
2. Berichterstatter: Prof. Dr. T. J.-L. Courvoisier

Zusammenfassung

Aufgrund ihrer gewaltigen Leuchtkraft über bis zu dreizehn Größenordnungen im Frequenzbereich gehören Kerne aktiver Galaxien (AGN) zu den am weitesten entfernten Einzelobjekten, die im Universum beobachtet werden können. Außer der Einteilung in radiolaute und radioleise AGNs, abhängig von der An- oder Abwesenheit eines Jets, erklärt das Vereinheitlichungsmodell die unterschiedlichen phänomenologischen Erscheinungen von AGNs mit einem unterschiedlichen Blickwinkel auf ein und dieselbe physikalische Objektklasse.

Als hellster und nächststehender Quasar ist 3C 273 ein ideales Objekt für das Studium von Kernen aktiver Galaxien. Er ist über die letzten 30 Jahre häufig in allen Wellenlängenbereichen beobachtet worden. 3C 273 war ebenfalls Beobachtungsobjekt für den europäischen Röntgensatelliten XMM-Newton. Die Beobachtungsergebnisse von einem der Hauptinstrumente, der EPIC Kamera, sind in dieser Arbeit zusammengefasst. Die EPIC Kamera bietet eine Energieauflösung $E/\Delta E$ von etwa 20–50 in einem Energiebereich von 0.1–12 keV. Gleichzeitige oder zumindest nahezu gleichzeitige Beobachtungen mit dem NASA-Satelliten RXTE ermöglichen eine Ausweitung des betrachteten Energiebereichs zu höheren Energien von etwa 100 keV.

Der Kalibrationsvergleich zwischen den EPIC-Detektoren PN und MOS2 sowie derjenige zwischen EPIC PN und RXTE PCA zeigt eine gute spektrale Übereinstimmung aller Detektoren. Die geringen Unterschiede in den gemessenen Flüßen können nachvollzogen werden.

Zunächst wurde der hohe Energiebereich $E > 2.5$ keV ausgewertet. Die entsprechenden Spektren können gut durch ein einzelnes absorbiertes Potenzgesetzmodell beschrieben werden. Die Potenzgesetzindizes variieren im Bereich von $\Gamma = 1.60 - 1.79$, die 3–10 keV Flüße zwischen $6.2 - 9.5 \cdot 10^{-11} \text{ erg cm}^{-2} \text{ s}^{-1}$. Die durchschnittliche Spektralneigung zwischen 2000–2001 ist signifikant härter als diejenige zwischen 2002–2003. Zwischen den Variabilitäten von Potenzgesetzindizes und 3–10 keV Flüßen können keine Verbindungen gefunden werden.

Alle XMM–Newton Beobachtungen zeigen bei Energien unterhalb von etwa 2 keV ein Übermaß an Strahlung bezogen auf das absorbierte einfache Potenzgesetzmodell, einen sogenannten Soft Excess. Für die Untersuchungen der Soft Excess Komponente wurden die Parameter des Potenzgesetzes, welches im hochenergetischen Bereich gefunden wurden, festgehalten. Weder ein zweites Potenzgesetzmodell noch ein zusätzliches einfaches Schwarzkörperstrahlungsmodell einer Akkretionsscheibe ermöglichen eine zufriedenstellende Beschreibung der Soft Excess Komponente.

Für eine systematische Untersuchung aller Beobachtungen wird das absorbierte doppelte Potenzgesetzmodell verwendet. Es wird gezeigt, dass es keine Verbindungen zwischen den Parametern der Soft Excess Komponente und den Parametern der hochenergetischen Potenzgesetzkomponente gibt, was andeutet, dass die beiden Komponenten unabhängig und folglich die entsprechenden Emissionsgebiete unterschiedlich sind. Die Diskussion schließt daraus, dass die Soft Excess Komponente nicht das hochenergetische Ende der UV Komponente des Big Blue Bump ist, welcher mit der Emission einer Akkretionsscheibe um das supermassive Schwarze Loch im Zentrum des Quasars gedeutet wird.

Abstract

Due to their tremendous luminosity over up to thirteen orders of magnitudes in frequency, active galactic nuclei (AGN) belong to the most distant discrete objects that can be observed in the universe. Except the differentiation into radio quiet AGNs and radio loud AGNs, dependent on the presence or absence of a jet, the unification model explains the different phenomenonal appearances of AGNs by a different viewing angle on the same physical kind of objects.

As the brightest and nearest quasar, 3C 273 is the ideal object for studying active galactic nuclei. It has been frequently observed in all wavelengths for the last 30 years. 3C 273 was also an observation object for the European X-ray satellite mission XMM–Newton. The results using one of its main instruments, the EPIC camera, are summarised in this thesis. The EPIC camera provides an energy resolution of $E/\Delta E$ about 20–50 in the energy range of 0.1–12 keV. Simultaneous or at least quasi-simultaneous observations using the NASA satellite RXTE enable the extension of the analysed energy range to higher energies of about 100 keV.

The cross calibration between the EPIC detectors PN and MOS2 as well as the one between EPIC PN and RXTE PCA show that all detectors are in very good spectral agreement. The small differences in the measured fluxes are understood.

First the high energy range of $E > 2.5$ keV is analysed. The corresponding X-ray spectra are well described by an absorbed single power law model. The power law indices vary in the range from $\Gamma = 1.60 - 1.79$, the 3–10 keV fluxes are between $6.2 - 9.5 \cdot 10^{-11}$ erg cm⁻²s⁻¹. The average spectral slope between 2000–2001 is significantly harder than the one between 2002–2003. No correlation in the variabilities of the power law indices and the 3–10 keV fluxes are found.

All XMM–Newton observations show an excess of emission with respect to the single power law model at energies lower than about 2 keV, called soft excess. For the analyses of this soft excess component the power law parameters found in the high energy regime are fixed. Neither a second power law model nor an additional

simple disk blackbody model enable a satisfying fit of the soft excess component.

For a systematic analyses of all observations the absorbed double power law model is used. It is shown that there are no correlations between the parameters of the soft excess component and the parameters of the high energy power law component, indicating that the two components are independent, thus the corresponding emission regions are different. The discussion concludes that the soft excess component is not the high energy end of the big blue bump component seen in the UV which is associated with the emission of the accretion disk around the super massive black hole in the center of the quasar.

Contents

Zusammenfassung	3
Abstract	5
1 Introduction	13
1.1 The AGN Phenomenon	13
1.2 AGN Classifications	14
1.2.1 Seyfert Galaxies	14
1.2.2 Radio Galaxies	15
1.2.3 Quasars	15
1.2.4 Blazars	16
1.3 The Unification Model	16
1.4 The Quasar 3C 273	18
2 The Satellites	22
2.1 XMM–Newton	22
2.1.1 X–ray telescopes	24
2.1.2 EPIC	25
2.1.3 RGS	29
2.1.4 Optical Monitor	30
2.2 RXTE	30
2.2.1 PCA	31
2.2.2 HEXTE	33
3 The Data Processing	35
3.1 XMM EPIC Data	35
3.1.1 Data selection	38
3.2 RXTE Data	42

4	Results of Spectral Analysis	44
4.1	The Spectra Above 2.5 keV	45
4.1.1	RXTE PCA	46
4.1.2	RXTE HEXTE	47
4.1.3	XMM EPIC	48
4.1.4	Simultaneous Observations of RXTE and XMM	51
4.1.5	Fe-Line	52
4.2	Soft Excess	57
5	Variability	61
5.1	Light Curves	61
5.1.1	Short Time Scales	61
5.1.2	Long Time Scales	69
5.2	Spectral Variability	72
5.2.1	Hard Component above 2.5 keV	72
5.2.2	Fe-Line	74
5.2.3	Soft Excess	74
6	Discussion	77
6.1	The power law component >2.5 keV	77
6.2	The Fe-Line	80
6.3	The soft excess	84
6.4	Origin of the X-ray emission	89
A	RXTE Spectra	93
B	XMM spectra	103
	References	130
	Acknowledgements	135
	Curriculum vitae	136

List of Figures

1.1	Optical spectrum of Seyfert I galaxy NGC 5548	14
1.2	Unified model of AGNs	17
1.3	Optical spectrum of 3C 273	19
1.4	Average spectrum of 3C 273	20
2.1	Sketch of XMM–Newton.	23
2.2	Picture of a mirror module.	25
2.3	Picture of the PN chip.	27
2.4	Picture of the MOS CCD array.	28
2.5	Picture of the RGA.	29
2.6	Schematic representation of RXTE.	32
3.1	PN source and background regions.	38
3.2	Example of a pattern distribution provided by SAS task EPATPLOT.	39
3.3	Example for GTI selection.	41
4.1	Contour plot I–E of Fe–line in MOS2 obs. 0126700701.	45
4.2	RXTE spectra of observation 2000-06-14.	47
4.3	The PN spectrum (2.5-10 keV) of observation 2000-06-14.	49
4.4	Cross calibration of EPIC PN and MOS2.	50
4.5	Cross calibration of RXTE PCA and XMM EPIC PN.	51
4.6	Obs. 2000-06-16: Possible signature of an Fe–Line.	54
4.7	Contour plot σ –E of Fe–line in MOS2 obs. 0126700701.	55
4.8	Obs. 2000-06-16: Ratios of un-binned MOS/PN spectra between 5.0–6.5 keV.	56
4.9	Obs. 2001-06-13: The 0.3–10 keV PN spectrum.	58
5.1	The 2000 June light curves of two energy bands.	63
5.2	Example of short time scale variability.	65
5.3	Source variability at frequencies $< 10^{-4}$ Hz.	66
5.4	Structure functions of 2000 June light curve.	68
5.5	The long term variability of 3C 273.	70
5.6	Variability of soft power law component.	71
5.7	Variability of hard power law component.	73
5.8	Spectral variability of soft excess component.	75

6.1	Flux versus power law indices for spectra >2.5 keV.	79
6.2	Development of the hard X-ray power law index for 3C 273. . .	81
6.3	Discussion of Fe-line feature in 3C 273 PCA spectra.	82
6.4	Correlation of fluxes versus power law indices of the soft excess model parameters.	86
6.5	Correlations between the soft and hard band parameters.	87
6.6	Correlation of power law index and logarithm of the photon flux ratio.	91
A.1	RXTE spectra of observation 2000-06-14.	94
A.2	RXTE spectra of observation 2001-06-13.	95
A.3	RXTE spectra of observation 2001-12-16.	96
A.4	RXTE spectra of observation 2001-12-21+23.	97
A.5	RXTE spectra of observation 2002-01-09.	98
A.6	RXTE spectra of observation 2003-01-05.	99
A.7	RXTE spectra of observation 2003-06-16.	100
A.8	RXTE spectra of observation 2003-07-21.	101
A.9	RXTE spectra of observation 2004-01-01.	102
B.1	PN/MOS2 spectra (2.5–10.0 keV) of obs. 2000-06-14.	104
B.2	PN soft excess characterisations of obs. 2000-06-14.	105
B.3	PN/MOS2 spectra (2.5–10.0 keV) of obs. 2000-06-15.	106
B.4	PN soft excess characterisations of obs. 2000-06-15.	107
B.5	PN/MOS2 spectra (2.5–10.0 keV) of obs. 2000-06-16.	108
B.6	PN soft excess characterisations of obs. 2000-06-16.	109
B.7	PN/MOS2 spectra (2.5–10.0 keV) of obs. 2000-06-18.	110
B.8	PN soft excess characterisations of obs. 2000-06-18.	111
B.9	PN/MOS2 spectra (2.5–10.0 keV) of obs. 2001-06-13.	112
B.10	PN soft excess characterisations of obs. 2001-06-13.	113
B.11	PN/MOS2 spectra (2.5–10.0 keV) of obs. 2001-12-16.	114
B.12	PN soft excess characterisations of obs. 2001-12-16.	115
B.13	PN/MOS2 spectra (2.5–10.0 keV) of obs. 2001-12-22.	116
B.14	PN soft excess characterisations of obs. 2001-12-22.	117
B.15	PN/MOS2 spectra (2.5–10.0 keV) of obs. 2002-01-09.	118
B.16	PN soft excess characterisations of obs. 2002-01-09.	119
B.17	PN/MOS2 spectra (2.5–10.0 keV) of obs. 2002-07-07.	120
B.18	PN soft excess characterisations of obs. 2002-07-07.	121
B.19	PN/MOS2 spectra (2.5–10.0 keV) of obs. 2000-12-17.	122
B.20	PN soft excess characterisations of obs. 2002-12-17.	123
B.21	PN/MOS2 spectra (2.5–10.0 keV) of obs 2003-01-05.	124
B.22	PN soft excess characterisations of obs. 2003-01-05.	125
B.23	PN/MOS2 spectra (2.5–10.0 keV) of obs. 2003-01-05.	126

B.24	PN soft excess characterisations of obs. 2003-01-05.	127
B.25	PN/MOS2 spectra (2.5–10.0 keV) of obs. 2003-07-08.	128
B.26	PN soft excess characterisations of obs. 2003-07-08.	129

List of Tables

2.1	Basic characteristics of the XMM instruments.	24
2.2	Basic characteristics of the RXTE instruments.	31
3.1	Summary of XMM observations of 3C 273.	35
3.2	Summary of RXTE observations of 3C 273.	42
4.1	Fit results for PCA spectra.	46
4.2	Fit results for EPIC spectra $E = 2.5\text{--}10.0$ keV.	48
4.3	Upper limits (3σ) of narrow or broad Fe $K\alpha$ line.	53
4.4	Fit results for spectra $0.3 > E > 2.5$ keV.	59
5.1	Average count rates of individual EPIC PN light curves from 2000 June.	62
A.1	The energy ranges of HEXTE spectra.	93

CHAPTER 1

Introduction

1.1 The AGN Phenomenon

Active Galactic Nuclei (AGN) belong to the most impressive objects in the sky. Inside a tiny volume they produce amazing luminosities from $\sim 10^{42}$ – 10^{48} erg s⁻¹, in some cases as much as 10 000 times the luminosity of a typical galaxy. The radiation is produced over a very broad range of frequencies, with the luminosity per logarithmic frequency interval roughly constant (within a factor of several) across up to thirteen orders of magnitude in frequency. As an example the broadband spectrum of 3C 273 is presented in Fig. 1.4. Because of their high luminosity AGN are the most distant discrete objects that can be observed.

About 3% of all galaxies are classified as AGN (Collmar 2001). Although there is no overall agreement about a precise definition of active galaxies, a galaxy is called ‘active’ if it shows one or more of the following characteristics:

- Compact galactic core, brighter than in galaxies of the same type.
- Strong narrow and/or broad emission lines, usually redshifted.
- High luminosity.
- Non-thermal, non-stellar continuum emission.
- Radio emission from lobes or jets.
- Variability of the continuum and the emission lines.

1.2 AGN Classifications

1.2.1 Seyfert Galaxies

In his publication Seyfert (1943) summarized six spiral galaxies revealing unusual emission lines in their optical spectra. These galaxies also contain high surface brightness nuclei that look like normal distant galaxies with a star superimposed on the center. The definition has evolved so that Seyfert galaxies are now identified spectroscopically by the presence of strong, high-ionization emission lines.

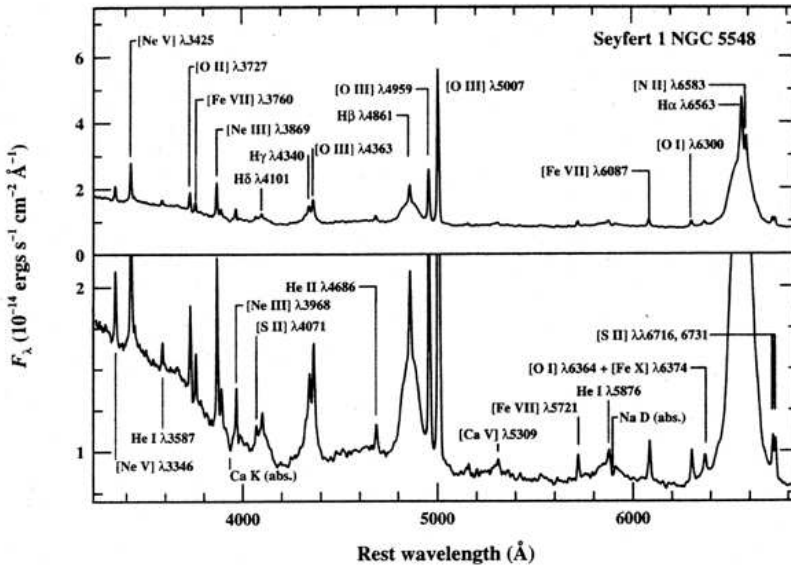


Figure 1.1: Optical spectrum of Seyfert I galaxy NGC 5548: broad lines and narrow lines are superposed (Peterson 1997).

Khachikian & Weedman (1974) were the first to realize that there are two distinct subclasses of Seyfert galaxies. Seyfert I galaxies have two sets of emission lines, superposed on one another. The first set lines have widths corresponding to velocities of several hundred kilometers per second and are referred as narrow lines. The presence of forbidden lines indicates that the emission region is a low-density ionized gas. Next to these narrow lines there are broad lines with a width corresponding to velocities up to 10^4 km s^{-1} , but in permitted lines only indicating that the emitting gas is of high density, so the non-electric dipole transitions are collisionally suppressed. Seyfert II galaxies differ from Seyfert I galaxies in that only narrow lines are present

in the spectra.

The two sets of lines are explained by two different emission regions. According to the different line widths they are called broad line region (BLR) and narrow line region (NLR). The BLR is assumed to be very close (~ 1 pc) to the center of the AGN. Clouds of ionized gas are moving with typical velocities of 10^4 km s $^{-1}$. Due to these high velocities the lines are broadened by the Doppler effect. In a distance of about 100 pc there is the NLR with clouds of ionized gas moving at lower velocities. Therefore the lines are less broadened by the Doppler effect than in the BLR. It is assumed that in Seyfert I galaxies both the NLR and the BLR can be observed directly, whereas in Seyfert II galaxies the BLR is hidden behind a dust torus and can not be observed. The current model for AGN is described in chapter 1.3.

Osterbrock (1993) has introduced more subclasses to the Seyfert galaxies with the notation Seyfert 1.X. These subclasses are based on the appearance of the optical spectrum. Numerically larger subclasses have weaker broad line components relative to the narrow lines than numerically lower subclasses. E.g. in Seyfert 1.9 galaxies the broad component is detected only in the H α line and not in higher-ordered Balmer lines. In Seyfert 1.8 galaxies, the broad components are very weak, but detectable at H β as well as at H α . In Seyfert 1.5 galaxies the strengths of the broad and narrow components in H β are comparable.

1.2.2 Radio Galaxies

AGNs having high luminosities at radio frequency are classified as radio galaxies. Their optical spectra also indicate two types of radio galaxies: narrow line radio galaxies (NLRGs) and broad line radio galaxies (BLRGs). Radio galaxies are the radio loud analogs of Seyfert I+II galaxies.

Radio galaxies can show an extended, spatially resolved radio morphology and a compact appearance, unresolved at ~ 1 arcsec resolution. Fanaroff & Riley (1974) divided extended radio structures into two classes. Weaker radio sources which are brightest in the center and with decreasing surface brightness towards the edges are called FR I. The more luminous FR II sources are limb-brightened and often show regions of enhanced emission either at the edge of the radio structure or embedded within the structure.

1.2.3 Quasars

The name quasars is a contraction of quasi-stellar radio sources (QSRs). Quasars are the most luminous subclass of AGNs. Historically, quasars have been radio objects.

Their optical counterparts show no nebulosity of a host galaxy but seem to be stellar. Today, using large telescopes the host galaxies of many quasars can be resolved. According to the flux in the radio and infrared quasars are classified as radio loud or radio quiet. Quasar spectra do not differ from spectra of radio or Seyfert galaxies. Usually AGNs with an absolute luminosity greater than $M_V > -23^m$ are called quasars if the objects are radio loud or quasi-stellar objects (QSOs) if they are radio quiet.

1.2.4 Blazars

In general, AGNs show irregular continuum variability at all wavelengths. The notation blazar is used for the subclass of AGNs showing short time variations that are abnormally large. In addition to their large variability in flux, the continuum emission is polarized up to a few percent (as opposed to less than one percent for most AGNs). The polarization also varies in both magnitude and position angle. These sources are always radio loud. Blazars can be sub-divided into:

- Optical Violent Variables (OVVs): Quasars with extreme short time-scale variability at optical wavelengths.
- Highly Polarized Quasars (HPQs): Quasars with highly polarized emission.
- BL-Lacertae objects: AGNs without emission lines, having a highly polarized and very variable continuum emission.

1.3 The Unification Model

The taxonomy of AGNs tends to be rather confusing. Undoubtedly, some of the differences between various types of AGN are more due to the way the objects are observed than to fundamental physics underlying the AGN phenomenon. Except the differentiation into radio quiet AGNs and radio loud AGNs the unification model rests on the assumption that all the different appearances of AGNs are caused by the viewing angle under which these objects of the same physical kind are observed.

Observing short time variations of the AGN continuum emission of the order days or even less, the size of the emitting source region can be derived. Let's assume that the physical conditions of a volume with radius r are changing suddenly. Due to the limited speed of light c the observer will see this transition as a variation with the duration time of $t = 2r/c$. Reversed if a variation of the duration t is observed, the radius of the involved volume r can be estimated to be $r = tc/2$. For AGN this resulting volume is about the size of our solar system. Thermonuclear fusion, the energy

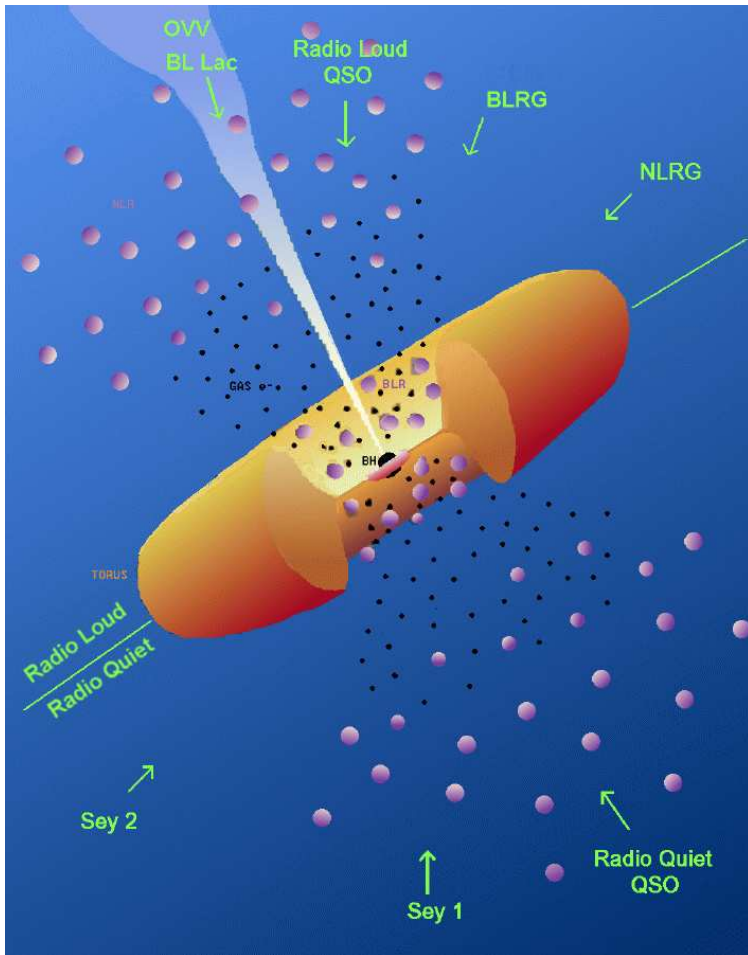


Figure 1.2: Unified model of AGNs: The classification of an AGN depends on the viewing angle to the physically similar objects. Upper half: radio loud; lower half: radio quiet AGNs. Figure from BeppoSAX Calendar 1999, <http://www.asdc.asi.it/bepposax/calendar/>

engine of stars, is not able to explain the production of about 10^{12} times the solar luminosity. The only process known that is able to provide such amounts of energy

inside small volumes is accretion of matter onto a massive black hole. The efficiency of the conversion of rest mass to radiation is about $\eta_{\text{accr}} \sim 10\%$ for accretion, about 10 times higher than the $\eta_{\text{th}} \sim 0.7\%$ efficiency of thermonuclear fusion.

According to the standard model the center of an AGN is a super massive black hole with a mass between 10^7 – 10^9 solar masses, accreting matter from the innermost region of its host galaxy. Because the conservation of angular momentum prohibits the matter to fall directly into the black hole, an accretion disk is formed. The inner radius of the accretion disk is limited by the innermost stable orbit around the black hole at 3 Schwarzschild radii ($R_S = \frac{2GM}{c^2}$) for non-rotating black holes. The outer radius extends to some tens of mpc. The optical and UV continuum of AGN mainly originates from thermal emission of the accretion disk (Shields 1978), in the spectra denoted as the big blue bump. Czerny & Elvis (1987) suggested that the soft X-ray excess of some AGN could be the high-frequency tail of the thermal disk component.

At a distance of about a few tens parsec the BLR is surrounded by a dusty torus. The dimension of the BLR could be derived from the variations of the broad emission lines to be about 0.1 up to a few parsec. At Seyfert II galaxies the torus is in the line of sight between the observer and the BLR, thus covering the BLR and no broad lines are detectable in the spectra. Outside the torus the NLR is located and extends to some hundreds of parsec. There are hints that the NLR emission may be concentrated into two cones which are often aligned with radio structure (Wilson & Baldwin 1989).

1.4 The Quasar 3C 273

According to its name, 3C 273 was discovered in the radio sky survey at 158 MHz resulting in the Third Cambridge (3C) catalogue (Edge et al. 1959). Galaxies were found as optical counterparts for several of these radio sources. For 3C 273 the identification proved to be more difficult. The optical image of the most likely candidate in the radio error box was point-like and didn't appear to be a galaxy at all. A moon occultation enabled Hazard et al. (1963) to identify the radio object 3C 273 with a stellar object with an average magnitude of 12.9 in the V band. After 3C 48 this was the second time that a radio source was identified with a stellar object. Moreover, their optical spectra were dominated by emission lines, a fact that greatly puzzled astronomers used to the absorption line spectra of normal galaxies. The measured wavelengths were not even close to any familiar line energy, and optical astronomers had only few clues about what kind of object they might be. This new class of objects was named quasars, a contraction of quasi-stellar radio sources.

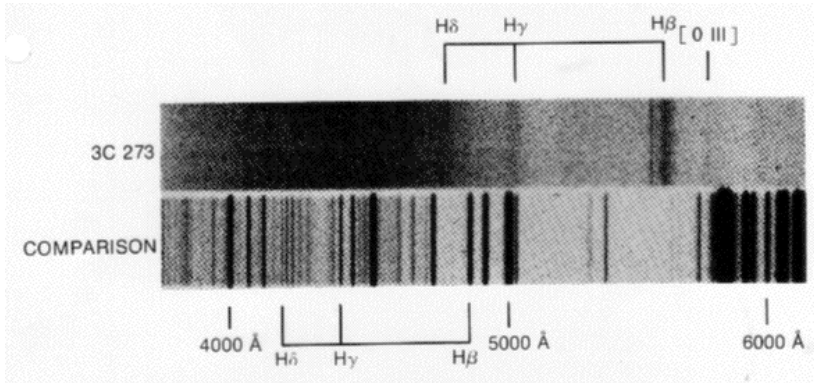


Figure 1.3: Optical spectrum of 3C 273: Maarten Schmidt identified redshifted Hydrogen Balmer lines (Greenstein & Schmidt 1964).

The mystery was cleared up in 1963. Analyzing the optical spectrum of 3C 273 Maarten Schmidt noticed that the wavelength distances between certain emission lines were the same as between the Hydrogen Balmer lines H_β , H_γ and H_δ (Fig. 1.3). If this correspondence was interpreted to be cosmological in origin, the resulting redshift of 3C 273 was $z = \frac{\lambda - \lambda_0}{\lambda_0} = 0.158$. Using this redshift Schmidt identified other lines like MgII and the forbidden line [OIII] (Schmidt 1963; Greenstein & Schmidt 1964).

As the brightest and nearest quasar, 3C 273 is the ideal laboratory for studying active galactic nuclei. It has been frequently observed in all wavelengths for the last 30 years. Türler et al. (1999b) published the average broad band spectrum of 3C 273 derived out of a database of nearly 20 000 observations covering 16 orders of magnitude in frequency from radio to the γ -ray domain. In Fig. 1.4 the average spectrum of 3C 273 is presented. The broad spectral energy distribution (SED) of the quasar continuum can be characterized crudely as a power law $F_\nu = C\nu^{-\alpha}$, where α is the spectral index, C is a constant, and F_ν is the spectral flux usually in units of Jansky [$1 \text{ Jy} = 10^{-23} \text{ ergs cm}^{-2} \text{ s}^{-1} \text{ Hz}^{-1}$]. The lower panel shows the νF_ν versus $\log \nu$ representation. In this case the power law distribution becomes $\nu F_\nu \sim \nu^{1-\alpha}$, so that the case $\alpha = 1$, equal energy per unit logarithmic frequency interval, is a horizontal line in the diagram. This is the preferred unit for examining where the quasar energy is emitted as it reflects the amount of energy emitted in each equally spaced interval on the logarithmic frequency axis.

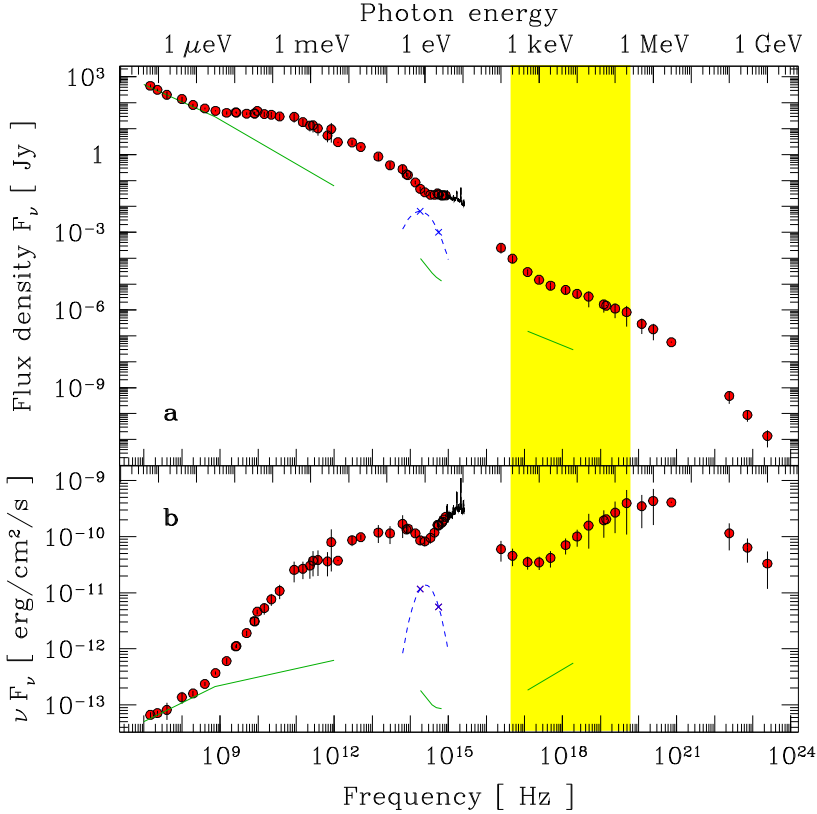


Figure 1.4: Average spectrum of 3C 273 derived out of the 3C 273 data base (Türler et al. 1999b). Solid line: contribution of the jet; dashed line: contribution of the host galaxy. The highlighted frequency region represents the energy range covered by XMM and RXTE observations used in this work.

The νF_ν representation in the lower panel demonstrates that the luminosity per logarithmic interval is nearly constant over more than 10 decades of frequency. There are two maxima at roughly the same level, one in the far ultraviolet, the big blue bump, and the other at about 1 MeV. The relatively small error-bars show that the variability of 3C 273 does not basically change its overall spectral shape. The solid line is the contribution of the jet, the dashed line is the contribution from the host galaxy suggested by a parabola in νF_ν , which is normalised by the H and V band contributions (crosses, Türler et al. (1999b)). The highlighted frequency region represents the en-

ergy range covered by XMM and RXTE observations used in this work.

Combining four emission mechanisms, the main characteristics of the overall spectral shape can be reproduced:

- Radio: The radio emission is dominated by the non-thermal emission of the jet. Electrons moving in a magnetic field are emitting synchrotron radiation.
- Infrared: Thermal radiation of a warm dusty disk which is heated by the central source.
- Op./UV: Thermal emission of the accretion disk and its hot corona is responsible for the big blue bump.
- X/ γ -ray: Relativistic electrons in an accretion disk corona interact with photons from synchrotron radiation and the optical/UV photons of the accretion disk corona. These photons are scattered to X/ γ -rays using the inverse Compton effect.

The time scales of the variation are different for radio, optical/UV and X-ray fluxes. Correlations of the variability between these frequency bands have not been found so far, indicating that the emitting regions are different.

CHAPTER 2

The Satellites

2.1 XMM–Newton

The X–ray Multi–Mirror mission (XMM), a ‘Cornerstone Mission’ in the *Horizon 2000 Programme* of the European Space Agency (ESA), was launched on 1999 December 09th, the first commercial launch of Ariane-5. The primary scientific objective of XMM is to perform high throughput spectroscopy of cosmic X–ray sources over a broad band of energies ranging from 0.1 keV to 10 keV. The secondary objective is the imaging of faint source populations and detection of extended emission.

The observatory consists of three coaligned high throughput 7.5 m focal length telescopes with 6” FWHM¹ (15” HEW²) angular resolution. XMM–Newton provides images over a 30’ field of view with moderate spectral resolution using the European Photon Imaging Camera (EPIC), which consists of two MOS and one PN CCD arrays. High–resolution spectral information ($E/dE \sim 300$) is provided by the Reflection Grating Spectrometer (RGS) that deflects half of the beam on two of the X–ray telescopes. The two telescopes equipped with the Reflecting Grating Arrays (RGA) have the EPIC MOS cameras as focal instruments, whereas the EPIC PN is placed at the focal plane of the third telescope without gratings. The instrumentation is completed by an optical/UV monitor using an own telescope.

The basic characteristics of the XMM–Newton mission are:

- Having a mirror geometric effective area of 1550 cm² at 1 keV energy per mirror module, XMM–Newton carries the X–ray telescopes with the largest effective area for a focusing telescope ever.

¹Full width at half maximum.

²Half energy width.

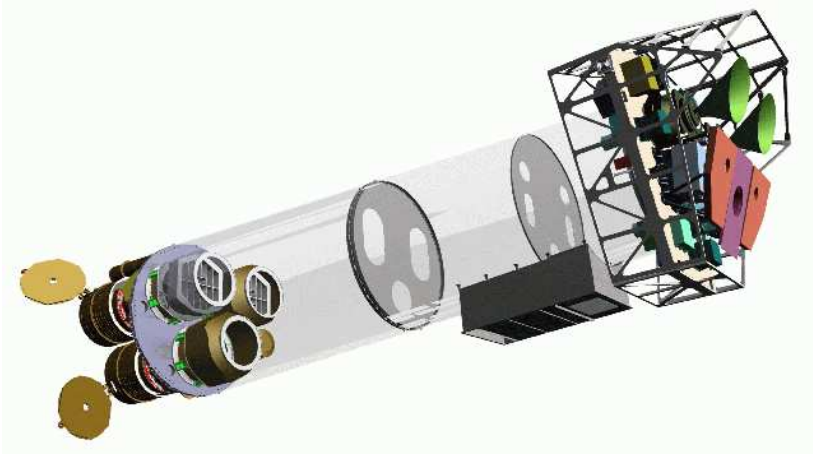


Figure 2.1: Sketch of XMM–Newton. Figure of Dornier Satellitensysteme GmbH. The mirror modules are on the left side, the instruments are on the right side.

- All six scientific instruments operate simultaneously and independently, if not prohibited by target brightness constraints.
- The 58 thin nested mirror shells in each telescope enable XMM–Newton a good angular resolution with a FWHM on the order of $6''$.
- The EPIC CCD cameras have moderate spectral resolutions ($E/\Delta E$ about 20–50) in the energy range of 0.1–12 keV. The RGS spectrometers offer much higher spectral resolution ($E/\Delta E$ about 200–800) for the smaller energy range of 0.3–2.5 keV.
- A highly elliptical orbit offers long continuous target visibility of about 40 hours. Due to the telemetry gap near apogee, these 40 hours are split into two periods of about 70 ksec each with a short gap (of about one hour) in between.

The design of the XMM–Newton spacecraft is shown in Fig. 2.1. The mirror modules are visible at the lower left. Two of the three telescopes are equipped with Reflection Grating Arrays (RGA) of the RGS. In the sketch the gratings are the hexagonal structures at the right end of the upper two mirror modules. The optical monitor is hidden by the lower mirror module. Next to the upper mirror module are the star trackers. At the right end of the spacecraft, the focal instruments EPIC MOS, EPIC PN and RGS detectors are shown. The two MOS cameras, sharing their telescopes

with the RGS, are easily identified by the horn radiators. The PN is shown as the box below the MOS cameras, the RGS detectors as the small cubes at the lower end of the detector module. The plain radiators of the RGS detectors are on the left and right side of the PN radiator. Some characteristics of the instrument are summarised in Tab. 2.1.

Table 2.1: Basic characteristics of the XMM instruments.

Instrument	EPIC PN	EPIC MOS	RGS	OM
Bandpass:	0.1–15 keV	0.1–15 keV	0.35–2.5 keV	160–600 nm
Spectral resolution:	57 eV at 1 keV	67 eV at 1 keV	3.2 eV at 1 keV	0.5 nm
Field of view:	30'	30'	~5'	17'
Timing resolution:	1 ms	0.03 ms	16 ms	50 ms

XMM–Newton was launched into a highly elliptical orbit with an inclination of 40 degrees, an apogee of 114,000 km and a perigee of 7,000 km. Due to this orbit, XMM–Newton spends most of its time outside earth's radiation belt. About 40 hours of the 48–hour orbit can be used for scientific observations, with a total target visibility period of approximately 145 ksec per orbit. Note that objects cannot be continuously observed during the entire visibility period due to an apogee telemetry gap. This gap is caused by an interruption of contact during the hand–over between the two ground stations located at Kourou and Perth.

2.1.1 X-ray telescopes

Each of the three X-ray telescopes on board of XMM–Newton consists of 58 Wolter I grazing-incidence mirrors which are highly nested in a coaxial and cofocal configuration. The design of the optics was driven by the requirement of obtaining the highest possible effective area over a wide range of energies, with a particular emphasis in the region around 7 keV (Fe K_{α} line). Thus, the mirror system had to utilize a very shallow grazing angle of 30' in order to provide sufficient reflectivity at high energies. The telescopes' focal length is 7.5 meters and the diameter of the largest mirrors is 70 cm, to be compatible with the shroud of the launcher. Each telescope includes, apart from the mirror modules, baffles for visible and X-ray stray-light suppression and an electron deflector for diverting soft electrons. Two of the telescopes carry a Reflection Grating Array.

Each Mirror Module is a grazing-incidence Wolter I telescope, consisting of 58 gold-coated nested mirrors. Wolter telescopes enable imaging in the X-rays using two grazing incident reflections, the first one at a parabolic mirror and the second one at a hyperbolic mirror. Therefore each mirror shell consists of a paraboloid and an

associated hyperboloid which were replicated together in one piece to facilitate alignment and integration.

In grazing incidence optics the effective area is increased by nesting a number of mirrors and thus filling the front aperture as far as possible. The nesting efficiency is

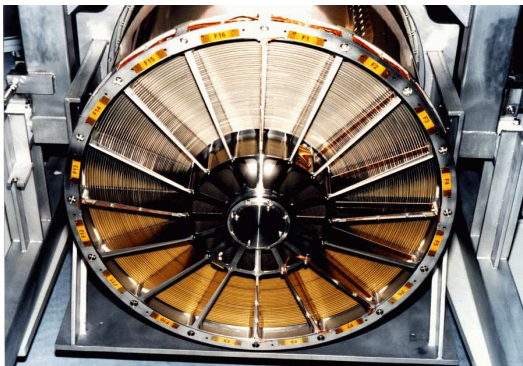


Figure 2.2: Picture of a mirror module with 58 highly-nested Wolter I telescope mirrors.³

order to guarantee sufficient stiffness. The thickness of the 700 mm diameter mirror is 1.07 mm. The minimum radial separation between adjacent shells is 1 mm.

determined by the mirror shell thickness and, in case of very low grazing angles, by the minimum radial mirror separation which is required for integration and alignment. The thinner the mirror shells are and the narrower the shells are spaced, the larger is the collecting area.

The thickness of the smallest mirror (diameter = 306 mm) is 0.47 mm, and it increases linearly with shell diameter in

X-rays from outside the field of view can reach the sensitive area of the focal plane detectors by single reflection from the rear end of the hyperbola, if the source is at an off-axis angle between 20' and 80'. Rays reflected just once from any one of the parabolas cannot leave the mirror assembly because of the close packing of the mirror shells.

The baffles behind the mirror modules reduce the stray light level by a factor of 5 to 10 depending on the position in the focal plane.

2.1.2 EPIC

The EPIC CCDs are designed to exploit the full design range of the X-ray mirrors, 0.1–15 keV. They provide energy resolution at 6.5 keV of $E/dE \sim 50$, and their positional resolution is sufficient to resolve the mirror performance of 6" FWHM (15" HEW). A selection of filters mounted on a wheel in front of each camera allows the

³Photograph of XMM–Newton SOC, VILSPA
(http://xmm.vilspa.esa.es/external/xmm_user_support/documentation/build/mirr_mod_3.shtml)

rejection of long wavelength optical and UV radiation in such a way as to optimize the low energy response of the instrument. A variety of data collection modes is provided which trade imaging performance against timing resolution and maximum count rate. These operational modes are:

- Full frame (MOS and PN): In this mode, all pixels of all CCDs are read out and thus the full FOV is covered. The time resolution for MOS is 2.5 s, for PN 73.4 ms.
- Extended full frame (PN only): Like the full frame mode, but the image collection time is extended to 0.28 s.
- Partial window (MOS): In a partial window mode the central CCD of both MOS cameras can be operated in a different mode of science data acquisition, reading out only part of the CCD chip: in small window mode an area of 100 x 100 pixels (0.4 s) is read out, whereas in large window mode an area of 300 x 300 pixels (0.9 s) is active.
- Partial window (PN): In large window mode only half the area (200×384 pixels) of all 12 CCDs is read out, whereas in small window mode only the part of CCD 0 in quadrant 1 at the focal point is used to collect data. The time resolution is 48 ms for the large window mode and 6 ms for the small window mode, respectively.
- Timing (MOS and PN): In timing mode, imaging is made only in one dimension, along the column axis. Along the row direction, data from a predefined area on one CCD chip are collapsed into a one-dimensional row to be read out at high speed of 1.5 ms for MOS and 0.03 ms for PN.
- Burst (PN only): A special variant of the timing mode of the EPIC PN camera is the burst mode, which offers very high time resolution of 7 μ s.

2.1.2.1 EPIC PN

The EPIC PN detector was built by the Max-Planck-Institut für extraterrestrische Physik (Garching) and Astronomisches Institut Tübingen. It is mounted at the focal plane of one of XMM's three telescopes without a grating spectrometer in the light path.

The PN camera CCDs are new technology, back illuminated and fully depleted X-ray p-n CCDs. X-rays hit the detector from the rear side. In the event of an X-ray interaction with the silicon atoms, electrons and holes are generated in numbers proportional to the energy of the incident photon. The average energy required to form

an electron-hole pair is 3.7 eV at -90°C . The strong electric fields in the PN–CCD detector separate the electrons and holes before they recombine. Signal charges (in our case electrons), are drifted to the potential minimum and stored under the transfer registers. The positively charged holes move to the negatively biased back side, where they are absorbed. The electrons, captured in the potential wells 10 microns below the surface can be transferred towards the readout nodes upon command, conserving the local charge distribution patterns from the ionization process. Each CCD line is terminated by a readout amplifier.

The PN camera consists of twelve (6×2) chips with a size of $3\times 1\text{ cm}$ each, built on a single wafer by the monolithic fabrication. The chip array itself is embedded in an electronics board carrying the camera electronics. The twelve CCDs are ordered into four individual quadrants which are operated in parallel.

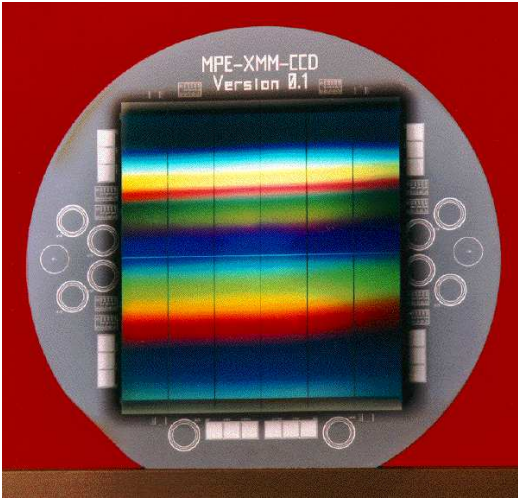


Figure 2.3: Picture of the PN chip.⁴

The CCD array was especially designed for the XMM–Newton X–ray telescope FOV and mirror PSF. It has an imaging area of $6\times 6\text{ cm}$ covering about 97% of the circular FOV, 3% of the FOV is not covered by the quadratic CCD array. About 6 cm^2 of the CCD’s sensitive area are outside the circular FOV and are used for background studies. The pixel size is $150\times 150\text{ microns}$ ($4.1''$) with a position resolution of 120 microns, resulting in an equivalent angular resolving capability for a single photon of $3.3''$. With 64×200 pixels per chip and a total of 12 chips, the PN camera offers a square field of view with a size similar to that of the 7 MOS chips.

⁴Photograph of XMM–Newton SOC, VILSPA
(http://xmm.vilspa.esa.es/external/xmm_user_support/documentation/build/pn_ccd.shtml)

2.1.2.2 EPIC MOS

The MOS camera system is produced by a consortium which includes Leicester University (CCDs and camera head), the University of Birmingham (thermal control system) and CEN Service d’Astrophysique Saclay (control and event recognition electronics).

Each camera consists of an array of 7 front illuminated Metal–Oxide–Silicon (MOS) technology, X-ray-sensitive CCD chips. The central CCD is at the focal point on the optical axis of the telescope while the outer six are stepped towards the mirror by 4.5 mm to follow approximately the focal plane curvature, and improve the focus for off-axis sources. Note that in Fig. 2.4 the vertical offset of the chips with respect to each other is exaggerated.

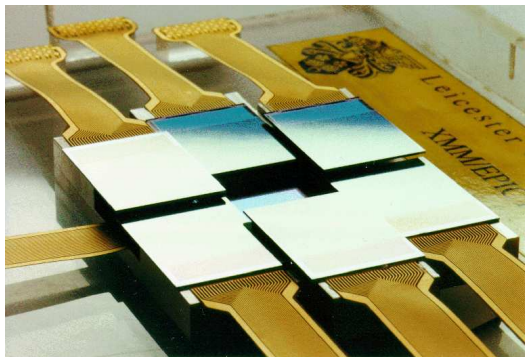


Figure 2.4: Picture of the MOS CCD array.⁵

The CCDs have a dead region of less than 300 microns wide on three sides. To minimise the dead space, neighboring CCDs are stepped by about 1 mm to overlap by 300 microns. The two MOS cameras are arranged on the spacecraft focal plane in a way so that the CCDs are orthogonal. This means that the 300 micron gaps between the outer CCDs in one camera are covered by their opposite numbers in the other camera.

The imaging area of a single CCD is about 2.5×2.5 cm, so that a mosaic of seven covers the focal plane 62 mm in diameter, equivalent to 28.4 arcminutes. The imaging section has 600×600 pixels with size of 40 microns square. One pixel covers 1.1×1.1 arcseconds on the FOV and 15 pixels cover the mirror PSF half energy width of 15 arcseconds.

⁵Photograph of XMM–Newton SOC, VILSPA
(http://xmm.vilspa.esa.es/external/xmm_user_support/documentation/build/mos_array.shtml)

2.1.3 RGS

Reflection Grating Spectrometers (RGS) are included in two of the three XMM–Newton X–ray telescopes, intercepting about 50% of the X–rays passing through the mirrors. The RGS instruments achieve high resolving power of $E/\Delta E=150\text{--}800$ over a range from 5–35 Ångström in the first spectral order. The effective area peaks around 15 Ångström at about 150 cm^2 for the two spectrometers. The gratings of the Reflection Grating Assemblies (RGAs) consist of a silicon carbide substrate coated with 2000 Ångström gold. The gratings are trapezoidally shaped to fill the beam of the telescope. Flatness of the gratings is obtained by 5 stiffening ribs on their backside. The gratings are integrated in a structure which is mounted on the mirror module.

The diffracted X–rays are detected with a strip of CCD detectors, the RGS Focal Cameras (RFCs). The CCD adopts as basic element a $27.97\text{ mm} \times 25.4\text{ mm}$ chip with 27 micron squared pixels. The quantum efficiency of these CCDs is optimized using these in a back illuminated fashion (no absorption of soft X–rays in the gate structure). To suppress optical stray light, each CCD has a thin aluminum layer on top of their backside. A set of

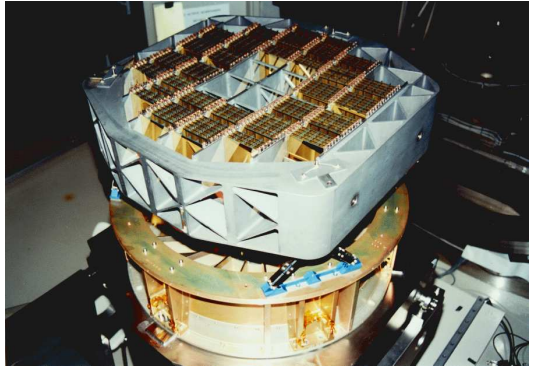


Figure 2.5: Picture of the RGA.⁶

9 of these chips is oriented tangent to the Rowland circle with a cross-dispersion width of about $5'$ and a length that ensures that no emission of an X–ray source at small off-axis angles ($<5'$) is lost off the edges of the array.

The arrays are actually so long that one does not only detect light from the $-1.$ grating order, but also the $-2.$, and depending on the brightness of the source possibly even higher orders. The separation of spectral orders is accomplished by using the energy resolution of the CCDs. In addition this energy resolution provides the means for background suppression since it is required that events have the correct pulse height, corresponding to their spatial position in the spectrum.

⁶Photograph of XMM–Newton SOC, VILSPA
(http://xmm.vilspa.esa.es/external/xmm_user_support/documentation/build/rga.test1.pdf)

2.1.4 Optical Monitor

The XMM Optical Monitor (OM) was built by a consortium of institutes from the UK, the USA and Belgium, led by the PI group at the Department of Space and Climate Physics at the Mullard Space Science Laboratory, part of University College London.

The OM is co-aligned with the X-ray telescopes, providing simultaneous UV, optical and X-ray observations. The instrument consists of a 30 cm Ritchey-Chretien telescope feeding a compact image-intensified photon-counting detector. The low background in space seen by an orbiting observatory gives the Optical Monitor a sensitivity for imaging comparable to that of a 4 m telescope at the earth's surface. Some characteristics of it are summarised in Tab. 2.1.

The detector operates in the UV and the blue region of the optical spectrum. Since the majority of X-ray sources is variable, the optical monitor allows the observers to know the optical state of the X-ray objects they are viewing.

There is a facility for more detailed imaging of the center of the field of view through a $\times 4$ magnifier. The magnifier is carried on one of the filter wheel positions. The spectral range of the telescope with the magnifier selected is fixed at 350–550 nm.

The Optical Monitor can provide spectral resolution by the use of broad- and narrow-band filters contained within a filter wheel, plus two gratings in the filter wheel for low resolution spectroscopy. The spatial pixel size in normal operation is 1" and the limiting sensitivity is $B=24$ for a star viewed with the detector in unfiltered light.

2.2 RXTE

The Rossi X-ray Timing Explorer (RXTE) was launched on 1995 December 30th, from NASA's Kennedy Space Center. The launch vehicle was a Delta II rocket that put RXTE into a low-earth circular orbit at an altitude of 580 km, corresponding to an orbital period of about 90 minutes, with an inclination of 23 degrees. RXTE provides unprecedented time resolution in combination with moderate spectral resolution to explore the variability of X-ray sources. Time scales from microseconds to months are covered in an instantaneous spectral range from 2–250 keV. Originally designed for a required lifetime of two years with a goal of five, RXTE has passed that goal and is still performing well.

The mission carries two pointed instruments, the Proportional Counter Array (PCA)

that covers the lower part of the energy range (2–60 keV), and the High Energy X-ray Timing Experiment (HEXTE) covering the upper energy range (10–250 keV). These instruments are equipped with collimators yielding a FWHM of one degree. In addition, *RXTE* carries an All-Sky Monitor (ASM) that scans about 80% of the sky every orbit, allowing monitoring at time scales of 90 minutes or longer.

Table 2.2: Basic characteristics of the *RXTE* instruments.

Instrument	PCA	HEXTE
Energy range:	2–60 keV	10–250 keV
Energy resolution:	18% at 6 keV	15% at 60 keV
Time resolution:	1 microsecond	8 microseconds
Collecting area:	6500 cm ²	2 × 800 cm ²
Sensitivity:	0.1 mCrab	1 Crab yields 360 counts/s per cluster
Background:	2 mCrab	50 counts/s per cluster
Spatial resolution:	collimator with 1 degree FWHM	

2.2.1 *PCA*

The Proportional Counter Array (PCA) is an array of five identical co-aligned gas-filled proportional counter modules with a total collecting area of 6500 cm². Each module, referred to as a Proportional Counter Unit (PCU), is equipped with a collimator. This means that each PCU has approximately the same field of view. Each PCU is split into two volumes, the upper propane veto volume and the main xenon volume. Through these volumes run five layers of anode-wire grids: 1 propane veto, 3 xenon and 1 xenon veto layer. Below the xenon volume is mounted an Americium-241 calibration source. The instrumental properties of the PCA are listed in Tab. 2.2.

The top one of the 3 xenon layers is the most sensitive. Selecting events from only the first layer will yield higher signal-to-noise than the second layer, the third layer or any combination of layers. This is because significantly more X-ray interactions occur in the top layer than in the bottom two, whereas the instrumental background depends less on layer.

Information on events occurring in the PCA detectors is handled by the Experiment Data System (EDS), a microprocessor-driven on-board data system. The EDS

⁷Graphic by Center for Astrophysics & Space Sciences, University of California, San Diego (http://mamacass.ucsd.edu:8080/hexite/pictures/xte_spacecraft.gif)

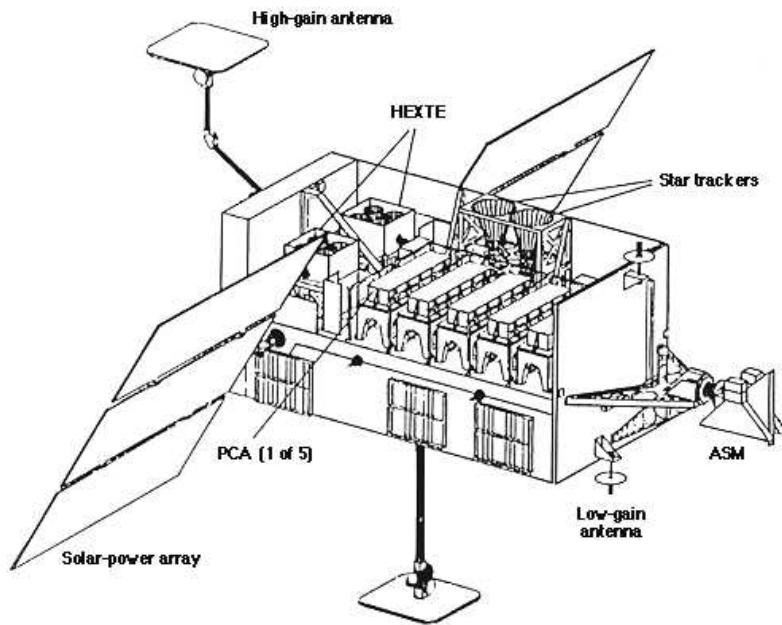


Figure 2.6: Schematic representation of RXTE.⁷

is capable of processing up to 500 000 counts per second, and can time the arrival of individual X-rays to about 1 microsecond. The data can be collected in a number of different data modes simultaneously. This facilitates collection and analysis of the data appropriate to different sources.

The EDS consists of eight Event Analyzers (EA), of which six are dedicated to the PCA and two to the ASM. The EAs can be programmed independently to process incoming events from the instruments in any of the following modes:

- **Event Encoded mode**: yields data as a time-series of unevenly spaced events each described by arrival time, pulse height, PCU ID, etc. Configurations comprise generic events, good xenon and transparent.
- **Binned Data mode**: events are summarised as regularly accumulated histograms of pulse height, time and event type. Configurations comprise generic binned, standard-1 and standard-2.

- Single Bit mode: generates a stream of zeros and ones representing events and clock ticks.
- Burst Catcher mode: uses two EAs, one to search data and generate a trigger (activated by count rate, rate of change of count rate or hardness), and the other one to collect data in binned or event modes. Configurations comprise event burst catcher and binned burst catcher.
- Delta-binned mode: yields data in a time-series of regularly spaced histograms of the times between events.
- Fast Fourier Transform mode: accumulates simultaneously the channels of 256 time bins and averages the power density spectrum and cross spectrum.
- Pulsar Fold mode: yields data in time-series of regularly spaced histograms, counted in pulse periods, of pulse height, pulsar phase and event type. The configuration must be specially created for each observation.

Two of the EAs always run in the standard-1 and standard-2 configurations. The configurations of the other four EAs are specified by the proposal for observations.

2.2.2 *HEXTE*

The High Energy X-ray Timing Experiment (HEXTE) consists of two independent clusters of detectors. The clusters are known as Cluster-A and Cluster-B. Each cluster contains four NaI(Tl)/CsI(Na) Phoswich detectors. Each detector is split into two volumes, the primary NaI detector crystal and the CsI shield/light guide crystal. X-rays produce scintillations in the NaI crystal, while particles can produce scintillations in both the NaI and CsI crystals. Since the scintillations in the two crystals, as recorded by the photomultiplier tube, have different rise times, the two kinds of event can be distinguished. Automatic gain control is provided by using an Americium-241 radioactive source mounted in each detector's field of view.

There are five HEXTE data modes:

- Archive mode: is roughly equivalent to PCA standard-1/2 and yields 64-channel spectra per detector as well as 1.0-second light curves in four energy bands. This mode, running always, provides a uniform and continuous archive of data collected over the lifetime of the mission.
- Event List mode: yields time-tagged information about every event that survives background rejection and passes through the various discrimination windows.

- Histogram Bin mode: provides PHA histograms every 1–16 seconds, separated by detector.
- Multiscale Bin mode: yields time histograms with a resolution of 0.5 milliseconds to 1 second, separated by detector or not, in 2, 4, 6 or 8 PHA bands.
- Burst List mode: a triggered version of the Event List mode providing event-by-event information.

Each cluster can beam switch along RXTE spacecraft's Z and Y axes to provide background measurements 1.5 or 3.0 degrees away from the source every 16 to 128 seconds, as defined by the observer. When one cluster is on target, the other one is off target and vice versa. The rocking axis of the two clusters are orthogonal resulting in a total of four different background regions, two per cluster, for each source pointing.

CHAPTER 3

The Data Processing

3.1 XMM EPIC Data

Between 2000 June and 2003 January the quasar 3C 273 was observed 16 times by the X-ray satellite XMM *Newton*. Four observations were performed as off axis observations. These offset observations were not used for our spectral analysis because the instrument response for non focal point spread functions (PSF) was not calibrated well enough. Also these observations show strong pile-up effects due to the long frame integration times of the selected full frame mode. A summary of all observations is given in Table 3.1.

Table 3.1: Summary of XMM observations of 3C 273. FF = full frame mode; SW = small window mode; TI = timing mode; BU = burst mode.

Date	Obs. ID	Exposure [s]	Mode	Filter	
2000-06-13	0126700101	PN:	4 848	FF	medium, offset -7'
		MOS1:	7 544	FF	medium, offset -7'
		MOS2:	7 544	FF	medium, offset -7'
2000-06-13	0126700201	PN:	22 598	FF	medium, offset -1.5'
		MOS1:	25 334	FF	medium, offset -1.5'
		MOS2:	25 334	FF	medium, offset -1.5'
2000-06-14	0126700301	PN:	65 823	SW	medium
		MOS1:	63 374	SW	medium
		MOS2:	63 374	SW	medium
2000-06-15	0126700401	PN:	4 698	FF	medium, offset +7'
		MOS1:	7 394	FF	medium, offset +7'
		MOS2:	7 394	FF	medium, offset +7'

continued on next page

Date	Obs. ID	Exposure [s]	Mode	Filter
2000-06-15	0126700601	PN: 29 703	SW	medium
		MOS1: 27 194	SW	medium
		MOS2: 27 194	SW	medium
2000-06-16	0126700701	PN: 30 003	SW	medium
		MOS1: 29 994	SW	medium
		MOS2: 29 994	SW	medium
2000-06-16	0126700501	PN: 7 453	FF	medium, offset +1.5'
		MOS1: 9 642	FF	medium, offset +1.5'
		MOS2: 9 642	FF	medium, offset +1.5'
2000-06-18	0126700801	PN: 60 632	SW	medium
		MOS1: 58 227	SW	medium
		MOS2: 58 248	SW	medium
2001-06-13	0136550101	PN: 88 623	SW	medium
		MOS1: 43 454	SW	thin
		MOS1: 45 254	SW	medium
		MOS2: 43 454	SW	thin
		MOS2: 45 254	SW	medium
2001-12-16	0112770101	PN: 5 003	SW	thin
		MOS1: 5 540	TI	medium
		MOS2: 5 795	SW	medium
2001-12-22	0112770201	PN: 4 993	SW	thin
		MOS1: 5 540	TI	medium
		MOS2: 5 795	SW	medium
2002-01-09	0137551001	PN: 18 777	TI,BU	medium
		MOS1: 20 412	LW,SW,TI	medium
		MOS2: 20 412	LW,SW,TI	medium
2002-07-07	0112770601	PN: 4 993	SW	thin
		MOS1: 2 621	TI	medium
		MOS2: 2 864	SW	medium
2002-12-17	0112770801	PN: 4 993	SW	thin
		MOS1: 4 890	TI	medium
		MOS2: 5 145	SW	medium
2003-01-05	0136550501	PN: 8 505	SW	medium
		MOS1: 8 657	SW	medium
		MOS2: 8 657	SW	medium

continued on next page

Date	Obs. ID	Exposure [s]	Mode	Filter	
2003-01-05	0112770701	PN:	4 993	SW	thin
		MOS1:	4 890	TI	medium
		MOS2:	5 145	SW	medium
2003-07-08	0112770501	PN:	8 105	SW	thin
		MOS1:	8 002	TI	medium
		MOS2:	8 262	SW	medium

Before the spectral analysis all observations were checked whether they are affected by pile-up. For data reduction reason the on-board data handling system of EPIC does not link down the complete frames (one read out of the complete chip), but analyses the frames for detected photons (events). Only the information of these events are sent to ground. In general, pile-up effects are errors of these photon reconstructions.

The point spread function (PSF) can be influenced by pile-up, if in the core of the PSF too many photons arrive at almost the same time within one readout frame. The spectral response can be compromised by energy pile-up, if two or more photons deposit charge in the same pixel before the readout, thus creating one artificially hard photon. If within one readout frame two or more photons deposit charge in neighbouring pixels, the photon reconstruction merges these neighbouring pixels together creating wrong multi-pixel photon patterns. This effect is called pattern pile-up.

The probability of producing artificial double events is 4 times larger than that of producing artificial hard single events. Therefore at moderate pile-up rates the main effect of pile-up is expected to be pattern pile-up. There are two different methods to verify a possible pile-up: count rate analysis and analysis of pattern distribution.

The XMM-Newton Users' Handbook (XMM-PS-GM-14 2003) provides estimates of count rates for the different EPIC instrument modes for which pile-up should not be a problem. For PN small window mode this maximum count rate is 130 cts/s and 5 cts/s for MOS small window mode. The maximum count rate of all PN observations is about 63 cts/s, thus the PN observations show no pile-up effects. For the MOS observations count rates between 13-19 cts/s are found, indicating that all observations are affected by pile-up.

The same result is provided by the pattern analysis. The XMM SAS¹ task EPAT-PLOT plots the observed pattern distribution over the theoretically expected one, known

¹XMM Science Analyzing Software, Version 5.4.1

from the calibration. Examples of these plots are shown in Fig. 3.2. The pattern fractions of types single, double, triple and quadruple dependent on photon energy are shown. For PN (top) there is a small discrepancy between theoretical and measured pattern distribution in the energy range of 0.4–0.6 keV, which is due to a slightly incorrect estimation of the thickness of the SiO₂ entrance window on the PN CCD chip.

In the energy range of 2–4 keV the MOS2 plot (Fig. 3.2, bottom) shows a small excess of double events and a lack of single events. This is a clear signature of pattern pile-up, where two single events in neighboring pixels within one integration cycle are reconstructed wrongly as a double event. Another indication for a stronger pile-up are the so-called diagonal patterns, two mono pixel events not side by side next to each other, but the second event at the corner of the first one. These patterns are not expected from a genuine X-ray, but they can arise in case of Si fluorescence or of pile-up. The low rate of diagonal patterns in the observations of the quasar 3C 273 and the small excess of the single/double event distribution prove that the MOS observations are affected by soft pile-up problems only.

The discrepancy observed above 2 keV between predicted and measured single event fractions does not imply that major spectral distortions of the single event spectrum are occurring at energies greater ~ 2 keV. At moderate pile-up rates the main effect of pile-up is to take single events and turn them into doubles. Molendi & Sembay (2003) verified that since the probability of an event to be lost to pile-up is independent of its energy, the loss of events will result in a lower normalization of the single event spectrum and not in a distortion of its shape.

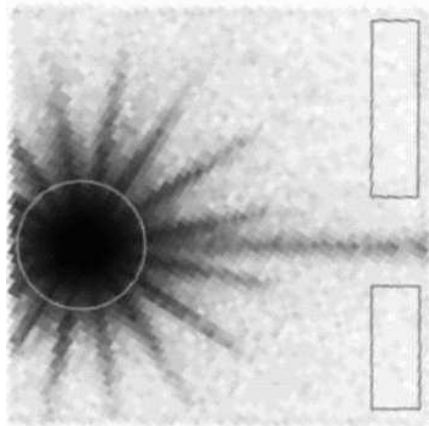


Figure 3.1: Example of the PN source and background region selection.

3.1.1 Data selection

A detailed description of EPIC data reduction is omitted. There are several documents describing the XMM science analyzing software and the technical methods for data reduction, available at the ESA² or NASA³ XMM web pages. I confine myself to selected details which are necessary to reproduce the analysis.

²<http://xmm.vilspa.esa.es/>

³<http://heasarc.gsfc.nasa.gov/docs/xmm/xmmgof.html>

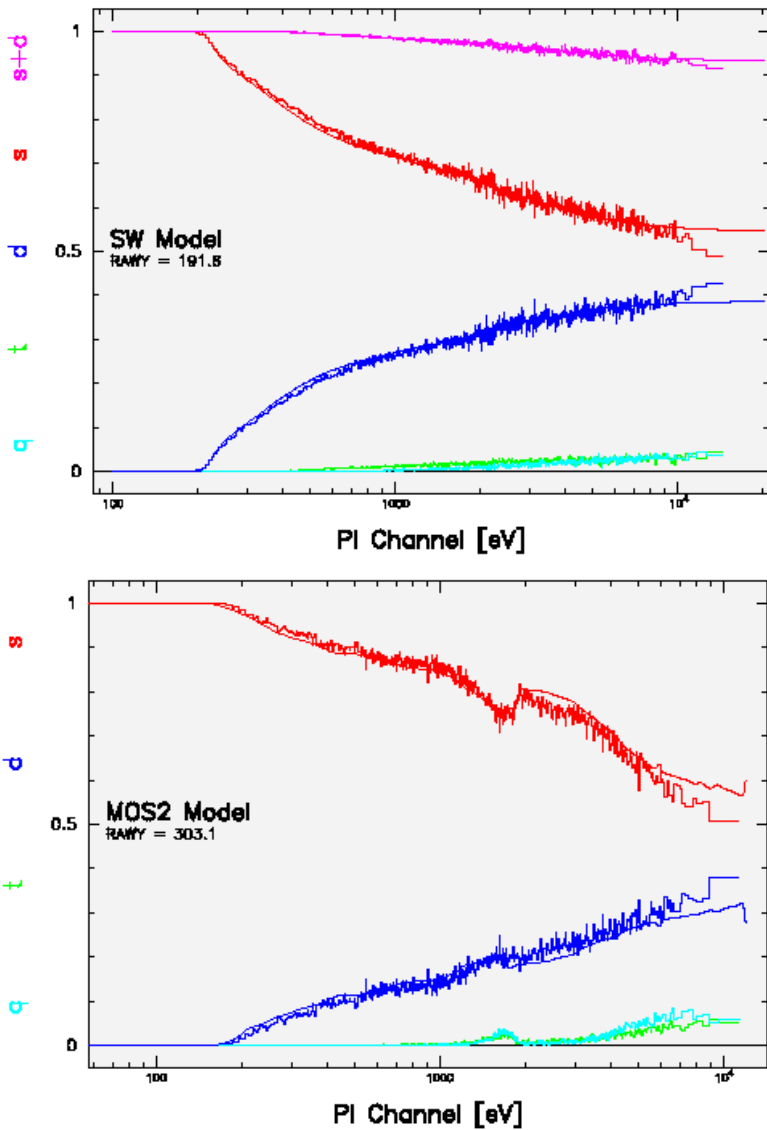


Figure 3.2: Example of a pattern distribution provided by SAS task EPATPLOT from observation 2001-06-13, top: PN; bottom: MOS2.

For spectral analysis of all EPIC instruments only single events (PATTERN=0) are used with all bits of the event quality flags set to zero (FLAG=0). For both the MOS and the PN cameras, source photons are extracted out of a circular region with a radius of 40 arcsec (sky projection) around the center of the PSF. PN background is taken out of two boxes close to the border of the small window pixel field. Fig. 3.1 illustrates the source and background regions defined at the PN small window picture. The stripes around the source are the diffraction image of the mounting of the mirror shells pictured in Fig. 2.2. It is not possible to define a background field inside the central MOS CCD1 because the PSF dominates the complete small window area. Therefore the MOS backgrounds are taken from two surrounding CCDs (MOS1: No.2+4; MOS2: No.3+6) out of areas where no source is visible.

The good time intervals (GTI) of the observations are selected via light curves of the background areas. An example of the GTI selection is shown in Fig. 3.3. The figure contains the PN background light curve of observation 0126700801. Times showing background flares are excluded from the spectral analysis.

Before the analysis the raw spectra are rebinned to increase the amount of counts per channel especially at higher energies. The raw spectra of the PN have 4096 channels, each channel representing an energy interval of 5 eV. For the analysis of the continuum emission the PN spectra are rearranged into bins with bin sizes of about half the energy resolution of the instrument. For the analysis of the upper limits of a possible Fe-line the sizes of the bins are bisected (values in brackets) to get a better coverage for a narrow line feature.

- Channel 0–255 (0–1.275 keV): Binning of 4 (2) channels.
- Channel 256–511 (1.275–2.555 keV): Binning of 8 (4) channels.
- Channel 512–1023 (2.555–5.110 keV): Binning of 16 (8) channels.
- Channel 1024–4095 (5.110–20.440 keV): Binning of 32 (16) channels.

The raw spectra of the MOS have 800 channels, each channel representing an energy interval of 15 eV. The MOS spectra are rebinned in the same way than the PN spectra in respect of the channel numbers. Equivalent to PN the bins are bisected for line analysis purposes (values in brackets).

- Channel 0–255 (0–3.840 keV): Binning of 4 (2) channels.
- Channel 256–511 (3.840–7.680 keV): Binning of 8 (4) channels.

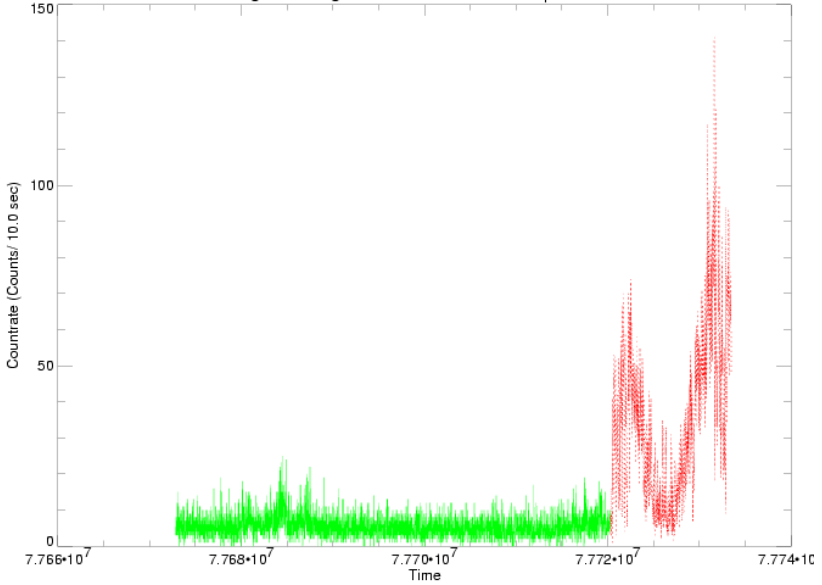


Figure 3.3: Example for GTI selection: times showing background flares are excluded from the spectral analysis.

- Channel 512–799 (7.680–12.000 keV): Binning of 16 (8) channels.

Comparing the spectra of the three EPIC instruments I found the PN and MOS2 in good agreement, but the MOS1 SW spectra to be systematically harder than the others. For example, the results for a power law model of the spectra > 2.5 keV of observations 0126700801 are 1.63 ± 0.01 for PN, 1.62 ± 0.02 for MOS2 and 1.54 ± 0.02 for MOS1. The results for observation 0136550101 that was performed about one year later is similar: 1.61 ± 0.01 for PN, 1.61 ± 0.02 for MOS2 and 1.54 ± 0.02 for MOS1. Including the cross-calibration of EPIC with RXTE PCA, the spectral slopes measured by PCA, PN and MOS2 are consistent with each other. Therefore I considered the MOS1 not to be in accordance with the other instruments. This deviation of the MOS1 spectral slope is also confirmed by the calibration team of the EPIC consortium (Kirsch 2003). Because of this cross-calibration problems we excluded MOS1 from our analysis.

3.2 RXTE Data

For XMM observations of 2000-06-14 and 2003-01-05 there are simultaneous observations of RXTE. Some other RXTE observations were performed close to the XMM ones with offsets of less than one day. A summary of the observations is given in Table 3.2.

Table 3.2: Summary of RXTE observations of 3C 273. For positive offsets the RXTE observation was later than the corresponding XMM one.

Date	Obs. ID	Exposure [s]	Offset [h]
2000-06-14	P50184-01-01-00	3 264	simultaneous
	P50184-01-01-01	6 928	simultaneous
	P50184-01-01-02	2 432	simultaneous
	P50184-01-01-03	1 280	simultaneous
2001-06-13	P60144-03-45-00	1 600	-3
2001-12-16	P60144-03-01-10	1 680	+4
2001-12-21	P60144-03-03-10	1 152	-24
2001-12-23	P60144-03-04-10	1 024	+27
2001-12-23	P60144-03-04-11	752	+31
2002-01-09	P60144-03-11-10	1 584	-6
2003-01-05	P50184-02-01-00	23 072	simultaneous
2003-06-16	P80165-01-01-00	9 530	-551
2003-07-21	P80165-01-02-00	7 168	+299
	P80165-01-02-01	2 994	+303
2004-01-01	P80165-01-03-00	5 104	
2004-01-02	P80165-01-03-01	512	

Again I do not mention all steps of the RXTE data reduction. A detailed description is available at the web pages of the NASA RXTE Guest Observer Facility⁴. From the five PCUs of the PCA instrument only PCU0 and PCU2 were available at all of the observations. The PCUs have three xenon layers. In the low energy band (i.e. < 10 keV) the top layer detects roughly 90 percent of the cosmic photons and contributes 50 percent to the internal instrumental background. Thus the signal-to-noise ratio for weak sources can be improved by selecting only events from the top layer. The definition of a weak source is fuzzy of course, since it depends on the source spectrum. As a rule of thumb, the RXTE Cook Book makes a cut at a rate of 20 counts per second per PCU. For all observations with lower count rates, we therefore used only signals from the top layers in order to obtain the best signal-to-noise ratio.

⁴http://heasarc.gsfc.nasa.gov/docs/xte/xhp_proc_analysis.html

Because in 2000 May the PCU0 lost the propane gas, all presented results were obtained using the top layer of PCU2 only.

The PCA Standard Mode 2 data were reduced using FTOOLS V5.2. The response file was generated using PCARMF V8.0. The background estimation was done with PCABACKEST V3.0 using the L7-240 background model recommended for faint sources. To assure that there is no significant electron contamination, times with electron ratio >0.1 were filtered out. All PCA spectra are analysed in the energy range from 2.5-21 keV. This energy range corresponds to channels 4–46 out of the 129 channels of the standard 2f spectra.

Both HEXTE clusters are combined to get higher signal to noise ratio. In addition the 256 channels of the combined HEXTE spectra are binned the following way:

- Channel 0–35 (0–35 keV): Binning of 2 channels.
- Channel 36–53 (35–53 keV): Binning of 6 channels.
- Channel 54–245 (53–261 keV): Binning of 16 channels.
- The remaining channels are single channels, but they are not used anyway.

Nevertheless the count rate is very weak, the 1σ error bars are large. Fitting the PCA and HEXTE (20–190 keV) data simultaneously, the fit is completely dominated by the PCA, the resulting $\Gamma(\text{PCA/HEXTE})$ is identical to $\Gamma(\text{PCA})$.

CHAPTER 4

Results of Spectral Analysis

The average broad band spectrum of 3C 273 derived from its historical data base (Türler et al. 1999b) allows to pre-estimate the spectral components of the XMM and RXTE spectra. In Fig. 1.4 the used energy range of EPIC and RXTE is highlighted. A single power law component dominates the spectral shape from about 1 MeV down to about 1 keV. At lower energies there is more flux than predicted by the high energetic power law component. This additional emission is called the soft excess.

All power law indices mentioned in this work are photon indices that refer to analysis of photon count spectra. The power law representation

$$F_E \sim E^{-\alpha} \quad [\text{keV}/\text{cm}^2 \cdot \text{s} \cdot \text{keV}] \quad (4.1)$$

with energy index α is changed into the form

$$F_E \sim E^{-\Gamma} \quad [\text{ph}/\text{cm}^2 \cdot \text{s} \cdot \text{keV}] \quad (4.2)$$

with photon index $\Gamma = \alpha + 1$.

The errors of all model parameters are determined using the `ERROR` command of the XSPEC package, using a delta χ^2 statistic of 2.706, equivalent to the 90% confidence region for a single interesting parameter (one degree of freedom).

The errors of all fluxes as well as line equivalent widths are determined using two-dimensional fit-statistic contour plots of the relevant model parameters. The initial default values for the contour levels are used. In χ^2 statistic these levels are 2.23, 4.61 and 9.21, equivalent to 68%, 90% and 99% confidence regions (two free parameters). The extrema of the model fluxes/equivalent widths are determined using the parameter values of the 99% confidence line. As an example of a contour plot the confidence levels of the possible Fe-line detection of the MOS2 observation from 2000-06-16 is shown in Fig. 4.1. The two free parameters are the line energy (quasar frame) and line flux, the line width is fixed to $\sigma = 0.12$ keV. See Sect. 4.1.5 for the details.

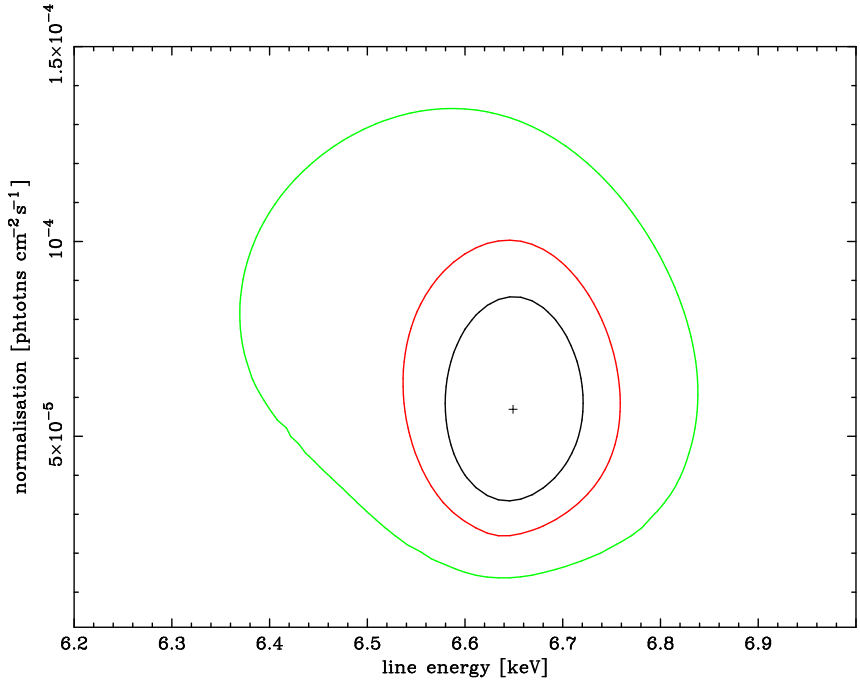


Figure 4.1: Contour plot I–E of a possible Fe–line detection in MOS2 observation from 2000-06-16, showing 68, 90 and 99 per cent (innermost to outermost curves) confidence regions for the two free parameters line energy (quasar frame) and line flux. The cross tags the best fit values.

4.1 The Spectra Above 2.5 keV

First the power law describing the hard X–ray spectral component is analysed. Therefore a lower limit for the energy range of $E > 2.5$ keV is used. This selection corresponds to the lowest energy available for the RXTE PCA detector. For XMM this limitation excludes the instrumental edge at about 2.2 keV caused by the gold surface of the mirror system. The limit is also well above the energy range where the additional softer component is expected. Simultaneous observations with ROSAT and Ginga found this soft excess component to be in the range 0.1–1.0 keV (Staubert et al. 1992).

4.1.1 RXTE PCA

All PCA spectra are fitted in the energy range from 2.5–21.0 keV. As fit model a single power law with galactic absorption was used:

$$F_E = e^{-N_H \sigma(E)} \cdot I_{(1\text{keV})} \cdot E^{-\Gamma} \quad (4.3)$$

$I_{(1\text{keV})}$ is the normalisation at 1 keV in units of photons $\text{cm}^{-2}\text{s}^{-1}\text{keV}^{-1}$. The galactic absorption was fixed to $N_H = 1.79 \cdot 10^{20} \text{ cm}^{-2}$ (Dickey & Lockman 1990). None of the observations showed indications of an Fe-line. The spectral results are summarised in Tab. 4.1. The 3–10 keV fluxes are given in units of $10^{-11} \text{ erg cm}^{-2}\text{s}^{-1}$, with $1 \text{ eV} = 1.6 \cdot 10^{-12} \text{ erg}$.

Table 4.1: Fit results of PCA spectral analysis for a single power law model including a fixed galactic absorption. Fluxes (3–10 keV) are given in units of $10^{-11} \frac{\text{erg}}{\text{cm}^2\text{s}}$. The spectral results of the combined PCA/HEXTE fits are identical to the PCA results. Therefore only the normalisation constants (see sect. 4.1.2) of HEXTE¹ are provided.

Date	RXTE PCA		HEXTE	
	Γ	Flux _{3–10keV}	$\chi^2/41 \text{ dof}$	norm.const.
2000-06-14	1.61±0.02	8.50±0.10	0.84	0.77±0.05
2001-06-13	1.60±0.05	9.76±0.29	0.79	0.93±0.11
2001-12-16	1.61±0.04	12.40±0.27	1.05	0.79±0.09
2001-12-21+23	1.58±0.03	13.13±0.24	1.05	0.73±0.06
2002-01-09	1.59±0.05	9.06±0.30	0.84	0.77±0.14
2003-01-05	1.73±0.02	9.17±0.09	0.70	0.78±0.04
2003-06-16	1.68±0.01	12.47±0.11	0.93	0.79±0.03
2003-07-21	1.63±0.02	9.18±0.11	0.69	0.74±0.04
2004-01-01+02	1.69±0.02	10.13±0.14	0.73	0.96±0.05

As an example the RXTE spectra of observation 2000-06-14 are presented in Fig. 4.2. The power law index of this observation was fitted to $\Gamma = 1.61 \pm 0.02$, the resulting HEXTE normalisation constant (see 4.1.2) was $\text{const} = 0.77 \pm 0.05$. In appendix A the spectra of all RXTE observations are presented in two plots, one showing the PCA spectrum stand alone and a second one illustrating the combined PCA + HEXTE spectrum.

¹For the most recent (2004 Apr.) RXTE responses these cross calibration problems have been solved.

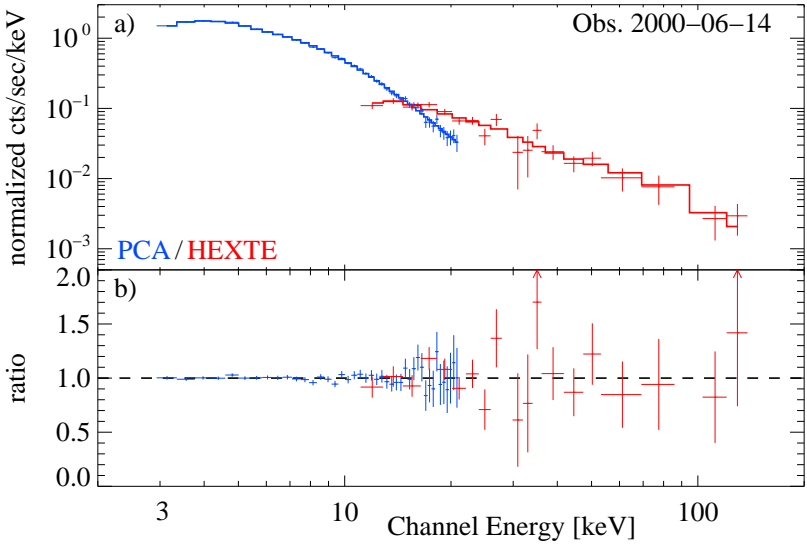


Figure 4.2: Combined PCA + HEXTE spectrum of observation P50184-01-01-00/01/02/03 fitted by a single power law model including galactic absorption. Power law index $\Gamma = 1.61 \pm 0.02$, HEXTE normalisation constant $\text{const} = 0.77 \pm 0.05$. All RXTE spectra are presented in appendix A.

4.1.2 RXTE HEXTE

Both clusters of HEXTE were combined to get a higher signal to noise ratio. Nevertheless due to the rather short observations the accumulated source counts are very low. Dependent on the observation time, the highest HEXTE channels where the quasar 3C 273 was clearly detected are in the range of 50–140 keV. If the HEXTE data are fitted independently from the PCA data, the power law indices tend to be slightly softer, but within the error bars the results are still consistent with the PCA. Fitting the PCA and HEXTE data simultaneously, the fit is dominated by the PCA, the resulting $\Gamma(\text{PCA}/\text{HEXTE})$ is identical to $\Gamma(\text{PCA})$. For these simultaneous fits a normalisation constant is added to the fit model with the PCA constant is fixed to equal one:

$$F_{\text{PCA}}(E) = \text{const} \cdot F_{\text{HEXTE}}(E) \quad (4.4)$$

The results of the HEXTE normalisation constants are shown in Tab. 4.1. Fig. 4.2 gives an example of the HEXTE spectra. The energy ranges of HEXTE where the signal of the 3C 273 is detected above the noise level of the detector are summarised in Tab. A.1 in appendix A as well as all HEXTE spectra.

4.1.3 XMM EPIC

The EPIC instruments PN and MOS2 are fitted independently. The first topic of the analysis is to confirm the high energetic power law component which is measured by RXTE. Therefore the low energy range of EPIC (0.3–2.5 keV) is ignored and the remaining energy range of 2.5–10.0 keV, referred to as high energy range, is used for all EPIC instruments. Tab. 4.2 summarises the fit results of a single power law model including a fixed galactic absorption of $N_{\text{H}} = 1.79 \cdot 10^{20} \text{cm}^{-2}$ (Dickey & Lockman 1990).

Table 4.2: Fit results for EPIC spectra $E = 2.5\text{--}10.0 \text{ keV}$ of a single power law model including a fixed galactic absorption. PN and MOS2 are fitted independently. Fluxes (3–10 keV) are given in units of $10^{-11} \frac{\text{erg}}{\text{cm}^2 \text{s}}$. The degrees of freedom (dof) are 63 for both PN and MOS2.

Date	EPIC PN			EPIC MOS2		
	Γ	$\text{Flux}_{3-10\text{keV}}$	χ^2/dof	Γ	$\text{Flux}_{3-10\text{keV}}$	χ^2/dof
2000-06-14	1.66 ± 0.01	6.44 ± 0.06	1.51	1.64 ± 0.02	6.22 ± 0.10	1.28
2000-06-15	1.60 ± 0.02	6.44 ± 0.08	1.23	1.61 ± 0.03	6.21 ± 0.14	1.26
2000-06-16	1.62 ± 0.02	6.21 ± 0.08	1.44	1.61 ± 0.03	6.03 ± 0.14	1.71
2000-06-18	1.63 ± 0.01	6.27 ± 0.06	1.68	1.62 ± 0.02	6.05 ± 0.11	0.98
2001-06-13	1.61 ± 0.01	7.66 ± 0.06	1.30	1.61 ± 0.02	7.29 ± 0.12	1.44
2001-12-16	1.67 ± 0.04	8.99 ± 0.25	1.34	1.57 ± 0.05	8.83 ± 0.38	0.97
2001-12-22	1.64 ± 0.03	9.52 ± 0.26	1.06	1.59 ± 0.05	8.80 ± 0.39	0.97
2002-01-09	1.71 ± 0.02	4.12 ± 0.08	0.81	1.71 ± 0.06	6.38 ± 0.36	1.05
2002-07-07	1.77 ± 0.04	6.24 ± 0.21	0.93	1.78 ± 0.08	5.84 ± 0.43	0.93
2002-12-17	1.79 ± 0.04	8.12 ± 0.24	1.29	1.72 ± 0.05	7.70 ± 0.36	1.27
2003-01-05	1.74 ± 0.03	6.84 ± 0.17	0.99	1.74 ± 0.05	6.37 ± 0.25	0.92
2003-01-05	1.73 ± 0.04	6.71 ± 0.22	1.18	1.75 ± 0.06	6.44 ± 0.33	1.14
2003-07-08	1.78 ± 0.03	7.31 ± 0.18	0.87	1.76 ± 0.05	6.83 ± 0.28	1.32

From the four 2000 June observations with an offset of roughly a day to each other, the last three are fully consistent with each other. The first PN observation shows a steeper power law index than the three others. The 3–10 keV spectrum of this observation is presented in Fig. 4.3. The residuals of the power law model (Fig. 4.3b) indicate an edge-like structure at about 6 keV, close to the energy expected from redshifted iron. Thus, the spectra are re-analysed adding a redshifted edge to the fit model, with the threshold energy E_{edge} , the absorption depth at the threshold τ and the redshift $z = 0.158$ of the quasar.

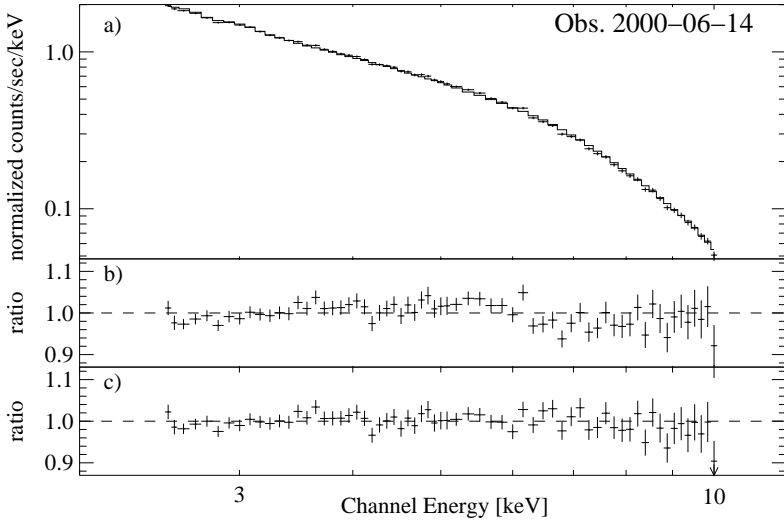


Figure 4.3: The PN spectrum (2.5-10 keV) of observation 0126700301. a+b) Single power law model including galactic absorption: $\Gamma = 1.66 \pm 0.01$. c) Power law plus redshifted Fe-edge including galactic absorption: $\Gamma = 1.62 \pm 0.02$, $E_{\text{Edge}} = 7.30 \pm 0.10$, $\tau_{\text{max}} = 0.084 \pm 0.022$.

$$F_E = \begin{cases} e^{-N_H \sigma(E)} \cdot I_{(1\text{keV})} \cdot E^{-\Gamma} & E < E_{\text{edge}} \\ e^{-N_H \sigma(E)} \cdot I_{(1\text{keV})} \cdot E^{-\Gamma} \cdot e^{-\tau \left(\frac{E(1+z)}{E_{\text{edge}}} \right)^3} & E > E_{\text{edge}} \end{cases} \quad (4.5)$$

For observation 2000-06-14 the PN fit provides the results $E_{\text{edge}} = 7.30 \pm 0.10$, $\tau = 0.084 \pm 0.022$. The power law index hardens to $\Gamma = 1.62 \pm 0.02$, consistent with the results of the other observations. The fit improves by $\Delta\chi^2 = 40.4$ for 2 degrees of freedom, with an F -test probability of $4.8 \cdot 10^{-8}$. The residuals for the fit model including the redshifted edge are presented in Fig. 4.3 c).

However, no edge-like structure is visible in the corresponding MOS2 spectrum (app. B, Fig. B.1). Offering the additional edge component to the MOS2, the fit improves only slightly by $\Delta\chi^2 = 5.8$ for two free parameters with an F -test probability of 0.10 ($E_{\text{edge}} = 7.15_{-0.16}^{+0.56}$, $\tau = 0.052 \pm 0.037$, $\Gamma = 1.62 \pm 0.02$). Anyway, the resulting parameter values are consistent with the PN results.

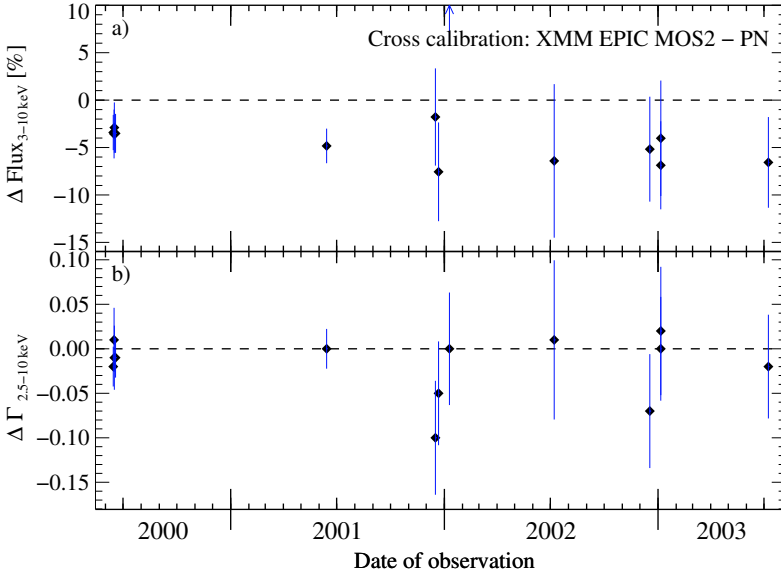


Figure 4.4: Cross calibration of EPIC PN and MOS2. a) $\text{Flux}_{\text{MOS2}}$ minus Flux_{PN} (3–10 keV): The MOS2 fluxes are lower than the PN ones by about 5% because of the loss of photons due to pile-up. b) Γ_{MOS2} minus Γ_{PN} : The two detectors are in very good agreement.

Different results are obtained if the additional edge component is fitted to other observations. Some PN fits produce results consistent with the edge values of observation 2000-06-14, the F -test probabilities are larger (2000-06-15: $1.5 \cdot 10^{-2}$; 2000-06-16: $2.7 \cdot 10^{-4}$; 2000-06-18: $9.3 \cdot 10^{-4}$; 2001-06-13: $1.3 \cdot 10^{-6}$). As seen before, the corresponding MOS2 spectra do not confirm any presence of an edge-like structure. All other observations do not support this additional edge component.

The comparison of the results of PN and MOS2 (Fig. 4.4) demonstrates that the two instruments are nicely consistent with regard to the measured spectral shape in the energy range of 2.5–10.0 keV. The differences of the power law indices in Fig. 4.4 are $\Gamma_{\text{MOS2}} - \Gamma_{\text{PN}}$. The maximum divergence of the PN and MOS2 power law indices is 0.1 at observation 2001-12-16.

The PN fluxes are higher than the MOS2 fluxes for all observations except for the observation of 2002-01-09. In this observation the PN was in timing mode, the MOS2

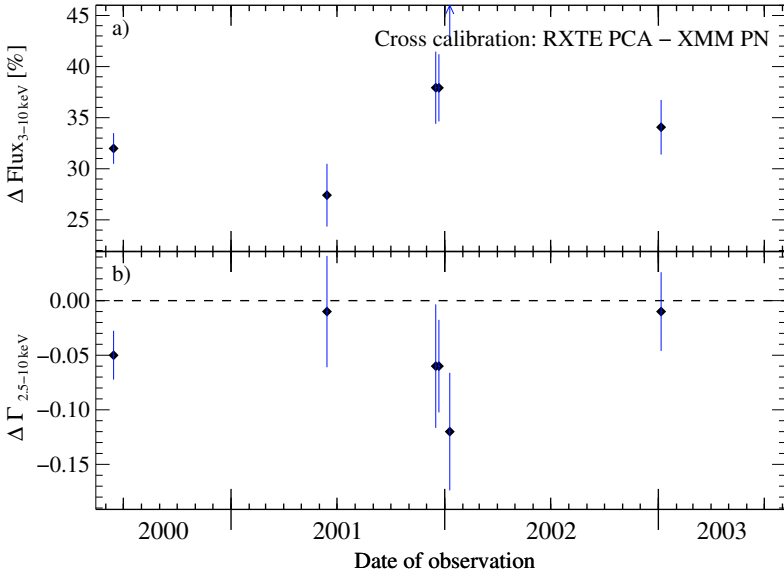


Figure 4.5: Cross calibration of RXTE PCA and XMM EPIC PN. a) Flux_{PCA} minus Flux_{PN} (3–10 keV): The PCA fluxes in the energy range of 3–10 keV are about 34% higher than the PN fluxes. This is a well known feature of the PCA. b) Γ_{PCA} minus Γ_{PN} : The spectral shape measured by the PCA is slightly harder than the one found by the PN.

in small window mode. The configuration of both PN and MOS2 at all other observations is the small window mode. In Fig. 4.4 the flux differences and the differences of the power law indices are plotted. In case of both instruments using the small window mode, the PN fluxes are on average 5.4% higher than the MOS2 ones. This effect is caused by the loss of photons due to pile-up in the center of the PSF of the MOS. Thus in the plot the flux of the PN is defined to be the reference.

4.1.4 Simultaneous Observations of RXTE and XMM

Simultaneous observations by two satellites with different observation techniques using detectors with different characteristics are important for space-based science. In the ideal case all instruments observing the same object at the same time should provide consistent results. The EPIC cross calibration of PN and MOS2 is a successful example. Since after their lifetime in space the “old” satellites are replaced by others

having a new payload technology, simultaneous observations are needed to ensure the correct changeover for the interpretation of measurements because the instrumental responses can be compared directly. Any uncertainties caused by the possible variation of the observed source are excluded by simultaneous observations.

The observations used for this work enable the cross calibration of RXTE and XMM. The differences between RXTE PCA and XMM EPIC PN of all quasi simultaneous ($\Delta t < 31$ h) observations are shown in Fig. 4.5. Note that only the observations performed on 2000-06-14 and 2003-01-05 are performed absolutely simultaneously (see Tab. 3.2). The 3–10 keV flux reference levels are the PN fluxes again. The PCA fluxes are at average 34% higher than the PN fluxes. This flux excess is a well known feature of the PCA². At a cross-calibration of RXTE with ASCA in 1996 and 1998 Tahir Yaqoob³ found the PCA fluxes to be 23–28% higher than those of ASCA. The calibration object was the quasar 3C 273. The XMM-EPIC status of calibration (Kirsch 2003) reports that the agreement of EPIC and ASCA in the measured fluxes is about $\pm 10\%$ (these are results from observations of two supernova remnants). So, the cross calibration between RXTE, ASCA and XMM (PN and MOS2) is reasonably understood.

4.1.5 Fe-Line

The analyses of the spectra at energies > 2.5 keV are also used for the search for signatures of an iron $K\alpha$ emission line. There are only a few publications about detections of neutral iron line emission in the X-ray spectra of 3C 273. For most observations of the quasar the single power law model is sufficient to describe the spectral shape between 3–20 keV.

The possible presence of a neutral iron emission line was investigated systematically for all XMM observations. Therefore an additional redshifted Gaussian line component was added to the power law model:

$$F_E = e^{-N_H\sigma(E)} \cdot \left[I_{(1\text{keV})} \cdot E^{-\Gamma} + K \cdot \frac{1}{\sqrt{2\pi\sigma^2}} \cdot e^{-0.5\left(\frac{E \cdot (1+z) - E_{\text{Fe}}}{\sigma}\right)^2} \right] \quad (4.6)$$

K represents the total flux in the line in units of [photons $\text{cm}^{-2} \text{s}^{-1}$]. The redshift was fixed to the known value of $z = 0.158$ and the line energy to $E_{\text{Fe}} = 6.4$ keV of neutral Fe $K\alpha$. The Gaussian line widths were fixed to $\sigma = 0.01$ keV for the narrow line and $\sigma = 0.8$ keV for the broad line, respectively, according to the sole publication of the

²For the most recent (2004 Apr.) RXTE responses these cross calibration problems have been solved.

³http://heasarc.gsfc.nasa.gov/docs/asca/calibration/3c273_results.html

detection of a broad line feature by Yaqoob & Serlemitsos (2000).

Table 4.3: Upper limits (3σ) of a possible Fe K α line. The narrow lines have an intrinsic width of $\sigma = 0.01$ keV, the broad lines $\sigma = 0.8$ keV. PN and MOS2 are fitted independently. The listed values are the maximum values of PN or MOS2, respectively. The values in brackets are the formal significances of the lines.

Date	Narrow line			Broad line		
	EQW [eV]	Sign.	Flux [$10^{-13} \frac{\text{erg}}{\text{cm}^2 \text{s}}$]	EQW [eV]	Sign.	Flux [$10^{-12} \frac{\text{erg}}{\text{cm}^2 \text{s}}$]
2000-06-14	<19	0.3	<1.76	<120	0.6	<1.11
2000-06-15	<34	0.5	<3.10	<206	0.8	<1.87
2000-06-16	<28	0.2	<2.52	<220	1.0	<1.93
2000-06-18	<30	0.9	<2.68	<139	0.5	<1.25
2001-06-13	<25	0.5	<2.71	<123	0.5	<1.32
2001-12-16	<38	0.2	<5.05	<351	0.7	<4.44
2001-12-22	<55	0.1	<7.19	<458	1.1	<5.66
2002-01-09	<99	0.4	<9.18	<566	1.0	<5.01
2002-07-07	<150	0.4	<12.6	<333	0.7	<6.12
2002-12-17	<89	0.5	<9.94	<580	1.3	<1.80
2003-01-05	<42	0.6	<4.28	<190	0.4	<3.59
2003-01-05	<68	0.3	<6.42	<388	0.5	<3.67
2003-07-08	<74	1.0	<7.46	<376	0.9	<5.01

The Fe–line was fitted independently for PN and MOS2. Tab. 4.3 summarises the results of this systematic investigation. Next to the 3σ upper limits of the equivalent widths and fluxes, the significances of the line fits are provided.

Next to this systematic analysis additional investigations for a line feature are undertaken offering a Gaussian line with all parameters allowed to vary, in particular line energy and width. Only the redshift was fixed at the known value again. Only for one MOS2 observation the corresponding fits yield reasonable results. For all other observations the lines are unconstrained.

The most promising signature of a possible Fe–line was found in the MOS2 observation of 2000-06-16. The spectrum and the residuals of the absorbed power law fit are shown in Fig. 4.6 and Fig. 4.8. Between 5.5–6.0 keV there is a line–like excess visible in the ratio plot of MOS2, which is in agreement with the expected energy

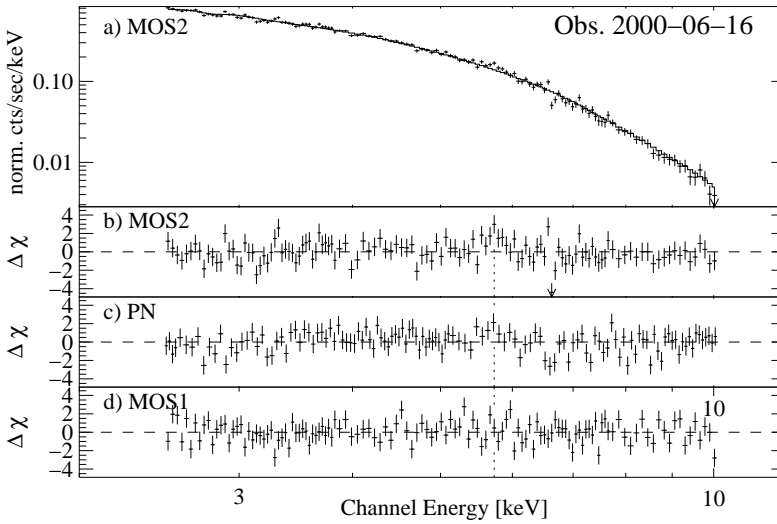


Figure 4.6: a) MOS2 spectrum of obs. 2000-06-16: Possible signature of an Fe–Line. The dashed line represents the line energy (observer frame) resulting out of the MOS2 fit. b) MOS2 residuals: Gaussian like residuals at level of $\sim 25\%$. c) Corresponding PN residuals: Despite of higher net effective area no clear line signature is present. d) Corresponding MOS1 residuals: Possible line signatures at lower and higher energies.

range for the redshifted neutral/ionised Fe- $K\alpha$ line. The residuals of the corresponding PN observation are plotted below those of MOS2. The presence of a possible line is also investigated using the MOS1 instrument, even though the general analyses of the MOS1 was skipped due to calibration problems.

The line-like residual of MOS2 obs. 2000-06-16 disappears if the redshifted ($z = 0.158$) Gaussian line is added to the fit model. The parameters of this line fit are (line energy in source reference frame):

$$\text{MOS2: } E = 6.65 \pm 0.08 \text{ keV}, \sigma = 0.12 \pm 0.13 \text{ keV}, \text{ and } I = 5.63 \pm 3.16 \cdot 10^{-5} \frac{\text{phot.}}{\text{cm}^2\text{s}}$$

$$(\text{PN: } E = 6.58 \pm 0.13 \text{ keV}, \sigma = 0.14 \pm 0.18 \text{ keV}, \text{ and } I = 2.67 \pm 2.09 \cdot 10^{-5} \frac{\text{phot.}}{\text{cm}^2\text{s}})$$

which corresponds to a total flux in the line of 3.91 (PN: 2.06) $\cdot 10^{-5}$ ergs $\text{cm}^{-2}\text{s}^{-1}$. The equivalent width of the line is $\text{EQW} = 51$ eV (PN: 23 eV). The χ^2 decreases

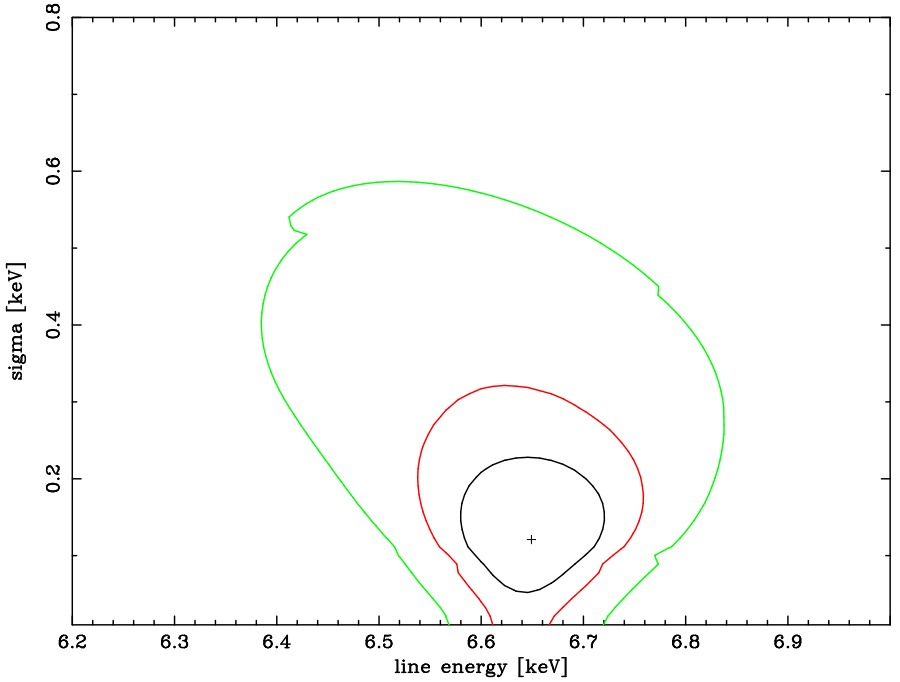


Figure 4.7: Contour plot σ -E of a possible Fe-line detection in MOS2 observation from 2000-06-16, showing 68, 90 and 99 per cent (innermost to outermost curves) confidence regions for two free parameters. The cross marks the best fit parameter values. The line energies are in source reference frame.

from 158.3/127 dof to 139.2/124 dof (PN: 146.5/128 dof to 137.9/125 dof) with an F -test⁴ probability of $1.13 \cdot 10^{-3}$ (PN: $5.52 \cdot 10^{-2}$). The significance of the line is low: $\sigma = 1.8$ for the MOS2 and $\sigma = 1.3$ for PN, respectively.

To gain a better impression whether the line is real or not, confidence contours are calculated both for normalisation versus energy (Fig. 4.1) and line width versus energy (Fig. 4.7). For both plots the line energy is in the source reference frame. The error contours show the 68, 90 and 99 per cent confidence regions for two degrees

⁴According to the publication by Protassov et al. (2002) using the F -test to investigate the probability of a line in a spectral model leads to an overestimation of the line probability. We use the F -test because the method is well known by the science community and our result is low significant anyway.

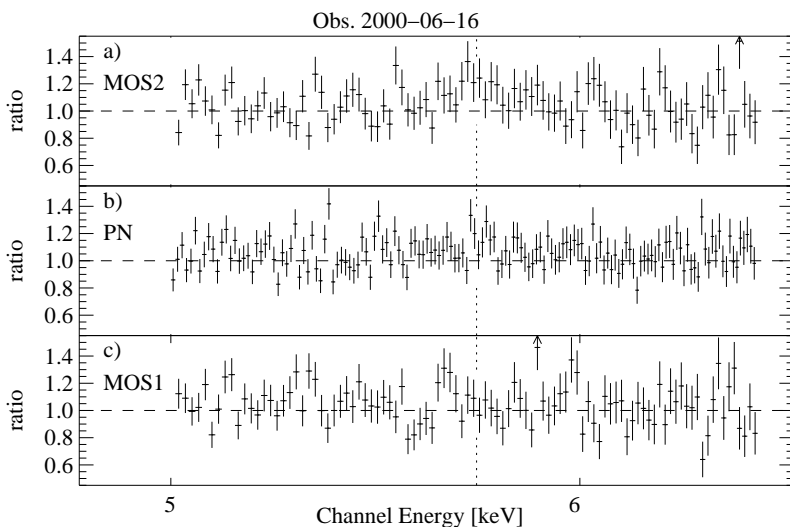


Figure 4.8: Obs. 2000-06-16: Ratios for an absorbed power law model of the un-binned spectra between 5.0–6.5 keV. The dashed line represents the line energy (observer frame) resulting out of the MOS2 fit of the binned spectrum. a) MOS2 ratios: Peak of Gaussian like residuals at level of $\sim 40\%$ at slightly lower energy as for the binned spectrum. b) Corresponding PN ratios: Ratios above 1, but double peaked structure. c) Corresponding MOS1 ratios: Possible line signatures at lower and higher energies.

of freedom. All three confidence levels of the normalisation versus energy contours are well defined. The 90% and 99% confidence regions in the σ -E plot pegged at the hard limit of zero, only the 68% contour is well defined around the best fit value represented as a cross in the center of the contours. Just considering the MOS2 stand-alone, these contour plots suggest a real detection of an Fe-line indicating a large contribution to the line of ionised matter, even if the significance of this detection is low.

So far the analysis of the Fe-line was done using binned spectra as described in Sect.3.1. Of course the line feature must also be present using the un-binned spectra. Having more than 250 counts per channel the χ^2 statistics still may be applied for these spectra. The ratios between 5.0–6.5 keV of all three detectors for an absorbed power law model are presented in Fig. 4.8. The un-binned 800 channel MOS2 spec-

trum shows an excess with a maximum level of about 40% at slightly lower energy than the best fit value for the binned spectrum. The un-binned spectrum confirms the possible detection of an Fe–line. Taking into account PN and MOS1, the conclusion must be different. The PN, having about twice the net effective area at 5–6 keV than a single MOS instrument, does not confirm the presence of an Fe–line. Though the ratios are above the unity, they do not show a Gaussian profile but a double peaked structure. The MOS1, known for showing a steeper spectral slope than MOS2 and PN, does show line like signatures but at different, slightly higher or lower energies. Summarising the results of all three detectors the detection of an Fe–line must be denied.

4.2 Soft Excess

For many AGN and quasars the X–ray spectrum in the energy range from 0.1–100 keV can be well described using an absorbed single power law model. As seen from the previous analysis this model is sufficient to describe the 3C 273 spectra at energies higher than 2.5 keV. Some sources show an excess of emission with respect to the single power law component at energies lower than 1–2 keV. This phenomenon is called *soft excess*.

According to the XMM EPIC status of calibration the MOS response at energies $E < 0.5$ keV is suspect, so only the PN camera is used to investigate the soft excess using the broadest available energy range of 0.3–10.0 keV. The galactic absorption is again fixed to $N_H = 1.79 \cdot 10^{20} \text{cm}^{-2}$ (Dickey & Lockman 1990).

All XMM observations of 3C 273 clearly prove the presence of a soft excess component. An example of the soft excess emission is shown in Fig. 4.9 b). The absorbed single power law model is a good description only for the high energetic X–ray spectra down to energies of about $E > 2$ keV. Below $E < 2$ keV the ascending slope of the soft excess emission steepens steadily. Between 0.4–0.5 keV the level of increase gets weaker. At energies below 0.3 keV the excess of soft emission decreases again. This general slope of the soft excess is uniformly for all XMM observations.

For the characterisation of this soft excess two different additional model components are tested: a second power law and a disk blackbody component. In both cases the power law component found at energies above 2.5 keV is fixed in both normalisation and slope. This fixation is justified by the good agreement in the cross calibration between XMM EPIC and RXTE PCA which surely verified this compo-

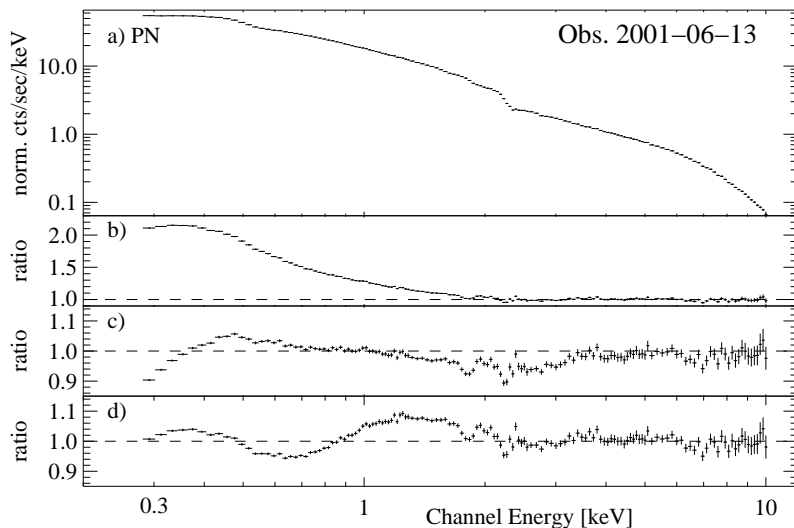


Figure 4.9: Obs. 2001-06-13: The 0.3–10 keV PN spectrum. a) Normalised count spectrum. b) Single power law model: The spectrum is fitted between 2.5–10.0 keV. At energies lower than ~ 2 keV the soft excess phenomenon is visualised. c) Double power law model: Break in the soft excess spectrum at 0.4–0.5 keV. d) Combined power law and disk blackbody model: Soft excess spectrum shows sinusoidal residuals.

ment up to about 20 keV.

Neither the double power law model nor the combined disk blackbody and power law model enable a satisfying fit to the spectra over the complete energy range of 0.3–10.0 keV. The fit results for both models are summarised in Tab. 4.4.

If the soft excess is described by a second power law component (Fig. 4.9 c) there is a kind of break in the residuals between 0.4–0.5 keV. This break represents the maximum of the ratio curve. The ratios descend to lower and higher energies, but the decrease to lower energies is clearly steeper than to higher energies. In the region of the transition between the two power law components the model fluxes are too high. Though the maximum offsets are moderate with about 10%, but due to the very high quality of the data the fit is very unsatisfactory.

Table 4.4: Fit results of soft excess models power law or disk blackbody including fixed galactic absorption of $N_{\text{H}} = 1.79 \cdot 10^{20} \text{cm}^{-2}$.

Date	Double power law			Disk blackbody + power law		
	Γ_{low}	Flux _{low}	χ^2/dof	T_{in}	Flux _{low}	χ^2/dof
2000-06-14	3.34±0.02	6.05±0.03	11.4	0.163±0.002	5.90±0.10	7.33
2000-06-15	3.29±0.02	5.83±0.04	5.29	0.168±0.002	5.64±0.15	5.60
2000-06-16	3.35±0.03	5.66±0.04	5.21	0.162±0.002	5.48±0.15	4.82
2000-06-18	3.50±0.02	5.69±0.04	8.70	0.150±0.002	5.53±0.12	5.02
2001-06-13	3.37±0.01	7.92±0.03	25.4	0.163±0.001	7.58±0.10	29.3
2001-12-16	3.22±0.05	8.84±0.12	2.81	0.171±0.004	8.61±0.45	1.75
2001-12-22	3.32±0.06	8.50±0.14	1.97	0.163±0.005	8.31±0.46	1.32
2002-01-09	3.12±0.02	5.08±0.04	12.1	0.195±0.002	4.92±0.17	4.39
2002-07-07	3.40±0.09	6.63±0.13	1.44	0.156±0.007	6.53±0.44	1.04
2002-12-17	3.34±0.05	9.83±0.14	2.80	0.162±0.004	9.61±0.48	1.63
2003-01-05	3.35±0.03	8.48±0.10	3.13	0.164±0.003	8.17±0.36	3.20
2003-01-05	3.18±0.04	8.35±0.02	2.48	0.177±0.003	8.04±0.40	3.10
2003-07-08	3.07±0.04	8.81±0.08	2.95	0.187±0.004	8.60±0.36	2.49

The power law indices of the soft component are definitely steeper than those of the hard component. The hard power law component is fitted by indices in the range of $1.6 < \Gamma_{\text{high}} < 1.8$, whereas the indices of the soft power law component is found to be in the range $3.1 < \Gamma_{\text{low}} < 3.5$. The interval for the soft power law indices show a broader distribution.

Fitting the data with the thermal disk blackbody component and the hard power law component (Fig. 4.9 d) the residuals below about 2 keV show a sinusoidal structure. In the range of 0.5–0.9 keV the model flux is above the data, in the ranges 0.3–0.5 keV and 0.9–2.0 keV the model flux is lower than the measurement. Again the maximum offsets are about 10%, but the fit is not acceptable. At energies above 2 keV the spectra are well modelled by the high power law component.

Using a thermal Bremsstrahlung model instead of the disk blackbody does not improve the fit results. The residuals for thermal Bremsstrahlung are similar to those of the disk blackbody. A redshifted absorber as additional component does not improve the fits, nor does an additional warm absorber model. Page et al. (2004) use several black body components for the spectral range of 0.5–2.5 keV to get acceptable fits due to the red. χ^2 , but the authors emphasise that modelling the soft excess spectrum with multiple black body components is probably not physical.

Comparing the fit values of the four 2000 June observations (Tab. 4.4), three observations (June 15–18) show a distinct trend: The power law indices are steepening from $\Gamma_{\text{low}} = 3.29 - 3.50$, the disk temperatures are decreasing from $T_{\text{in}} = 0.168 - 0.150$, respectively. The observation on 2000-06-14 does not follow this trend. For these analyses the high energetic spectra ($E > 2.5$ keV) are described by a single power law model. In Sect. 4.1.3 the presence of an edge-like residual in the high energetic spectrum of observation 2000-06-14 was discussed. If an additional edge component is included for this observation, the power law index hardens from $\Gamma_{\text{high}} = 1.64$ to $\Gamma_{\text{high}} = 1.62$, thus the contribution of the high energetic power law component to the soft excess emission decreases. Therefore the fit values for the soft excess model components changes: The low energetic power law index flattens to $\Gamma_{\text{low}} = 3.22 \pm 0.02$, the disk temperature increases to $T_{\text{in}} = 0.174 \pm 0.002$. Including the edge component into the fit model of observation 2000-06-14, the results confirm the trend found for the other three 2000 June observations.

CHAPTER 5

Variability

5.1 *Light Curves*

The available XMM observations presented in Tab. 3.1 enable the analysis on different time scales. The first one is the variability on short time scales of seconds up to several kiloseconds that is done for each of the individual observations. The large effective area of the X-ray telescopes provides adequate count rates even on the time scale of seconds. The upper time scale limit is given by the individual duration of the observations, typically between 5–60 ksec.

The set of observations also allows the analysis of the variability of the quasar 3C 273 on the time scales of weeks, months and years. In these analyses each individual observation is represented as a single data point. Of course the analysis of periodicity is impossible due to the low number of observations that are performed in irregular time intervals. But trends and possible indications for correlations may be present also in this rather small data set.

5.1.1 *Short Time Scales*

All individual observations are analysed for short time scale variations. The GTI corrected single event light curves of the source regions are used for these investigations. Due to the highest count rates of the EPIC instruments, the PN data allow for the shortest time scales. Thus the reported results are restricted to the PN instrument and its small window mode observations.

Tab. 5.1 summarises the mean count rates of the individual observations in two energy bands. The soft band is defined from 0.3–2.0 keV, the hard band from 2.0–10.0 keV. The time binning of the light curves is 10 seconds per bin. To investigate

Table 5.1: Average count rates of the individual EPIC PN small window mode light curves. Results of three intervals of 2.5 ksec (start, mid and end) and two energy bands per observation. The binning of the light curves is 10 seconds per bin.

Date	Energy	Count rates [cts/10 sec]			Exposure [ksec]	Filter
		Start	Middle	End		
2000-06-14	0.3–2.0 keV	180.9±13.5	179.3±13.4	180.3±13.4	65	med.
2000-06-15	0.3–2.0 keV	172.6±13.1	172.5±13.1	169.1±13.0	29	med.
2000-06-16	0.3–2.0 keV	168.3±13.0	167.0±12.9	167.7±13.0	30	med.
2000-06-18	0.3–2.0 keV	165.0±12.8	167.7±13.0	168.4±13.0	60	med.
2001-06-13	0.3–2.0 keV	232.3±15.2	234.4±15.3	234.8±15.3	88	med.
2001-12-16	0.3–2.0 keV	273.5±16.5		275.0±16.6	5	thin
2001-12-22	0.3–2.0 keV	262.8±16.2		261.3±16.2	5	thin
2002-07-07	0.3–2.0 keV	205.6±14.3		204.6±14.3	5	thin
2002-12-17	0.3–2.0 keV	303.7±17.4		307.3±17.5	5	thin
2003-01-05	0.3–2.0 keV	250.6±15.8	250.0±15.8	250.3±15.8	8	med.
2003-01-05	0.3–2.0 keV	259.5±16.1		259.1±16.1	5	thin
2003-07-08	0.3–2.0 keV	274.0±16.6	273.8±16.5	273.3±16.5	8	thin
2000-06-14	2.0–10.0 keV	38.5±6.2	38.5±6.2	39.6±6.3	65	med.
2000-06-15	2.0–10.0 keV	37.7±6.1	37.7±6.1	37.6±6.1	29	med.
2000-06-16	2.0–10.0 keV	36.7±6.1	36.8±6.1	37.8±6.1	30	med.
2000-06-18	2.0–10.0 keV	37.2±6.1	37.2±6.1	37.7±6.1	60	med.
2001-06-13	2.0–10.0 keV	43.8±6.6	46.0±6.8	45.9±6.8	88	med.
2001-12-16	2.0–10.0 keV	55.6±7.5		55.2±7.4	5	thin
2001-12-22	2.0–10.0 keV	57.2±7.6		57.6±7.6	5	thin
2002-07-07	2.0–10.0 keV	39.6±6.3		40.1±6.3	5	thin
2002-12-17	2.0–10.0 keV	52.7±7.3		53.0±7.3	5	thin
2003-01-05	2.0–10.0 keV	43.1±6.6	43.8±6.6	43.2±6.6	8	med.
2003-01-05	2.0–10.0 keV	42.7±6.5		42.8±6.5	5	thin
2003-07-08	2.0–10.0 keV	47.6±6.9	46.6±6.8	47.5±6.9	8	thin

changes in the mean count rates different 2.5 ksec long segments are provided, from the start, the middle and the end of the observations. For the short 5 ksec observations only two values are provided to avoid overlapping. Note that the comparison of the mean count rates of different observations must be done carefully, because the individual observations are performed using different filters, the thin and medium, respectively (see Tab. 3.1).

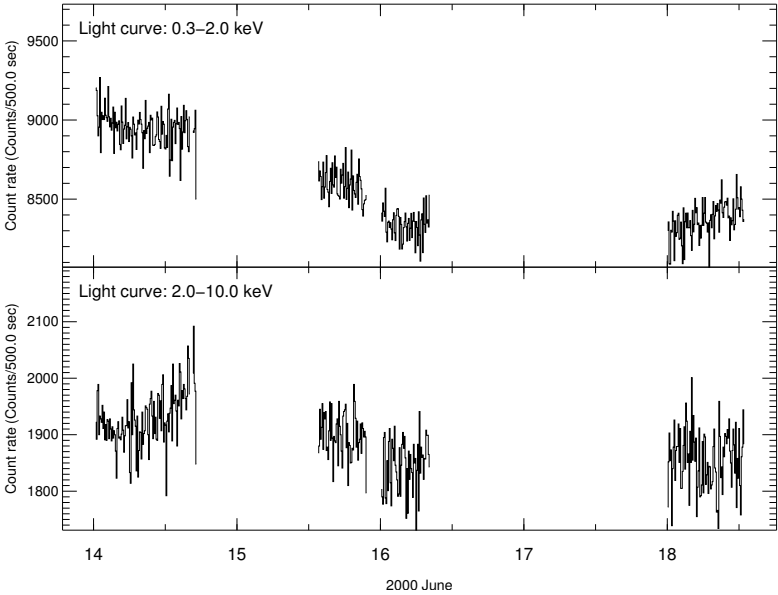


Figure 5.1: The 2000 June light curves of two energy bands. The binning of the plotted light curves is 500 sec. Upper panel: The 0.3–2.0 keV light curve. Lower panel: The 2.0–10.0 keV light curve.

If the time resolution of the individual light curves is reduced to 500 seconds (Fig. 5.1), changes of the count rates in the order of about one standard deviation are clearly visible in the light curves of the long observations. The changes between the 2000 June observations are significant with more than 8σ for the soft band, where the count rate drops from 9053 ± 95 to 8239 ± 91 within 2 days, between June 14–16. For the hard band the drop is also present, but less significant (3σ).

The light curves of observations 2000 June 14 and June 18 show different behaviour for the soft and hard band. While on June 14 in the soft band the count rate is decreasing during the first 6 hours of the observation from about 9000–8900 cts/500 s and then remains nearly constant, the hard band has a constant count rate for the first 10 hours and then it increases from about 1900–2000 cts/500 s. On June 18 the count rate of the hard band is more or less constant at about 1860 cts/500 s, whereas the count rate in the soft band is increasing from 8240–8400 cts/500 s. It is obvious that the soft band and the hard band show different evolutions.

The individual light curves do not show significant increases or decreases of the count rate, if a high time resolution of seconds or 10 seconds is selected (Fig. 5.2). The measured noise levels of the individual observations show over-statistical fluctuation indicating that the variations are not only statistical noise but the quasar 3C 273 itself contributes to the variations. Remarkable is the decline of the count rates on the order of one standard deviation at the daily observations from 2000-06-14 to 2000-06-16 in the soft band, whereas the change in the hard band is nearly negligible (see Tab. 5.1).

It is also investigated whether periodic signals are hidden in the noise of the individual light curves. Using the discrete Fourier transformation, the light curves are decomposed into sine wave components in the frequency domain. A detailed description of discrete Fourier transformation can be found in Pottschmidt (2002) or Benlloch-García (2003). If N is the total number of equally spaced time bins Δt of the light curve $x(t_k)$ with the observation time $T = N\delta t$, then the j^{th} element of the discrete Fourier transformation is defined as

$$FT(\omega_j) = \sum_{k=0}^{N-1} x(t_k) \exp(-i\omega_j t_k) \quad \text{for } j \in [-N/2, (N/2) - 1] \quad (5.1)$$

with ω_j representing the angular Fourier frequency $\omega_j = 2\pi j/T$ for $j = 1, \dots, N/2$.

The variability amplitude of the different frequencies is shown in a periodogram or power spectrum density (PSD). The PSD of a light curve is defined as the square absolute values of its Fourier coefficients, multiplied by a normalisation constant (Leahy et al. (1983), Miyamoto et al. (1991)).

$$P(\omega_j) = C \cdot |FT(\omega_j)|^2 \quad \text{for } j \in [0, \dots, N/2] \quad (5.2)$$

A periodic variation would appear inside the PSD as a peak with power higher than the noise distribution. The range of frequencies that is tested by this method is restricted by the total observation time and the time binning of the light curve. The limit for the highest frequency is the inverse of twice the binning time. For the PSD calculation a time binning of 1 sec was used for all observations. The limit for the lowest frequency is the inverse of half of the observation time (see Tab. 3.1 or Tab. 5.1).

In cases where the GTI correction forces gaps inside the light curve, these gaps can generate powerful peaks or curvatures in the PSD. Thus in case of gaps in the light curves the algorithm introduced by Scargle (1982) is used that enables reliable detections with the periodogram in the case where the observation times are unevenly spaced.

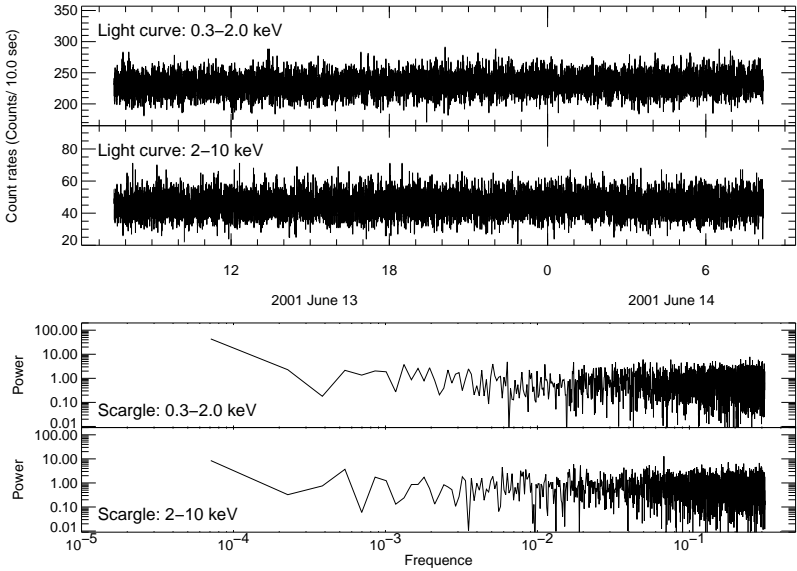


Figure 5.2: Example of short time scale variability. Upper panel: The light curves (0.3–2.0 keV; 2.0–10.0 keV) of observation 2001-06-13/14. The binning of the light curves is 10 sec. Lower panel: Scargle PSDs of the same observation.

No evidence for any periodic short time variability was found in the individual light curves of the XMM PN observations. Fig. 5.2 gives as an example the light curves and PSDs for the longest individual observation 2001-06-13 in two energy ranges, the soft band (0.3–2.0 keV) and the hard band (2–10 keV). For the PSD analysis a binning of 10 sec is used for all the individual light curves. The power is the same for all available frequencies. No peak with power in excess to the noise distribution power was found in the PSDs, indicating that there are no periodic variations on time scales between about 10–20000 sec.

Due to the non-curved appearance all the individual PSDs of both energy bands were fitted using the power law model $P = \text{const.} \cdot f^{-\alpha}$. The case of $\alpha = 0$ is called *white noise*, the power is equal for all frequencies. If the power decreases at increasing frequencies with $\alpha = 1$, this case is called $1/f$ -noise or *red noise*. All results are consistent with white noise.

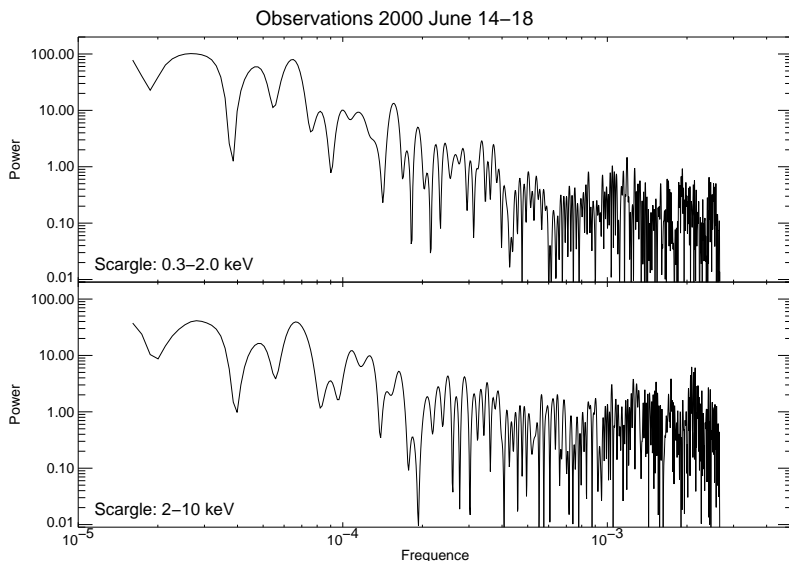


Figure 5.3: Source variability at frequencies $< 10^{-4}$ Hz. The PSDs of the light curves of observation set 2000 June 14–28 in two energy bands. The binning of the light curves is 500 sec and are presented in Fig. 5.1. Upper panel: Scargle PSD of the soft (0.3–2.0 keV) band. Lower panel: Scargle PSD of the hard (2–10 keV) band.

Only for the long observations (> 30 ksec) indications for an increase of the PSD are found. The PSD points at lowest frequency ($\sim 10^{-4}$ Hz) are well above the noise level (see Fig. 5.2). To verify that the quasar 3C 273 shows variability at frequency lower than $\sim 10^{-4}$ Hz, the durations of the individual observations are too short. Therefore we combined the 4 individual observations from 2000 June. The total observation time of this set of observations is about 180 ksec within a time range of 5 days.

Fig. 5.2 shows the PSDs for the soft and hard band of the 2000 June light curves presented in Fig. 5.1. For the soft band an increase of the PSD power is present starting at about $5 \cdot 10^{-4}$ Hz. For the hard band, this break point seems to be at a slightly lower frequency of about $3 \cdot 10^{-4}$ Hz. The PSD power at the lowest frequency is slightly higher for the soft band than for the hard band.

The set of 4 long observations within 5 days in 2000 June is also used for a first order structure function analysis. The concept of structure function has been introduced in astronomy by Simonetti et al. (1985). The first order structure function of a light curve $x(t)$ as a function of time lag τ is defined as:

$$SF_{x(t)}(\tau) = \langle (x(t+\tau) - x(t))^2 \rangle \quad (5.3)$$

For a stationary random light curve free of periodicities the structure function is related to the variance of the light curve and its autocorrelation function:

$$SF_{x(t)}(\tau) = 2 \cdot (\text{Var}(x) - \mathcal{A}_{x(t)}(\tau)) \quad (5.4)$$

While in theory it is completely equivalent to power spectrum analysis, the structure function has the advantage to work in the time domain which makes it less dependent on the sampling.

The general shape of a structure function can be described as follows: For short time lags the structure function has a lower plateau with an amplitude just twice the variance of the measured noise, because this noise (assumed Gaussian) has a zero correlation time scale. For lags longer than the longest correlation time scale there is a high plateau with an amplitude equal to twice the variance of the fluctuations. The slope of the curve linking these plateaus depends on the nature of the intrinsic variations of the source.

The structure functions from 2000 June light curves of the soft (0.3-2.0 keV, left) and hard (2.0-10.0 keV, right) band are presented in Fig. 5.4. The dotted lines are the corresponding calculated variance plateaus of the fluctuations. The time duration covered by the observation set is 391 ksec. The maximum time lag having the lowest reasonable sampling rate of about 3–4 is about 100 ksec. Thus for both bands no conclusion can be made at which time lag the structure functions reach the upper plateau. We can state that there is variability at least up to time scales to 10^5 seconds. Of course variability on longer time scales is possible. (For the cm-range Hughes et al. (1991) provided a lower limit of the characteristic time scale of 10 years.)

In both bands the structure functions show no steepening at time scales lower than about 10^4 seconds. This indicates that for both energy bands the measured source variability is dominated by Poisson noise at $\tau < 10^4$ seconds.

The obvious differences in these plots are the ratios between levels of the upper and lower plateaus. For the soft band the amplitude of the noise plateau is at about 10% the amplitude of the fluctuation plateau, whereas for the hard band the ratio is about

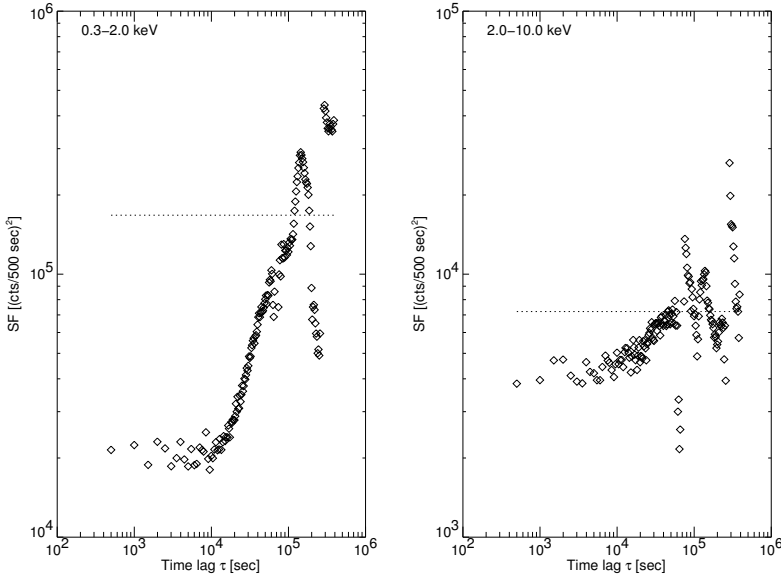


Figure 5.4: Structure functions of 2000 June light curve. The dotted lines represent the calculated variance plateau of the fluctuations. Left panel: The structure function of the soft band (0.3-2.0 keV). Right panel: The structure function of the hard band (2.0-10.0 keV).

40%. Therefore in the hard band the Poisson noise is stronger and the amplitudes of source variations are smaller than in the soft band.

To evaluate the slope of the structure function between the two plateau areas we fitted the data using the model:

$$SF_{x(t)}(\tau) = 2\varepsilon^2 + A \left(\frac{\tau}{\tau_{max}} \right)^\alpha \quad (5.5)$$

with the noise level ε , A is the difference of the variance level minus the noise level, τ_{max} being the start value of the variance plateau and the slope value α .

For the soft band we obtained a slope of $\alpha \approx 1.7$, a noise level $\varepsilon \approx 95$ and variance level of $A \approx 177\,000$ starting at $\tau_{max} \approx 95\,000$ sec. The corresponding fit values for the hard band are $\alpha \approx 0.6$, $\varepsilon \approx 43$, $A \approx 3\,800$ and $\tau_{max} \approx 100\,400$ sec. Because in our

structure functions neither the variance plateau A nor τ_{max} is defined, the resulting values can just be regarded as approximations.

5.1.2 Long Time Scales

For the analysis of the long time scale variability the individual observations are used as single data points. As time stamp for the data points the center of the observation is used with half of the observation duration time as 'time error', even if observation durations of a few ksec can not be resolved in a plot that covers three years. With the exception of the turn of the year 2000/2001 there is a data point roughly every half a year. These nearly equidistant observations enable an interpretation of the behaviour of the quasar on time scales of years. The total time base of three years is small for this subject, of course.

In addition there are some observations with offsets of only several days/weeks. These observations allow insights into the variability on these time scales. There are not enough data points to enable a detailed analysis, but they allow to judge whether significant variations are present at these time scales.

In Fig. 5.5 the long term light curves measured by the XMM EPIC PN camera are plotted for the fluxes in the total energy range (0.3–10 keV) as well as separated for the soft (0.3–2.0 keV) and hard (3.0–10.0 keV) energy bands. The plot for the hard band uses the flux errors of the PN fits of a single power law model in the range of 3–10 keV. The plot for the soft band uses the 0.3–2.0 keV flux errors of the PN fits of the double power law model with fixed hard power law component. The plot of the total fluxes uses the added flux errors of the soft and hard band.

The lowest fluxes are found at the start of the 3C 273 monitoring in 2000 June. The average flux of these four observations is $13.8 \cdot 10^{-11}$ erg/cm²s, with a weak indication of a flux decrease over the three observations from 2000-06-14 to 2000-06-16. On 2001 December the flux has increased to $20.4 \cdot 10^{-11}$ erg/cm²s. Both the fluxes of the soft and hard band are higher by the same factor of about 1.5 compared to the 2000 June observations. There is only one observation between these two extreme points on 2001 June, showing an intermediate flux level for the total flux as well as for the two energy bands.

The behaviour of the two observations in 2001 December needs some comments. The total flux is constant from Dec. 16th to Dec. 22nd. The splitting into the soft and hard band, however, shows that the contribution to the total flux of the soft and hard band is nearly equal for Dec. 16th. The flux at Dec. 22nd seems to increase in the hard band, whereas the flux in the soft band is decreasing. This increase of flux in the hard

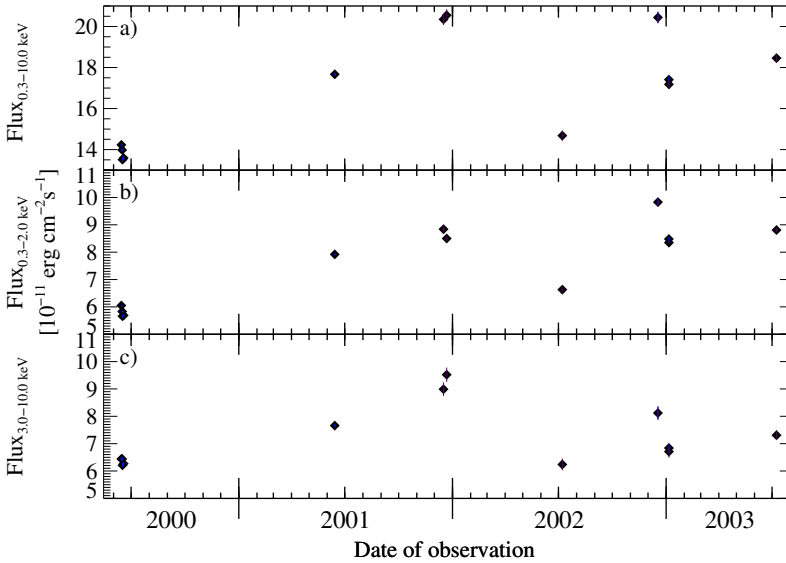


Figure 5.5: The long term variability of 3C 273 from 2000 Jun until 2003 Jan measured by EPIC PN. Where no error bars are visible the errors are within the diamonds. Fluxes are given in units of $10^{-11} \text{erg cm}^{-2} \text{s}^{-1}$. Upper panel: The total light curve (0.3-10.0 keV). Middle panel: The light curve of the low energy range (0.3-2.0 keV). Lower panel: The light curve of the high energy range (3.0-10.0 keV).

band is not seen for EPIC MOS2, but the PCA observations (see Fig. 5.7) indicate a flux increase in the hard band, too. The changes in the hard band are not significant neither for PN (1.5σ) nor for the PCA (2.0σ). Note that the hard component is fixed before the soft component is fitted. Due to the flux changes of the hard component the fit of soft component is forced to change, too.

In 2002 summer the brightness of the quasar dropped to $14.7 \cdot 10^{-11} \text{ erg/cm}^2 \text{ s}$, nearly the same level as in 2000 summer. The observation in 2002 December caught the quasar at a high flux level of $20.4 \cdot 10^{-11} \text{ erg/cm}^2 \text{ s}$ again. But contrary to the previous year the splitting into soft and hard band indicates that the contribution to the total flux of the soft band is higher than the contribution of the hard band.

Three weeks later in 2003 Jan the total flux dropped about 15% to $17.2 \cdot 10^{-11}$

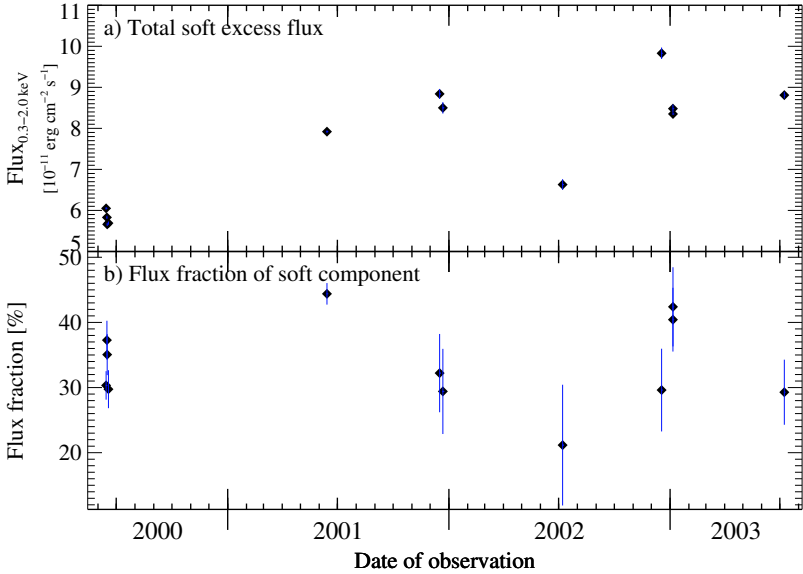


Figure 5.6: The long term variability of the soft power law component from 2000 June until 2004 January measured by EPIC PN. Fluxes are given in units of $10^{-11} \text{erg cm}^{-2} \text{s}^{-1}$. Upper panel: The light curve of the soft energy range (0.3–2.0 keV). Lower panel: The flux fraction of the soft power law component to the total 0.3–2.0 keV flux.

$\text{erg/cm}^2 \text{s}$. Still the quasar is brighter in the soft band than in the hard band. In 2003 summer the flux has slightly increased as well in the soft as in the hard band compared to 2002 December. The total flux is at $18.5 \cdot 10^{-11} \text{ erg/cm}^2 \text{s}$.

The contribution to the 0.3–2.0 keV flux of the hard power law component varies due to its luminosity changes as well as its spectral variability. Thus using the double power law model as characterisation of the soft excess, the contribution of the soft component to the total 0.3–2.0 keV flux is calculated and presented in Fig. 5.6. Less than 50% of the flux originate from the soft excess component. The varying fractions of the soft component to the total flux clearly show that the soft component is changing its luminosity, too. The flux variability of the soft component is different from the changes of the hard component. For example, the flux of the hard and soft components increase from 2001 summer to winter, but the relative contribution of the soft component to the total 0.3–2.0 keV flux is decreasing.

The monitoring observations of the quasar 3C 273 show clear evidence of strong flux variations of more than 50% ($13.5\text{--}20.4 \cdot 10^{-11}$ erg/cm²s) on time scales of months and years. There is also evidence for flux variations of about 15% on time scales of several days. The flux variability of the hard power law component is different from the evolution of the soft excess component.

5.2 Spectral Variability

Next to the brightness variations the spectral variability of the quasar is studied. None of the observations show any evidence of spectral variability within a single observation. Therefore this section refers to the long term variability of the spectral parameters.

5.2.1 Hard Component above 2.5 keV

The analysis of the RXTE data shows that a single power law model is sufficient to describe the spectral shape in the energy range above 2.5 keV. The EPIC PN and MOS2 results for this high energy power law component are consistent with the RXTE PCA results.

In Fig. 5.7 the fit results of a single power law model including galactic absorption for the energy range $E > 2.5$ keV is presented. The RXTE PCA results are plotted as open squares, the XMM EPIC PN results are plotted as diamonds. The upper panel shows the flux variations of the 3–10 keV band. It is the same plot as in the lower panel of Fig. 5.5 for PN, but now the RXTE results are included. As seen in the cross calibration of the two instruments, the results from PCA and EPIC are consistent with each other. The RXTE observations provide additional data points with offsets of several days to the XMM observations, especially for 2003 summer.

Some remarks must be made to the data point of the observation of 2002-01-09. The EPIC PN was not observing in small window mode but in timing mode. The resulting flux is significantly lower than the EPIC MOS2 and the RXTE PCA fluxes (see Tab. 4.1 and Tab. 4.2). The MOS2 and PCA fluxes are consistent with each other. Thus this PN data point was omitted in Fig. 5.7. The observation from 2002-01-09 is the only observation where the measured power law indices from EPIC ($\Gamma_{\text{PN}} = 1.71 \pm 0.02$) and PCA ($\Gamma_{\text{PCA}} = 1.59 \pm 0.05$) are not consistent within their error bars. The significance (2.2σ) of this difference is low.

While the 3–10 keV fluxes show strong variability, the power law indices do not

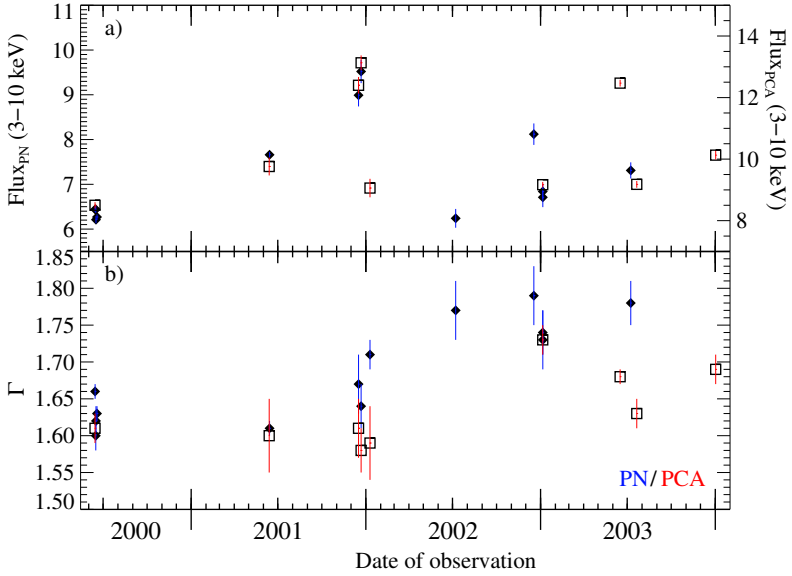


Figure 5.7: The long term variability of the hard (>2.5 keV) power law component from 2000 June until 2004 January measured by EPIC PN (diamonds) and RXTE PCA (open squares). Fluxes are given in units of 10^{-11} erg/cm²s. Upper panel: The light curve of the high energy range (3.0-10.0 keV). Lower panel: The power law indices Γ .

show variations from 2000 June until 2001 December. In this time period the observations are consistent with a constant power law index in the range of $\Gamma = 1.62 \pm 0.05$. Starting in 2002 summer the PN data points are consistent with a different softer power law index at $\Gamma = 1.76 \pm 0.03$, a steepening of the index of about 8%. The PCA result from 2002 December supports this possible second constant level, whereas the observations of 2003 and 2004 do not confirm this indication. From 2003-06-16 to 2003-07-08 the power law index softens from $\Gamma_{PCA} = 1.68 \pm 0.01$ to $\Gamma_{PN} = 1.78 \pm 0.03$ (3.2σ), and then it becomes harder again at 2003-07-21 to $\Gamma_{PCA} = 1.68 \pm 0.02$ (4.2σ). Due to the smaller error bars the significance of this index variations is higher than at the misalignment of the 2001-01-09 observations. The in general good agreement of PCA and EPIC indicates that these variations of the power law index are real.

5.2.2 Fe-Line

None of the observations shows a clear detection of neither a narrow nor a broad iron line. Therefore it is difficult to give a statement on the variability of this possible line interpreting the 3σ upper limits for equivalent widths and fluxes.

The equivalent widths (EQW) of the line upper limits clearly scale with the exposure times of the observations. The EQWs of the long observations are smaller than the EQWs of the shorter exposures. The flux limits vary by a factor of ~ 5 for the broad lines and by a factor of ~ 7 for the narrow lines, but they do not follow the general 3–10 keV band flux variations.

The variability found for the upper limits for a possible hidden iron line is presumably due to the differences in the statistics of the spectra.

5.2.3 Soft Excess

As characterisation of the soft excess both a double power law model and a combined disk blackbody and power law model is used. For both models the high energy power law component is fixed in shape and intensity to the values found at the 2.5–10 keV analyses. Galactic absorption is included at both models and is fixed to $N_{\text{H}} = 1.79 \cdot 10^{20} \text{ cm}^{-2}$ (Dickey & Lockman 1990).

A strong variability is found on time scales of days and weeks. But the insufficient fits ($1.0 \leq \text{red}\chi^2 \leq 29.3$) do not allow to be very conclusive. On the other hand the count rate analysis proves that the fluxes of the soft and hard band vary independently and therefore a change of the spectral properties is expected on these time scales.

Using a second power law component as characterisation of the soft excess, the indices of the soft power law component show a spreading between $3.07 \leq \Gamma \leq 3.50$. The evolution of the indices with time is plotted in Fig. 5.8. The dashed line inside the plot corresponds to the average value. Besides the strong variations on time scales of days and weeks there could be a soft decrease of the power law index over the years.

The results for the disk blackbody model are equivalent. The values for the temperature of the inner disk radius vary between $0.150 \text{ keV} \leq T_{\text{in}} \leq 0.195 \text{ keV}$. Next to the variations on shorter time scales there seems to be an increase of the inner disk temperature over the time range of the observation sample.

There is no correspondence to the possible presence of two different state levels as indicated by the spectral evolution of the hard power law component.

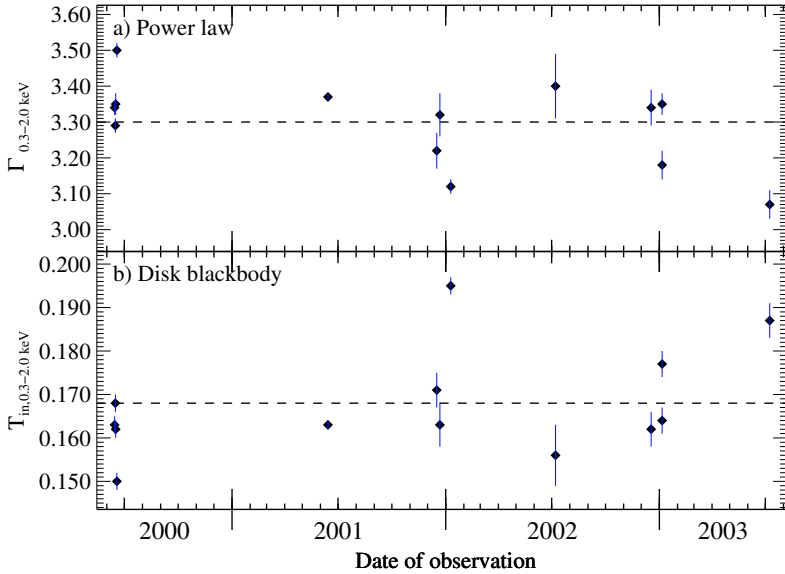


Figure 5.8: The long term spectral variability of the soft excess component from 2000 June until 2004 January measured by EPIC PN. The hard power law component is fixed before the soft excess is fitted. The galactic absorption is fixed to $N_{\text{H}} = 1.79 \cdot 10^{20} \text{ cm}^{-2}$. The dashed lines correspond to the average values. Upper panel: Double power law model. Lower panel: Combined disk blackbody and power law model.

Because the parameters for the high energy power law component were fixed, the fit of the soft excess component results in a well defined minimum providing very narrow error bars. Therefore the formal significances of the soft excess variations are high, even if the χ^2 statistic of the fit is unacceptable.

For most observations the parameters describing the spectral slope of the soft excess component jitter around the average value of $\Gamma_{\text{low}} = 3.30$ ($T_{\text{in}} = 0.168 \text{ keV}$) as shown in Fig. 5.8. Nevertheless, in several observations the values deviate significantly.

On 2003-01-05 there are two observations of 3C 273 within 4 1/2 hours. While the power law indices of the high energetic component are the same for both obser-

variations, the spectral parameters of the soft excess component show changes of 5.0 % ($\sigma = 3.4$) for the power law model and of 7.5% $\sigma = 3.0$ for the disk blackbody.

The shortest time scale for highly significant spectral variations provide the 2000 June observations. The four observations show a distinct trend (see Sect. 4.2). Whereas the first three of these observations are close to the average value, the last observation shows the steepest slope of all the XMM observations. Note that this is not the observation with the prominent edge-like feature. These variations within 5 days between the observations 2000 June 14–18 are highly significant. For the power law model the indices steepen by about 8% with a significance of $\sigma = 9.9$. The disk blackbody temperatures increase by 14% with a significance of $\sigma = 8.5$.

CHAPTER 6

Discussion

In the previous chapters the analysis of the X-ray observations was described. The observations were performed between 2000 and 2003 using RXTE and XMM-*Newton* satellites. The instruments of these satellites allow the spectral analysis over an energy range of 0.3–140 keV. The following sections are used to integrate the new results in the row of previously performed observations.

For the comparison of fluxes the results of the PN detector of the XMM EPIC instrument are used. The cross calibration of the detectors (Sect.4.1.3) proved that fluxes from all instruments can be compared.

6.1 *The power law component >2.5 keV*

The parameters determined with XMM-*Newton* for the power law component describing the 3C 273 spectra at energies >2.5 keV do fit very well into the ranges determined by previous observations. The power law indices vary in the range from $\Gamma = 1.60 - 1.79$, the 3–10 keV fluxes are between $6.2 - 9.5 \cdot 10^{-11} \text{erg cm}^{-2} \text{s}^{-1}$.

The first spectral analysis was published by Kellogg et al. (1971) using the first X-ray satellite Uhuru. They described the 2.4–6.9 keV spectrum by a power law with $\Gamma = 1.75 \pm 0.6$ and a flux of $6.6 \pm 1.0 \cdot 10^{-11} \text{erg cm}^{-2} \text{s}^{-1}$. The corresponding fluxes of the XMM observations are in the range of $4.9 - 7.4 \cdot 10^{-11} \text{erg cm}^{-2} \text{s}^{-1}$.

Variability of the X-ray intensity was discovered by the Ariel 5 experiment. The results, not available on the web, were published 1977 by K. Pounds in the proceedings of the 8th Texas Symposium on Relativistic Astrophysics. Worrall et al. (1979) confirmed the variability using the HEAO 1/2 experiments. They found a decrease of about 40% in the 2–10 keV flux values measured by HEAO 2 in 1977 December and in 1978 July ($11.1 - 7.4 \cdot 10^{-11} \text{erg cm}^{-2} \text{s}^{-1}$). No variability was found on time scales

of hours to 5 days. Also a variability of the spectral slope could not be discerned, the power law index was about $\Gamma = 1.5$ and consistent with previous observations. The flux range measured by XMM $7.9 - 12.4 \cdot 10^{-11} \text{erg cm}^{-2} \text{s}^{-1}$ is nearly the same as the one found by Worrall et al. (1979).

Analysing the data of a set of 13 individual observations using EXOSAT and Ginga between 1983–1988 Turner et al. (1990) for the first time found evidence of spectral variation. Especially the better sensitivity and energy resolution of Ginga proved the hardening of the power law slope from $\Gamma = 1.5$ to $\Gamma = 1.4$ in the 1.5–35 keV energy range, significantly flatter than those found in the present study. The measured 2–10 keV fluxes, varying between $5.9 - 16.8 \cdot 10^{-11} \text{erg cm}^{-2} \text{s}^{-1}$, again confirmed the variability of the X-ray fluxes.

ASCA observations in 1993 confirm a variation of the power law index (Capri et al. 1998). In their results the indices were in the range of $1.52 \leq \Gamma \leq 1.62$. The 2–10 keV fluxes, between $12.2 - 17.7 \cdot 10^{-11} \text{erg cm}^{-2} \text{s}^{-1}$, show weak variability. Compared to the XMM observations the flux level of the quasar during these ASCA observations was higher. The ASCA observations for the first time show a statistically significant evidence that the index Γ and flux are anti-correlated, i.e. a spectral hardening as the source brightens.

This anti-correlation was tested by Kataoka et al. (2002) using two observation campaigns (1996–1997, 1999–2000) with RXTE. The 2–10 keV fluxes show strong variability during the observations in 1996–2000: from $25.5 \cdot 10^{-11} \text{erg cm}^{-2} \text{s}^{-1}$ at the brightest to $6.2 \cdot 10^{-11} \text{erg cm}^{-2} \text{s}^{-1}$ at the faintest. During the first campaign 1996–1997 (166 observations) the power law indices do not show an anti-correlation with the flux: The spectral shapes do not change significantly despite large flux variations. In contrast, this anti-correlation has been found again for the 1999–2000 campaign (64 observations): The spectral index becomes smaller when the source is brighter, thus confirming the ASCA result.

We also tested this correlation using the results of the XMM/RXTE observations. Fig. 6.1 shows the fluxes versus power law indices for spectra $>2.5 \text{ keV}$. No anti-correlation between fluxes and power law indices can be found. For low fluxes the indices cover the whole range from $\Gamma = 1.59 - 1.77$. For high fluxes the range of the index values is smaller and concentrated between $\Gamma = 1.58 - 1.68$. Observations with high flux levels do not show spectral slopes steeper than $\Gamma = 1.7$, which would correspond to the anti-correlation found with ASCA and RXTE (1999–2000).

The indication of the possible two states seen in Fig. 5.7 is very weak. It is possible

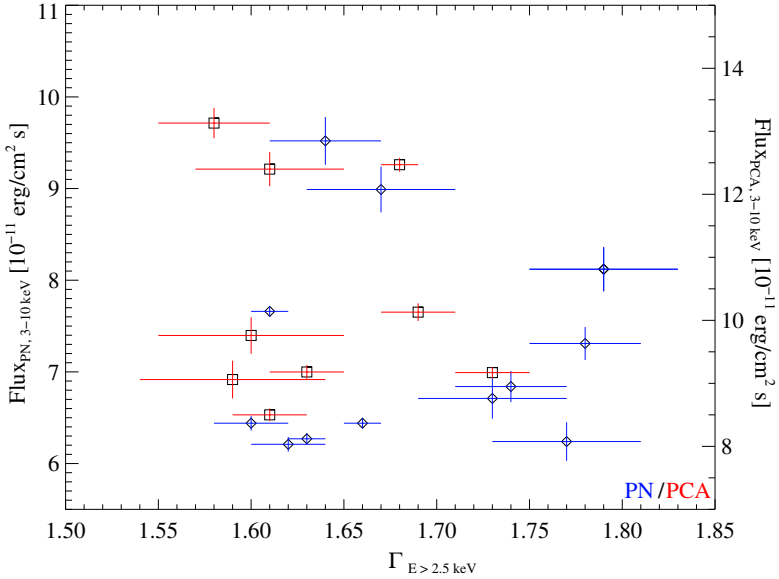


Figure 6.1: Flux versus power law indices for spectra >2.5 keV. PN data are represented as rhombs, PCA as squares. The flux scales (PN left, PCA right) correspond to the results of the cross calibration (compare e.g. Fig. 5.7).

to divide the data points at $\Gamma = 1.7$ into two states, but this idea is not really supported by the data.

Fig. 6.1 indicates another interpretation: two states showing different flux levels but covering the whole range of power law indices. Only the state having higher fluxes clearly shows the anti-correlation of flux and indices, whereas in the low flux regime the whole range of power law indices is covered. This low flux state would be in contradiction to the result of the RXTE 1996-1997 campaign (Kataoka et al. 2002). When they plotted the power law indices versus the corresponding fluxes, the more or less constant power law indices covered the whole flux range.

Compared to previous results, the 2–10 keV flux levels found by XMM of $7.9 - 12.4 \cdot 10^{-11} \text{ erg cm}^{-2} \text{ s}^{-1}$ are more in the lower range of observed fluxes. The faintest XMM observation is about 25% brighter than the faintest observation by Ginga in 1987, whereas the brightest XMM observation is about half as bright as the brightest observation by RXTE in 1996. Using the new value of the Hubble constant of

$H_0 \sim 70 \text{ km s}^{-1} \text{ Mpc}^{-1}$ (Freedman et al. 2001; Spergel et al. 2003) the corresponding luminosities are in the range of $5.0 - 8.1 \cdot 10^{45} \text{ erg s}^{-1}$.

Accretion is assumed to be the energy source for the tremendous luminosity. Because the observed flux range is the same for the last three decades, the average accretion rate must be constant over the covered period of 3C 273 observations.

The power law indices vary between $1.60 \leq \Gamma \leq 1.79$. As a possible emitting process for the high energy power law unsaturated Comptonisation with low energy seed photons from the accretion disk is discussed. The power law index (energy index α) then depends on the Compton y parameter, which describes the average fractional energy change per scattering correlated with the mean number of scatterings (Rybicki & Lightman 1979):

$$\alpha = -\frac{3}{2} + \sqrt{\frac{9}{4} + \frac{4}{y}} \quad (6.1)$$

with y for nonrelativistic thermal distribution of the electrons:

$$y = \frac{4kT}{mc^2} \text{Max}(\tau_{\text{es}}, \tau_{\text{es}}^2). \quad (6.2)$$

The change from $\Gamma = 1.60$ to $\Gamma = 1.79$ ($\alpha = 0.60$ to $\alpha = 0.79$) could result from a drop of 38% in the electron temperature kT_e or a corresponding change of the optical depth τ_{es} .

The power law indices found by XMM are higher than the canonical value of $\Gamma = 1.5$ found in observations before 1990. The complete set of observations with ASCA (1993: $\Gamma = 1.52 - 1.62$), BeppoSAX (1997 Jan.: $\Gamma = 1.52 - 1.64$), RXTE (1996-1997: $\Gamma = 1.48 - 1.70$; 1999-2000: $\Gamma = 1.51 - 1.68$) and XMM (2000-2003: $\Gamma = 1.60 - 1.79$) indicates a slow softening of the average power law spectrum over the last decades. The development of the hard X-ray power law index is visualised in Fig. 6.2.

6.2 The Fe-Line

Although for all of the 3C 273 observations discussed in this work a single power law model is sufficient to describe the spectral shape between 3–20 keV, there are several publications about detections of iron line emission.

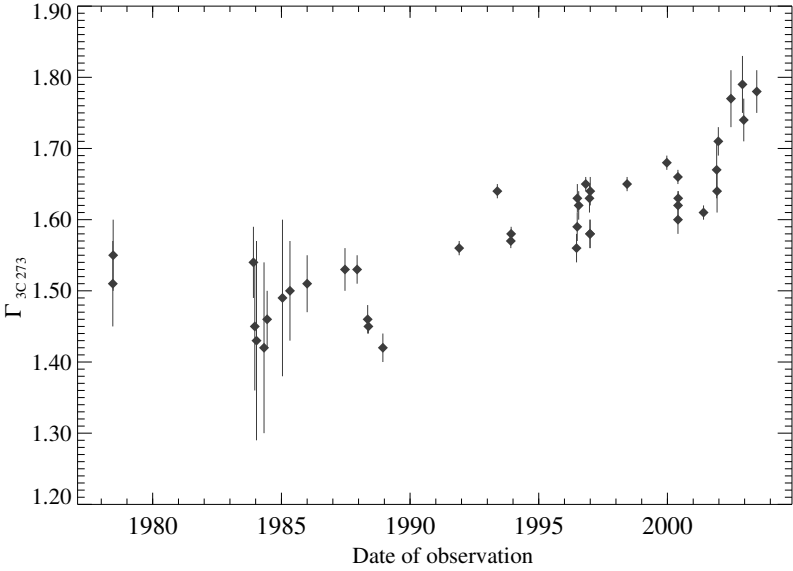


Figure 6.2: Development of the hard X-ray power law index for 3C 273. Before 1990 a canonical value of about $\Gamma = 1.5$ was accepted for the hard X-ray power law index. During the last decade the power law index increased significantly.

In a *Ginga* observation performed on 1987 July Turner et al. (1990) found a significant excess near 5 keV that was well fitted by a neutral Fe-line with an equivalent width (EQW) of about 50 eV. This value was compatible with the upper limit of 38 eV for previously performed HEAO1-A2 observations (Worrall et al. 1979). Grandi et al. (1997) identified a neutral iron line with an EQW of about 30 eV using a *BeppoSAX* observation. The Gaussian line width could not be constrained in these observations.

Analysing a set of *ASCA* and *RXTE* observations, Yaqoob & Serlemitsos (2000) were the first who could resolve a broad neutral Fe-line in one of these observations on 1996 July. The intrinsic width of the line was about 0.8 ± 0.3 keV. Using this value for their set of observations performed on 1993, 1996, 1998 and 2000, they got EQW between 43–133 eV and line intensities between $0.6 - 2.1 \cdot 10^{-4}$ photons $\text{cm}^{-2}\text{s}^{-1}$.

The presence of this broad line was confirmed by Kataoka et al. (2002) who published nine detections of broad line features using *RXTE* data from 1996–1998, partly the same observation as published by Yaqoob & Serlemitsos (2000). Because the line

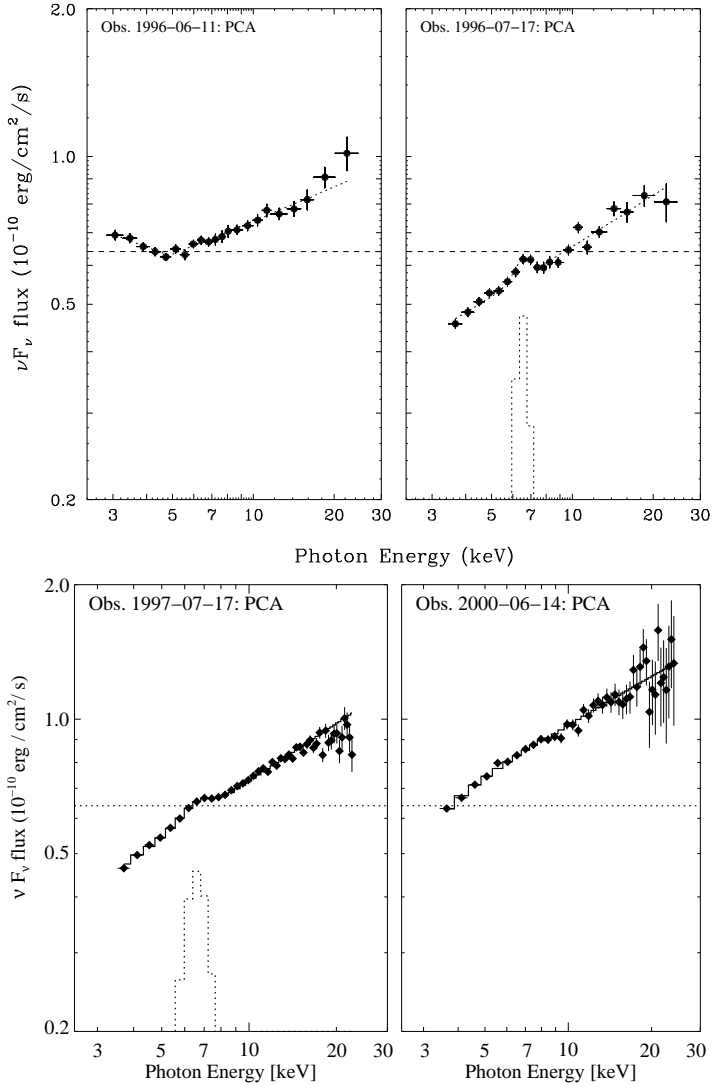


Figure 6.3: Discussion of Fe-line feature in 3C 273 PCA spectra. Upper panel: Spectra published by Kataoka et al. (2002) when a soft excess (left) and broad-line feature (right) are present. Lower panel: The re-analysed Kataoka-spectrum (left) and the PCA spectrum of 2000-06-14 (right) which is the PCA observation of our sample showing the lowest flux. The dashed lines indicate the upper flux limit of the line feature of the observation from 1996-07-17.

width could not be constrained a fixed value of 0.8 keV was used. The resulting EQWs were between 117–210 eV and the line intensities were between $1.7 - 5.4 \cdot 10^{-4}$ photons $\text{cm}^{-2}\text{s}^{-1}$.

To care for effects caused by changes in the calibration of RXTE I re-analysed the PCA observation from 1996 July. The presence of the neutral broad line can be confirmed. Because the line width could not be constrained, the published value of 0.8 keV was used. The line energy was found to be $E_{\text{Fe}} = 6.42 \pm 0.14$ keV with a line intensity of $1.6 \pm 0.2 \cdot 10^{-4}$ photons $\text{cm}^{-2}\text{s}^{-1}$. The EQW was 131 eV. The 2–10 keV continuum flux is about $7.9 \text{ erg cm}^{-2}\text{s}^{-1}$. The results are in very good agreement with the ones found by Yaqoob & Serlemits (2000).

Fig. 6.3 compares the PCA spectra from 1996 July published in Kataoka et al. (2002) with the PCA observation from 2000-06-14 showing the lowest flux of all PCA observations discussed in this work. The re-analysed spectrum of the 1996 July observation is added to visualise effects of the instrument calibration. The upper flux level of the iron line of observation 1996-07-17 published by Kataoka et al. (2002) is indicated in all plots by a dashed line. The continuum flux of 3C 273 on 2000-06-14 was higher than the line flux measured on 1996-07-17. If the line flux is constant, the line is hidden by the continuum flux in all observations discussed in this work.

The 2–10 keV continuum fluxes of the PCA observations between 2000–2004 are in the range of $10.4 - 16.2 \cdot 10^{-11}$ erg $\text{cm}^{-2}\text{s}^{-1}$. The corresponding quasi simultaneous XMM observations do not show signatures of neither a narrow nor a broad Fe–line. If the reason for the absence of the line is the flux level of the continuum, then previously published observations showing line features should have lower continuum flux levels.

The continuum fluxes of the observations in 1993, 1998 and 2000 published by Yaqoob & Serlemits (2000) were between $10.7 - 16.8 \cdot 10^{-11}$ erg $\text{cm}^{-2}\text{s}^{-1}$ and are in the same flux range as the XMM observation sample. The 1996 July observation, used to determine the line width, showed the lowest flux with $6.9/8.7$ erg $\text{cm}^{-2}\text{s}^{-1}$ (PCA/ASCA) which is lower than our sample.

Kataoka et al. (2002) found broad–line features in nine observations, six of these were performed between 1996 July 16–18¹. The published 2–10 keV continuum fluxes of these 1996 July observations were between $8.2 - 9.3 \cdot 10^{-11}$ erg cm^{-2} and

¹These observations correspond to the summed spectra of 1996 July used by Yaqoob & Serlemits (2000) and myself.

are in agreement with the values found by Yaqoob and myself. Three further observations from 1998 and 1999 had higher 2–10 keV continuum fluxes of $13.1 - 22.4 \cdot 10^{-11} \text{ erg cm}^{-2} \text{ s}^{-1}$).

These detections of line features when the 2–10 keV continuum fluxes of 3C 273 are in the same flux range or even higher than at the XMM observations support the assumption that the iron line is rather variable than constant.

6.3 *The soft excess*

The soft excess component of 3C 273 is verified in all XMM spectra of the analysed observations. The soft excess emission is identified up to the energy of about 2 keV. Neither a power law model nor the disk blackbody model is a good description of the soft excess component.

The soft excess component was discovered by Turner et al. (1990) using EXOSAT. They found an excess of emission at energies below ~ 1 keV that showed flux variability of a factor ~ 2 in about 20–40 days. The contribution of this soft component to the total flux at energies below ~ 1 keV was lower than 20%.

The ROSAT satellite with its energy range of 0.2–2.4 keV confirmed the variable soft excess component. Staubert et al. (1992) described the ROSAT spectra from 1990 June and December using an absorbed single power law model. The resulting indices were significantly steeper ($\Gamma_{\text{Jun.}} = 1.84 \pm 0.05$, $\Gamma_{\text{Dec.}} = 2.29 \pm 0.08$) than those observed in the 2–10 keV range (average $\Gamma_{\text{high}} \approx 1.5$).

Combining simultaneous observations by ROSAT and Ginga, Staubert (1992) determined the high energy power law with Ginga (2–20 keV, $\Gamma_{\text{high}} = 1.56 \pm 0.10$) and fitted the soft excess observed by ROSAT using this result plus a second power law component. The resulting soft excess power law index was $\Gamma_{\text{low}} = 3.5 \pm 0.4$. Again the soft component was visible at energies below ~ 1 keV. This soft excess index corresponds to the steepest value of the index range found by XMM. The high energy component of the corresponding XMM observations was similar ($\Gamma_{\text{high}} = 1.63 \pm 0.01$). Using high signal to noise ROSAT PSPC data Leach et al. (1995) found that the soft excess is better modelled by a power law component than a thermal emission model. Fixing the hard power law index at $\Gamma_{\text{high}} = 1.5$ the soft excess power law indices were in the range $2.40 \leq \Gamma_{\text{low}} \leq 2.79$. They also verified that the variability of the soft band (0.1–0.3 keV) and the hard band (1.5–2.4 keV) is uncorrelated.

Cappi et al. (1998) confirmed the results of the simultaneous ROSAT/Ginga observation, that a power law component is the best description for the soft excess component, with ASCA observations. The indices of a double power law model were $\Gamma_{\text{low}} = 3.0 \pm 0.8$ and $\Gamma_{\text{high}} = 1.59 \pm 0.09$.

A quasi-simultaneous observation of BeppoSAX and ASCA in 1996 July again confirmed a double power law model as the best description of the 0.1–10 keV spectrum. At energies <0.5 keV the soft excess component was detected. The spectral parameters are consistent with previous results ($\Gamma_{\text{low}} = 3.1, \Gamma_{\text{high}} = 1.6$). In addition Orr et al. (1998) confirmed the first detection of signatures of an additional absorber component at about 0.7 keV by Grandi et al. (1997) in the BeppoSAX observation using the quasi-simultaneous ASCA data. So far, no further detections of warm absorber signatures have been reported.

The soft excess component was nearly not detectable at BeppoSAX observations in 1997 January. In two out of four observations Haardt et al. (1998) found marginal indications for the presence of a soft excess at energies lower than 0.2 keV.

The previous extraction of soft excess publications clearly shows that the high energy end, where soft excess emission is detected, is highly variable. It covers the energy range from >0.2 keV, when the soft excess is nearly not detectable, up to about 2 keV as found with XMM in this work. The RXTE observation published by Kataoka et al. (2002) (see Fig. 6.3) indicates that this high energy end could even reach up to about 4 keV.

The soft excess is assumed to be a signature of the innermost region of an accretion disk. The main emission of the accretion disk is emitted in the optical/UV and is referred to as the "big blue bump" in the 3C 273 broadband spectrum. The innermost region is expected to have the highest temperatures, therefore thermal emission of soft X-rays is expected. The soft excess is interpreted as the high energy end of the "big blue bump". Using this model, the variability of the high energy end of the soft excess must be interpreted as a temperature variation of the innermost region of the accretion disk. Because the disk temperature depends on the radius/distance to the central black hole, these variations could be an indication of a variability of the inner accretion disk radius.

A possible correlation between the soft excess fluxes and its spectral slopes is investigated as well as a possible relation between the hard and soft band model parameters. Because the results of the thermal model are comparable, a steepening of

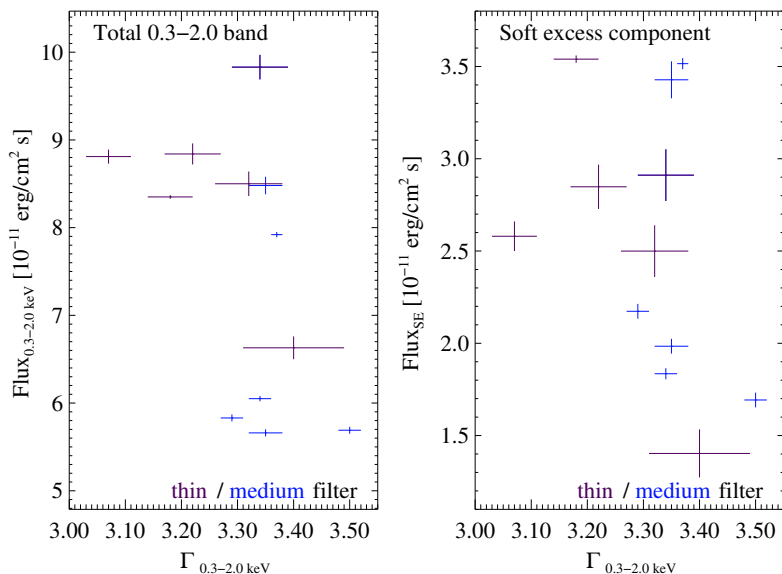


Figure 6.4: Correlation of fluxes versus power law indices of the soft excess model parameters. Left panel: Total fluxes of the 0.3–2.0 keV band including the contribution of the high power law component. Right panel: Fluxes of the soft excess component only.

the spectral slope leads to an increase of the power law index or alternatively to a decrease of the disk temperature (see Fig. 5.8), the analysis is restricted to the absorbed double power law model.

Fig. 6.4 presents the relation between fluxes and power law indices. The power law indices are the same in both panels, but the fluxes are different. The left panel presents the total flux in the 0.3–2.0 keV band including the contribution of the high power law component, whereas the right panel shows the flux of the soft excess component only. The contributions of the soft excess flux to the total soft band flux have been presented in Fig. 5.6.

No obvious correlation can be found between the fluxes and spectral slopes of the soft excess neither for the total fluxes nor for the soft excess component only. The linear Pearson correlation coefficients are $r = -0.21$ for the left plot and $r = -0.30$ for the right one. Whereas for the total flux there are four data points at lowest flux level

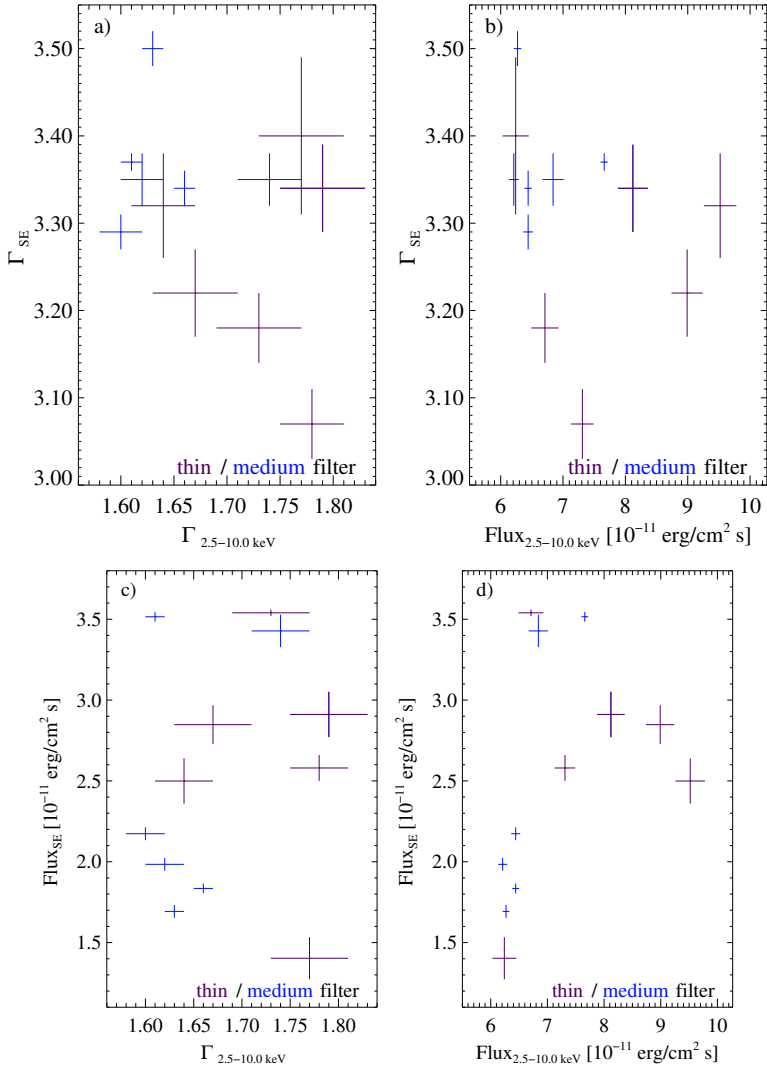


Figure 6.5: Correlations between the soft and hard band parameters. a) Soft excess power law index versus high power law index. b) Soft excess power law index versus flux of high power law component. c) Soft excess flux versus high power law index. d) Soft excess flux versus flux of high power law component.

and just one at the highest, for the soft excess component only, it is vice versa. Three data points are at highest flux level and just one at the lowest. As the contribution of the soft component to the total 0.3–2.0 keV flux is lower than 50%, the differences in these plots suggest an independent variability of the soft and hard component.

For the investigations of possible relations between the model parameters of the soft and hard power law component, the four possible parameter constellations were analysed. Fig. 6.5 a+b present the soft excess slopes versus the slopes and fluxes of the high power law component, whereas Fig. 6.5 c+d display the flux of the soft excess component versus the slopes and fluxes of the high band.

The distribution of the soft and hard power law indices (Fig. 6.5 a) does not show any correlation ($r = -0.36$). Most observations show a soft power law index of $\Gamma_{\text{low}} = 3.3 - 3.4$. The corresponding high power law indices cover the whole range from $\Gamma_{\text{low}} = 1.6 - 1.8$. There are two outliers at extreme index combinations. One observation shows a very steep soft spectrum with a correlated flat high energy spectrum. Vice versa the observation with the flattest soft excess spectrum is related with a steep high energy spectrum.

Also Fig. 6.5 b) does not show any correlation ($r = 0.09$). When the hard band has low flux steeper as well as flatter spectra can be observed. For larger fluxes in the hard band there are not enough data points to enable a statement about the soft index distribution. The few data points vary between $\Gamma_{\text{low}} = 3.2 - 3.4$, indicating that the soft indices also are spread over a wider range.

The soft excess fluxes are not related to the spectral slope of the high energy component (Fig. 6.5 c, $r = 0.15$). The corresponding high power law indices of observations with low soft excess fluxes vary over the complete observed parameter range as well as those of high soft excess fluxes.

Only Fig. 6.5 d) containing the soft and high band fluxes show a kind of grouping of the data points. One group of data points is at the low flux end of both bands. Observations with low soft excess fluxes have also low fluxes in the hard band. The other way around this is not true any more, because observations with low fluxes in the hard band have counterparts with high soft excess fluxes, too. A second group of data shows an anti-correlation of the fluxes. If the fluxes of the hard band increase the soft excess fluxes decrease. The soft excess flux at high hard band fluxes is still brighter than for the first group. One data point is just in between these two groups. So these structures are most likely due to the small observation sample and will presumably disappear if more observations are available. Taking all data point

into account the linear Pearson correlation coefficient is $r = -0.01$, indicating that the two parameters are not linearly related.

All figures showing soft component parameters to the hard band parameters require the conclusion that the variations of the soft excess component are independent from the high energy power law component. Therefore the emission regions for the soft excess and the high energy power law must be different and independent.

6.4 *Origin of the X-ray emission*

Multi-wavelength observations showed that the X-ray flux is not coupled to the fluxes in all other wavebands. Courvoisier et al. (1990) concluded that the self-Compton process is not the source of the X-ray photons. If the X-ray photons are produced by inverse Compton scattering the lack of correlation implies that the physical conditions of the Comptonising medium must be variable.

In Walter & Courvoisier (1992) the authors discuss that if Comptonisation is the source of the X-ray photons, the slope of the X-ray power law continuum is also variable and its variations are correlated to the same physical conditions and therefore may be correlated to a function of both X-ray and soft seed photons luminosities rather to only one of them. In this case the ultraviolet big blue bump component must play an important role as it is the brightest source of soft photons being able to be Comptonised. As the soft excess component is interpreted to be the high energy end of this big blue bump, the soft excess emission could also participate in a possible correlation.

If the energy distribution of the Comptonising electrons is purely non thermal, the X-ray spectral slope is determined by the slope of this distribution. This slope depends on the acceleration mechanism of the electrons and the cooling rate proportional to the soft photon luminosity. The acceleration mechanism is probably independent from the soft photon luminosity. For this model it is difficult to explain the value of the power law index and its small variation. The luminosity of the seed photons vary periodically by a factor of two, therefore as well the cooling rate associated with this luminosity. But the observed power law slope is shown to be quasi-constant for more than ten years.

On the other hand, if the width of the electron energy distribution is significantly less than the extension of the X-ray spectra, the Comptonisation may be considered

as thermal. In this case the X-ray spectral slope is not only determined by the electron temperature but also by the Thomson optical depth of the Comptonising medium. As the ratio of the X-ray and seed photon count rates is basically proportional to this optical depth, a relation between this ratio and the slope of the X-ray power law is expected (Walter & Courvoisier 1992).

A cloud of hot electrons with a temperature θ (in units of $m_e c^2$) and the optical depth τ must be optically thin to produce variations of the spectral slope at energies $< \theta$. If the soft photon source is outside of the hot cloud, the hard X-ray power law index can be derived analytically (Rybicki & Lightman 1979):

$$\alpha = -\frac{\ln \tau}{\ln(A)} \quad (6.3)$$

where $A(\theta)$ is the amplification factor of the Compton scattering. In case of an optically thin source, the ratio of the photon luminosities in the hard X-ray power law C_{pwl} and the soft seed photon component C_{soft} may be written

$$\frac{C_{\text{pwl}}}{C_{\text{soft}}} = \eta \tau \quad (6.4)$$

with η being the covering factor of the Comptonising clouds above the source of the soft seed photons. Thus for thermal Comptonisation an anti-correlation is expected between the power law index and the ratio of the photon luminosities in the power law and the soft seed photon component:

$$\alpha \sim -\ln \left(\frac{C_{\text{pwl}}}{C_{\text{soft}}} \right) \quad (6.5)$$

As mentioned above, the ultraviolet big blue bump component is expected to be the source of the soft seed photons. Walter & Courvoisier (1992) found this anti-correlation between the X-ray power law index and the logarithm of the ratio of the X-ray and ultraviolet count rates in 3C 273 analysing simultaneous X-ray and ultraviolet observations obtained 1984–1988 with EXOSAT or Ginga and IUE. Substituting the ultraviolet count rate with the soft excess count rate, the correlation was not obvious any more.

We also tested this anti-correlation using the results of the XMM observations. Fig. 6.6 shows the correlation of X-ray power law index and the logarithm of the photon flux ratios of the 2–10 keV flux and the soft excess component (0.3–2 keV) flux. The linear Pearson correlation coefficient is $r = -0.09$, indicating that no relation between both parameters is found.

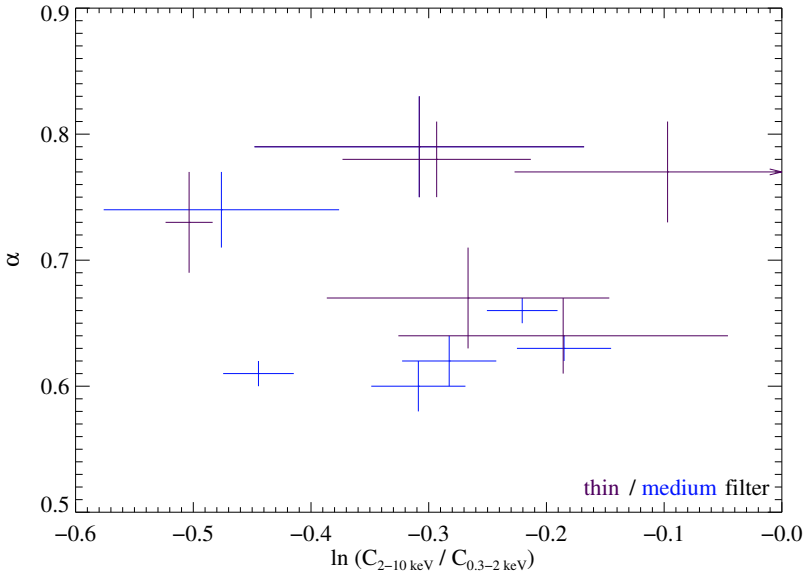


Figure 6.6: Correlation of X-ray power law index and the logarithm of the photon flux ratios of the 2–10 keV flux and the soft excess component (0.3–2 keV) flux.

Possibly the basic assumption that thermal Comptonisation is the source of the X-ray photons is incorrect. In this case a different model is needed to explain the anti-correlation between the X-ray power law index and the logarithm of the ratio of the X-ray and ultraviolet count rates found by Walter & Courvoisier (1992).

Another explanation for the missing anti-correlation, if the soft excess component is used instead of the UV, could be that the soft excess photons have no contribution to the seed photons of the Comptonisation. In this case the soft excess photons, in contradiction to the UV photons, must not pass the Comptonising electron cloud. Because the temperature of the accretion disk is increasing continuously for decreasing radii, the soft excess photons must be emitted in a region spatial close to the region of the UV emission. It is not reasonable to assume that the UV photons cross a cloud of hot electrons and are Comptonised to higher energies, but the soft excess photons do not cross the same cloud and thus do not contribute to the spectral hard X-ray slope.

The missing relation could be explained, if the soft excess component is not the high energy end of the big blue bump but a different component. The emission region

of the soft excess component could be far away from the accretion disk and therefore outside the Comptonising electron cloud, thus having no contribution to the spectral hard X-ray slope via thermal Comptonisation. A possible emission region of the soft excess component could be related to the base of the jet, for example.

APPENDIX A

RXTE Spectra

In this appendix all RXTE spectra are presented. On each page there are two plots of the same observation. All the different observations are illustrated the same way, the ranges of both axes are identical for all corresponding spectra. The data are fitted using a single power law model including galactic absorption of $N_{\text{H}} = 1.79 \cdot 10^{20} \frac{1}{\text{cm}^2}$ (Dickey & Lockman 1990). The spectral parameters obtained out of the fits are summarised in Tab. 4.1.

In the upper graphs the PCA spectra are shown. The same energy range between 3–21 keV, corresponding to channels 4–46, is used for all PCA spectra.

In the lower charts the combined PCA + HEXTE spectra are presented. The PCA spectra are identically to the upper panel. Due to the different exposure times and dependent on the spectral parameters of the quasar 3C 273 at the time of the observations the energy ranges of the HEXTE spectra vary within the different observations.

Table A.1: The energy ranges of HEXTE spectra.

Date	HEXTE energy range
2000-06-14	11–138 keV
2001-06-13	11– 46 keV
2001-12-16	11– 53 keV
2001-12-21+23	11–121 keV
2002-01-09	11– 69 keV
2003-01-05	11–138 keV
2003-06-16	11–138 keV
2003-07-21	11–138 keV
2004-01-01+02	11– 86 keV

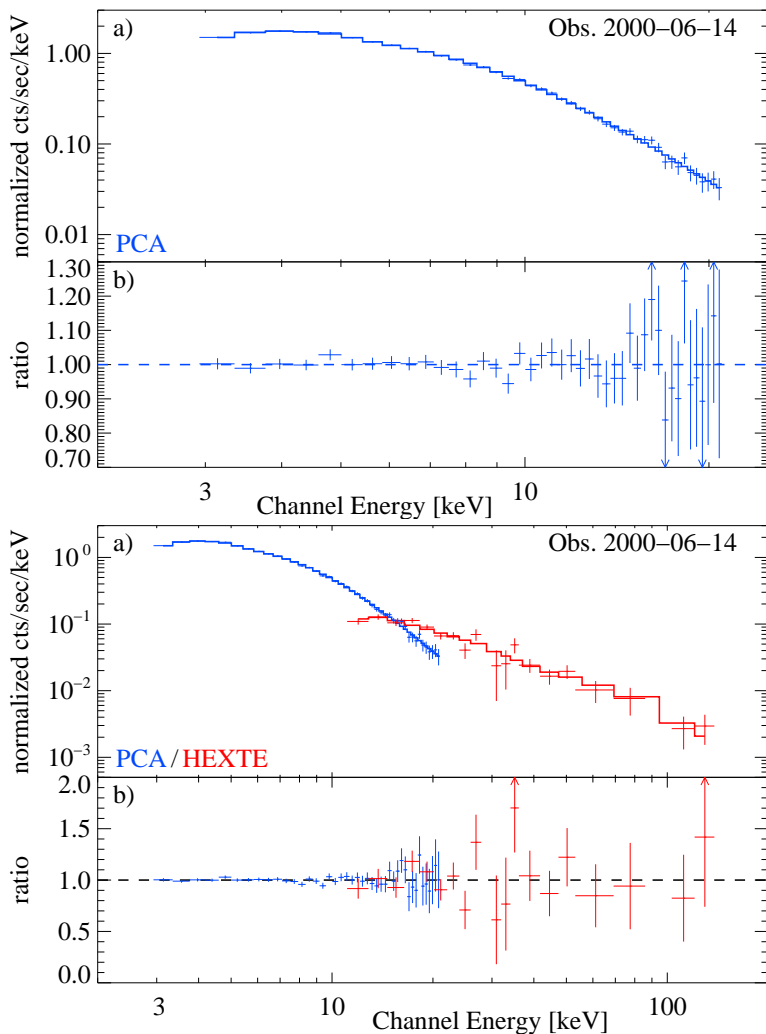


Figure A.1: PCA (top) resp. combined PCA + HEXTE spectrum (bottom) of observation P50184-01-01-00/01/02/03 fitted by a single power law model including galactic absorption. Power law index $\Gamma = 1.61 \pm 0.02$, HEXTE normalisation constant $= 0.77 \pm 0.05$.

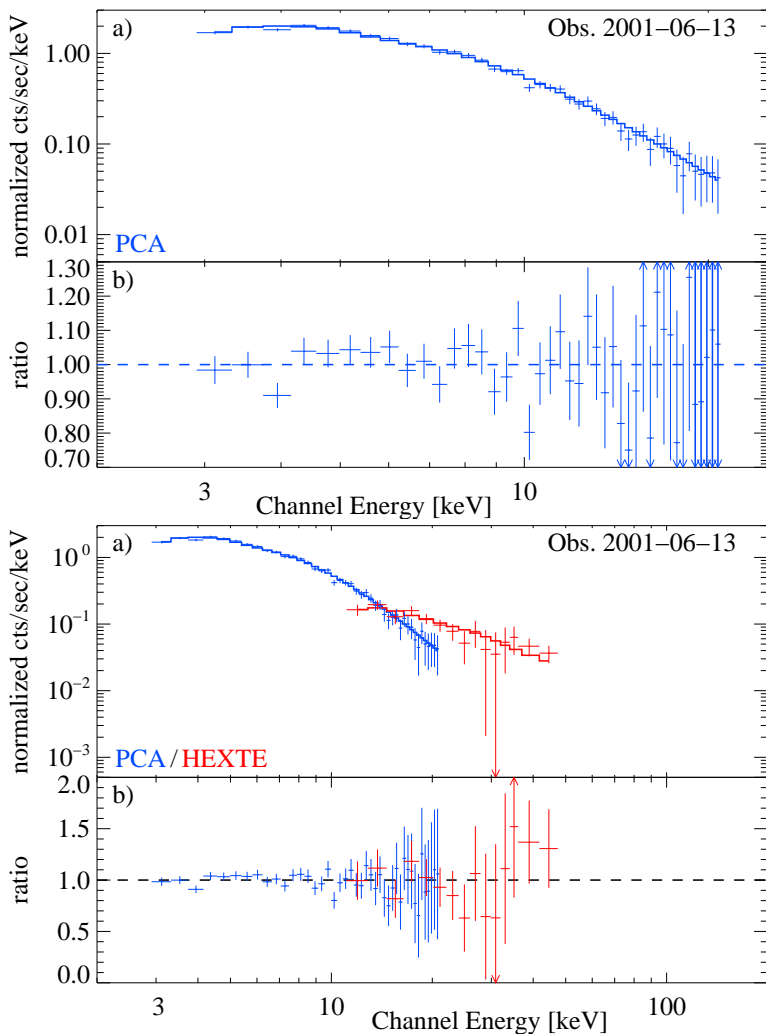


Figure A.2: PCA (top) resp. combined PCA + HEXTE spectrum (bottom) of observation P60144-03-45-00 fitted by a single power law model including galactic absorption. Power law index $\Gamma = 1.60 \pm 0.05$, HEXTE normalisation constant $const = 0.93 \pm 0.11$.

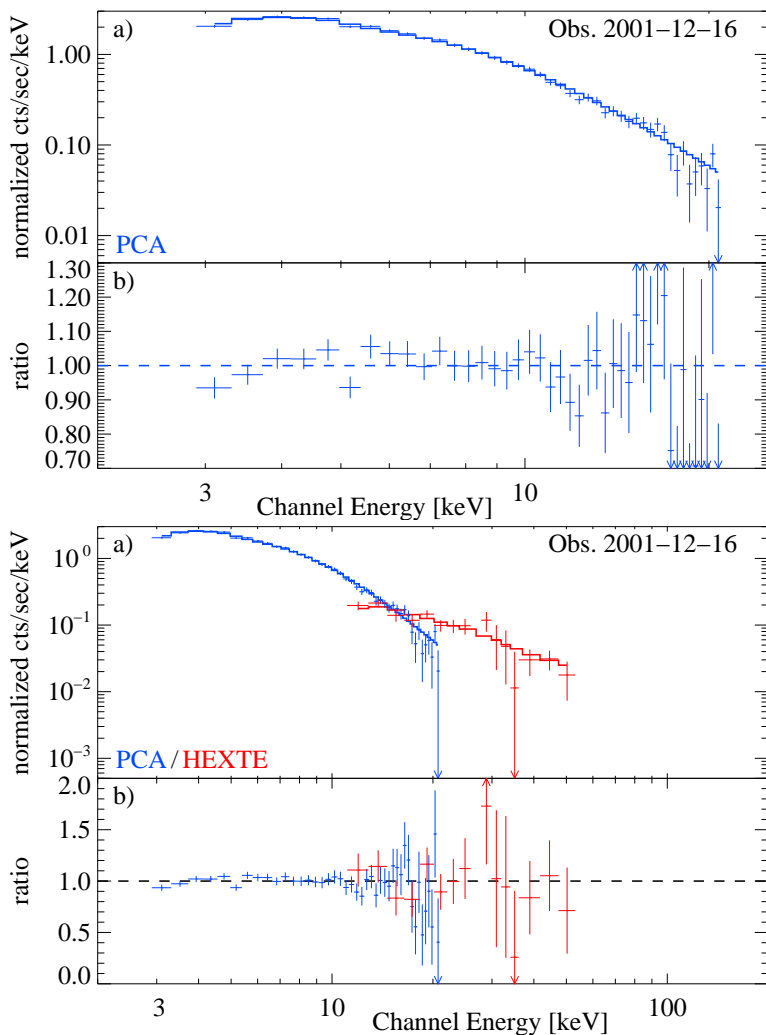


Figure A.3: PCA (top) resp. combined PCA + HEXTE spectrum (bottom) of observation P60144-03-01-10 fitted by a single power law model including galactic absorption. Power law index $\Gamma = 1.61 \pm 0.04$, HEXTE normalisation constant $\text{const} = 0.79 \pm 0.09$.

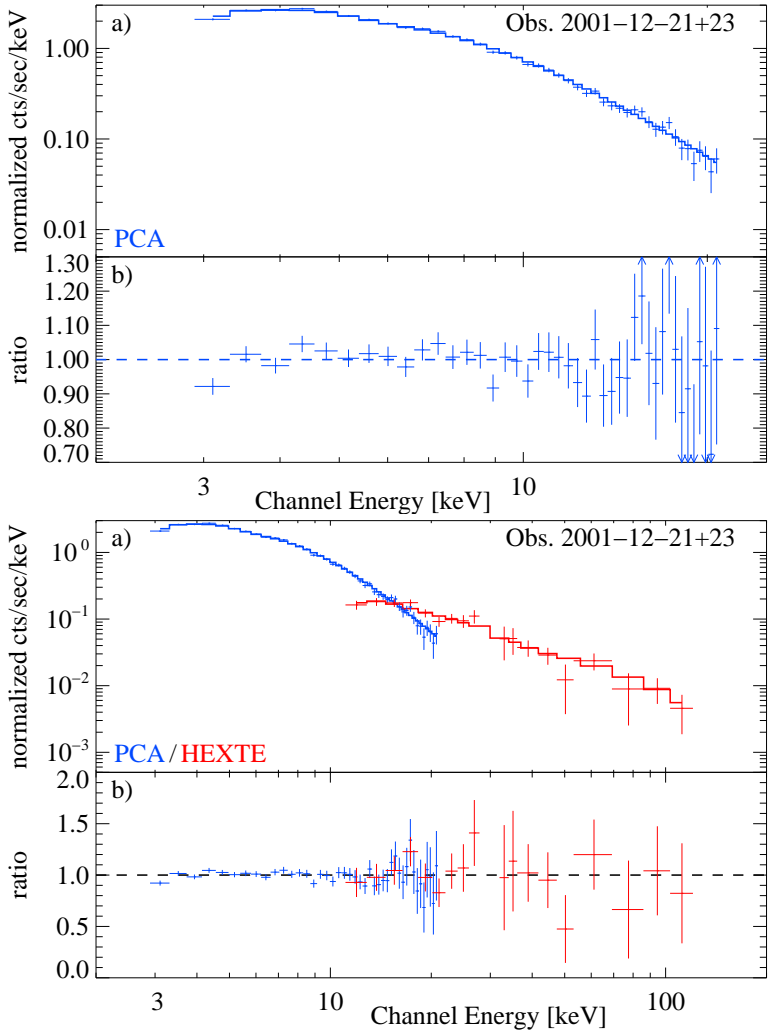


Figure A.4: PCA (top) resp. combined PCA + HEXTE spectrum (bottom) of observation P60144-03-03-10/04-10/04-11 fitted by a single power law model including galactic absorption. Power law index $\Gamma = 1.58 \pm 0.03$, HEXTE normalisation constant $\text{const} = 0.73 \pm 0.06$.

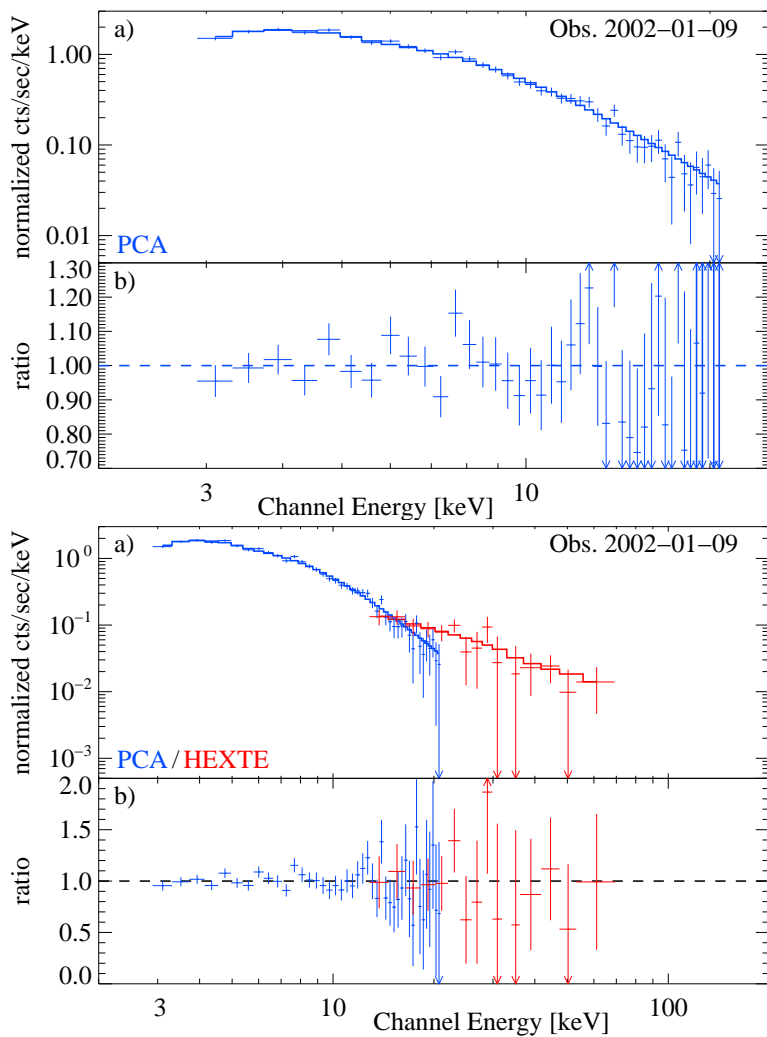


Figure A.5: PCA (top) resp. combined PCA + HEXTE spectrum (bottom) of observation P60144-03-11-10 fitted by a single power law model including galactic absorption. Power law index $\Gamma = 1.59 \pm 0.05$, HEXTE normalisation constant $\text{const} = 0.77 \pm 0.14$.

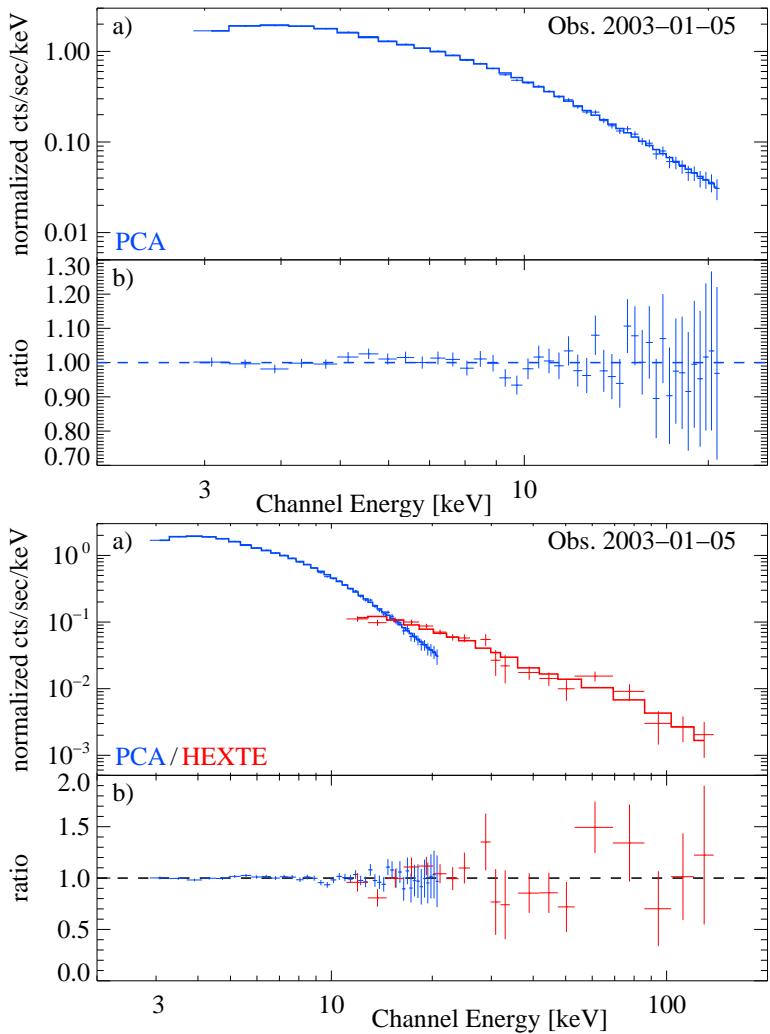


Figure A.6: PCA (top) resp. combined PCA + HEXTE spectrum (bottom) of observation P50184-02-01-00 fitted by a single power law model including galactic absorption. Power law index $\Gamma = 1.73 \pm 0.02$, HEXTE normalisation constant $const = 0.78 \pm 0.04$.

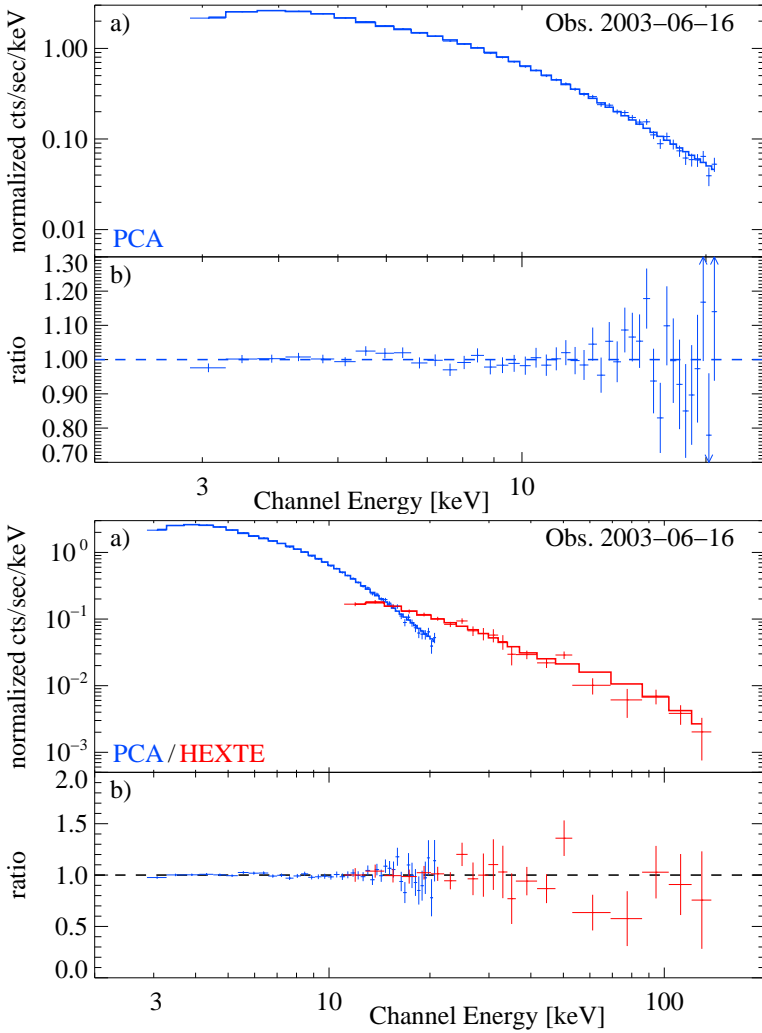


Figure A.7: PCA (top) resp. combined PCA + HEXTE spectrum (bottom) of observation P80165-01-01-00 fitted by a single power law model including galactic absorption. Power law index $\Gamma = 1.68 \pm 0.01$, HEXTE normalisation constant $\text{const} = 0.79 \pm 0.03$.

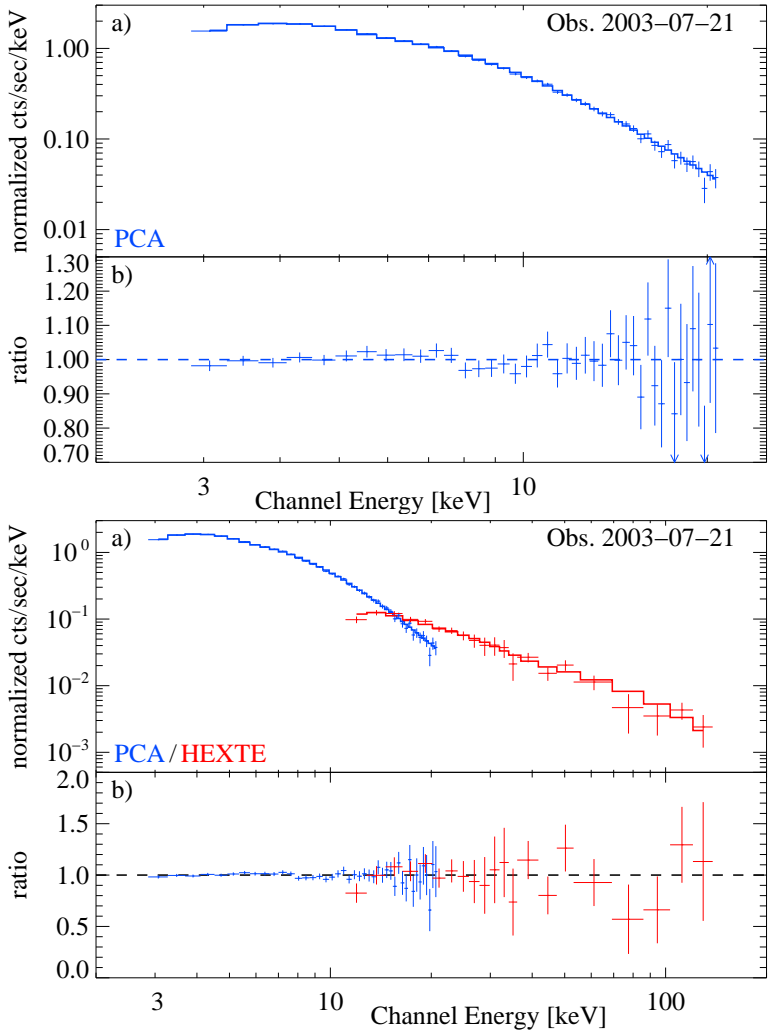


Figure A.8: PCA (top) resp. combined PCA + HEXTE spectrum (bottom) of observation P80165-01-02-00/01 fitted by a single power law model including galactic absorption. Power law index $\Gamma = 1.63 \pm 0.02$, HEXTE normalisation constant $\text{const} = 0.74 \pm 0.04$.

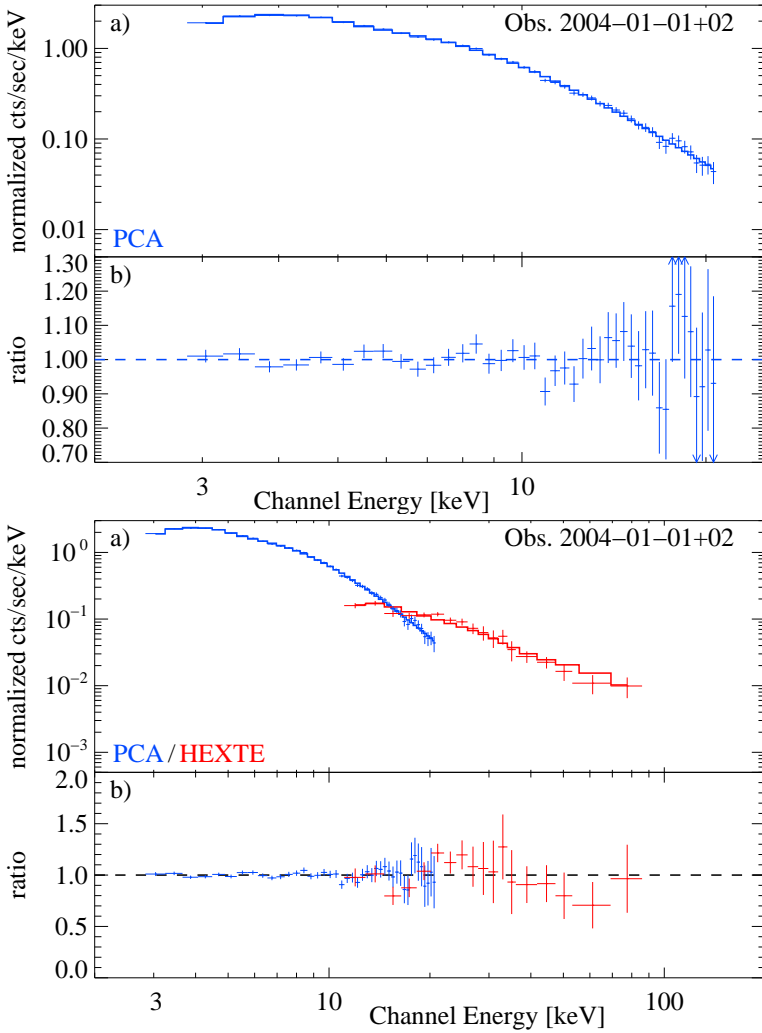


Figure A.9: PCA (top) resp. combined PCA + HEXTE spectrum (bottom) of observation P80165-01-03-00 fitted by a single power law model including galactic absorption. Power law index $\Gamma = 1.69 \pm 0.02$, HEXTE normalisation constant $\text{const} = 0.96 \pm 0.05$.

APPENDIX B

XMM spectra

A set of four XMM EPIC spectra per observation, each on two pages, is summarised in this appendix. Similar to the RXTE appendix the layout of the specific plots is the same for all observations.

The first pages of each observation present the PN/MOS2 spectral fits of the high energetic power law component, equivalent to the RXTE fits. The energy range is 2.5–10.0 keV for both PN and MOS2. The panels showing the normalised count spectra have identical ranges, but the ranges of the ratio panels are different for PN (0.7–1.3) and MOS2 (0.5–1.5). The detailed results are summarised in Tab. 4.2.

The second pages contain the PN plots of the two different models used for the characterisation of the soft excess at energies lower than 2 keV. The upper graphs show the double power law model, the lower one the combined disk blackbody and power law model, both including galactic absorption of $N_{\text{H}} = 1.79 \cdot 10^{20} \frac{1}{\text{cm}^2}$ (Dickey & Lockman 1990). See Tab. 4.4 for the resulting fit parameters.

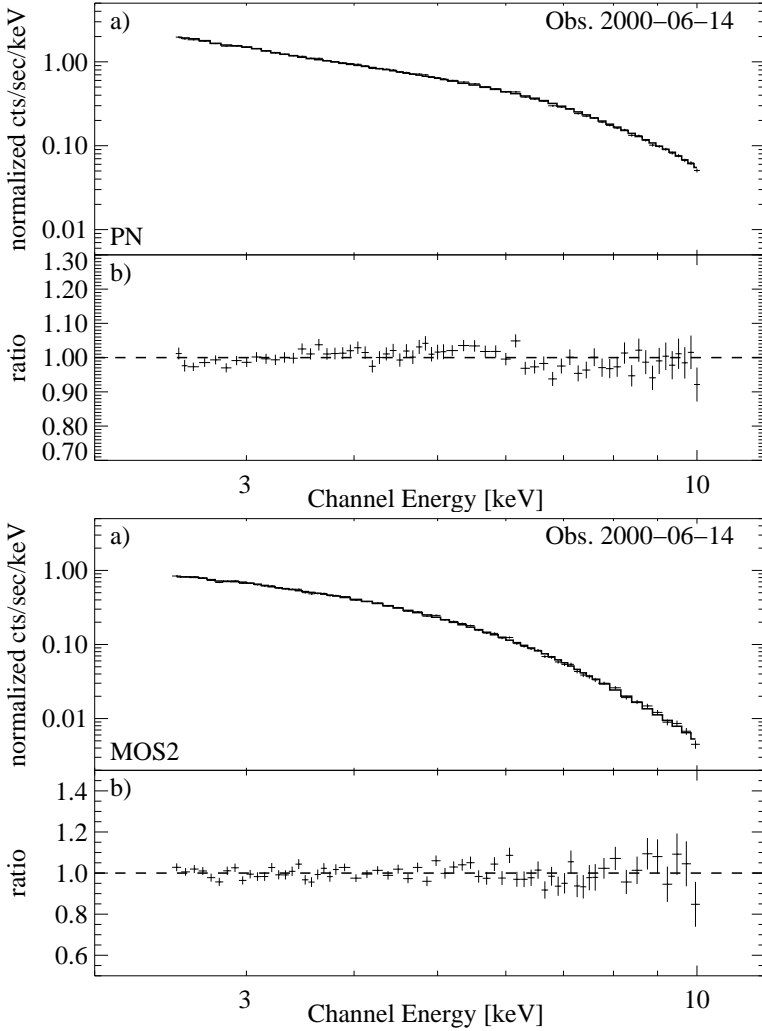


Figure B.1: PN (top) resp. MOS2 spectrum (bottom) of observation 0126700301 fitted by a single power law model including galactic absorption. Power law indices $\Gamma_{\text{PN}} = 1.66 \pm 0.01$; $\Gamma_{\text{MOS2}} = 1.64 \pm 0.02$.

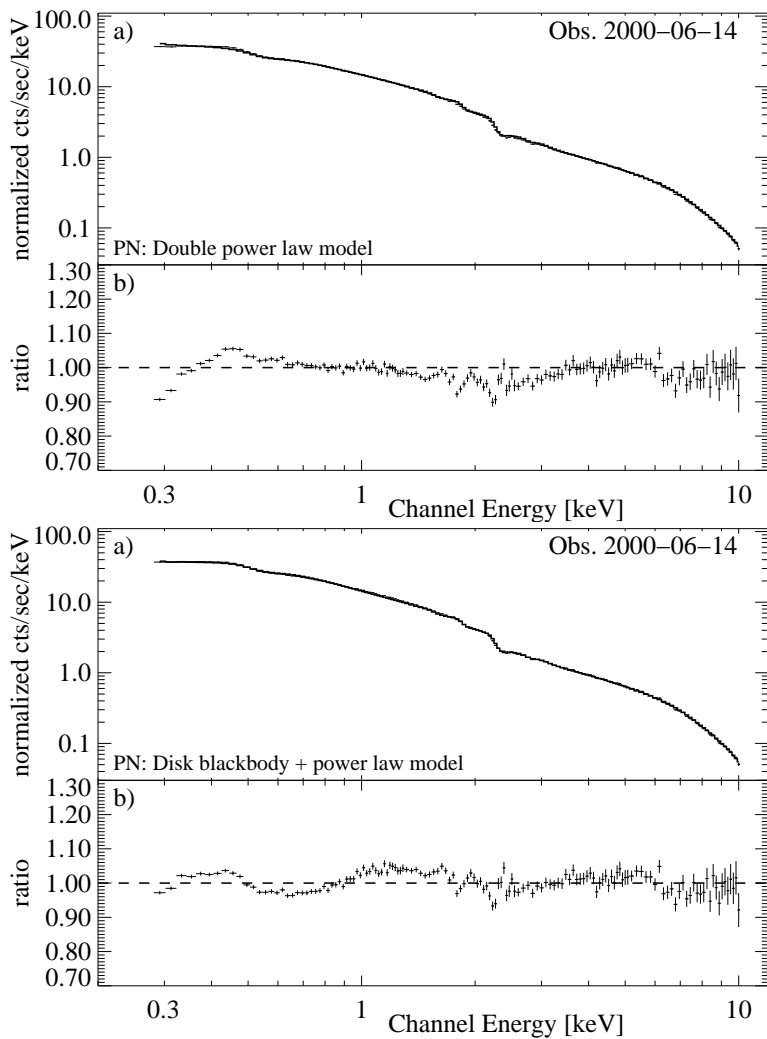


Figure B.2: PN soft excess characterisations of observation 0126700301. Top: double power law model; bottom: combined disk blackbody + power law model.

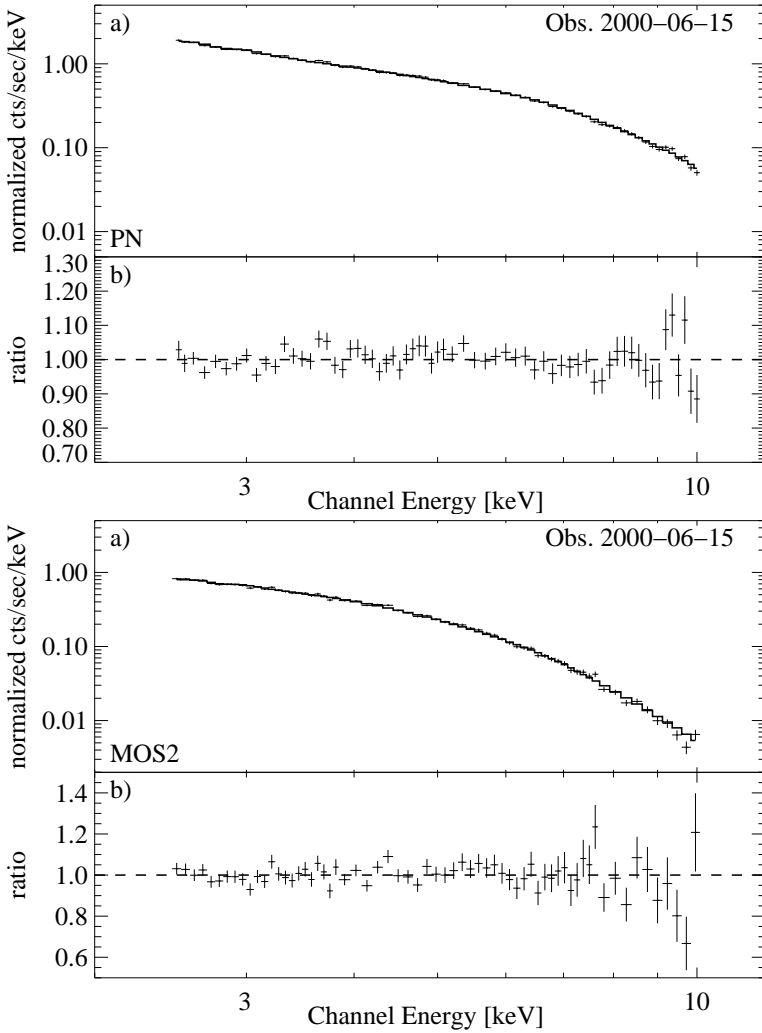


Figure B.3: PN (top) resp. MOS2 spectrum (bottom) of observation 0126700601 fitted by a single power law model including galactic absorption. Power law indices $\Gamma_{\text{PN}} = 1.60 \pm 0.02$; $\Gamma_{\text{MOS2}} = 1.61 \pm 0.03$.

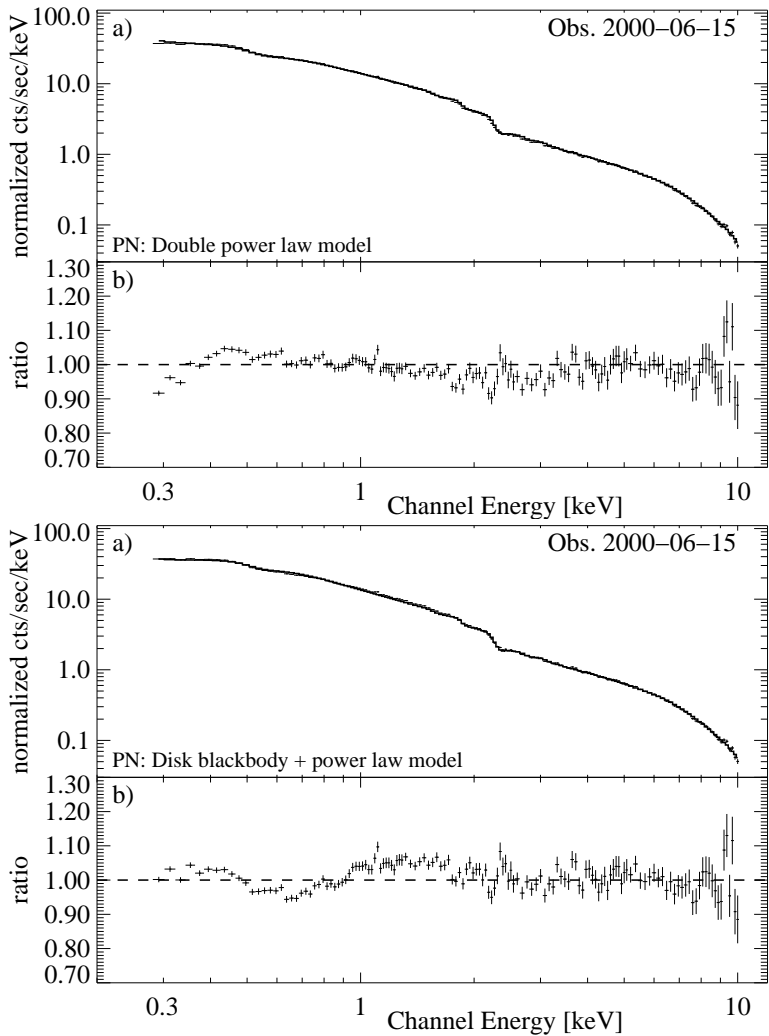


Figure B.4: PN soft excess characterisations of observation 0126700601. Top: double power law model; bottom: combined disk blackbody + power law model.

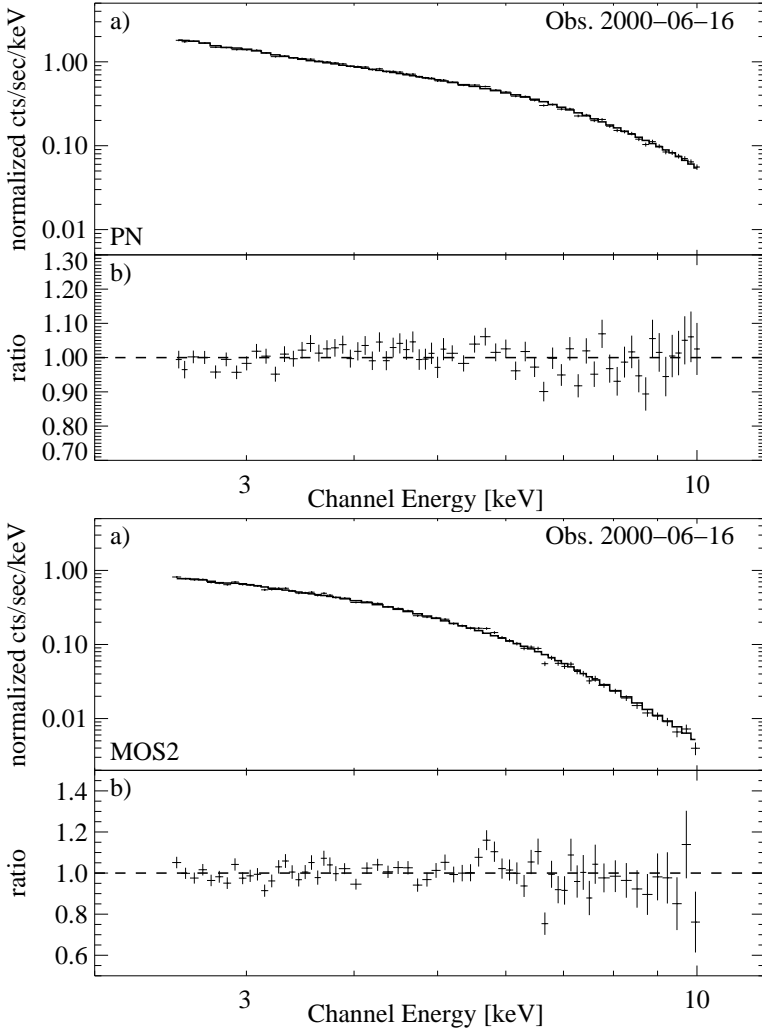


Figure B.5: PN (top) resp. MOS2 spectrum (bottom) of observation 0126700701 fitted by a single power law model including galactic absorption. Power law indices $\Gamma_{\text{PN}} = 1.62 \pm 0.02$; $\Gamma_{\text{MOS2}} = 1.61 \pm 0.03$.

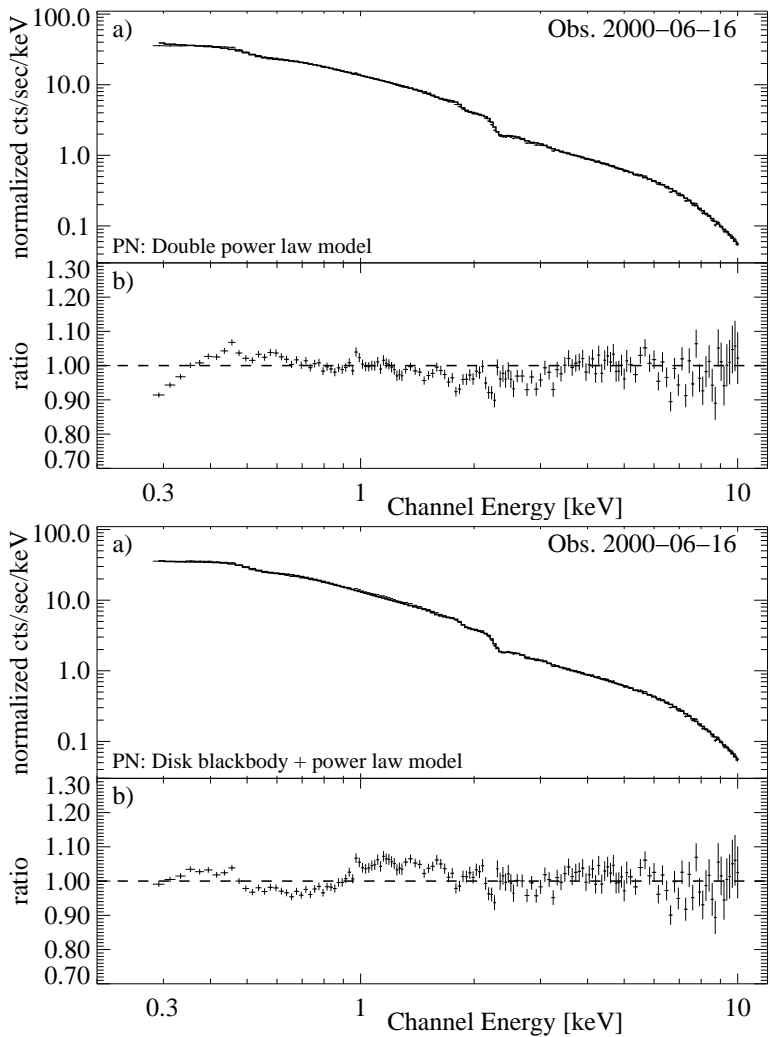


Figure B.6: PN soft excess characterisations of observation 0126700701. Top: double power law model; bottom: combined disk blackbody + power law model.

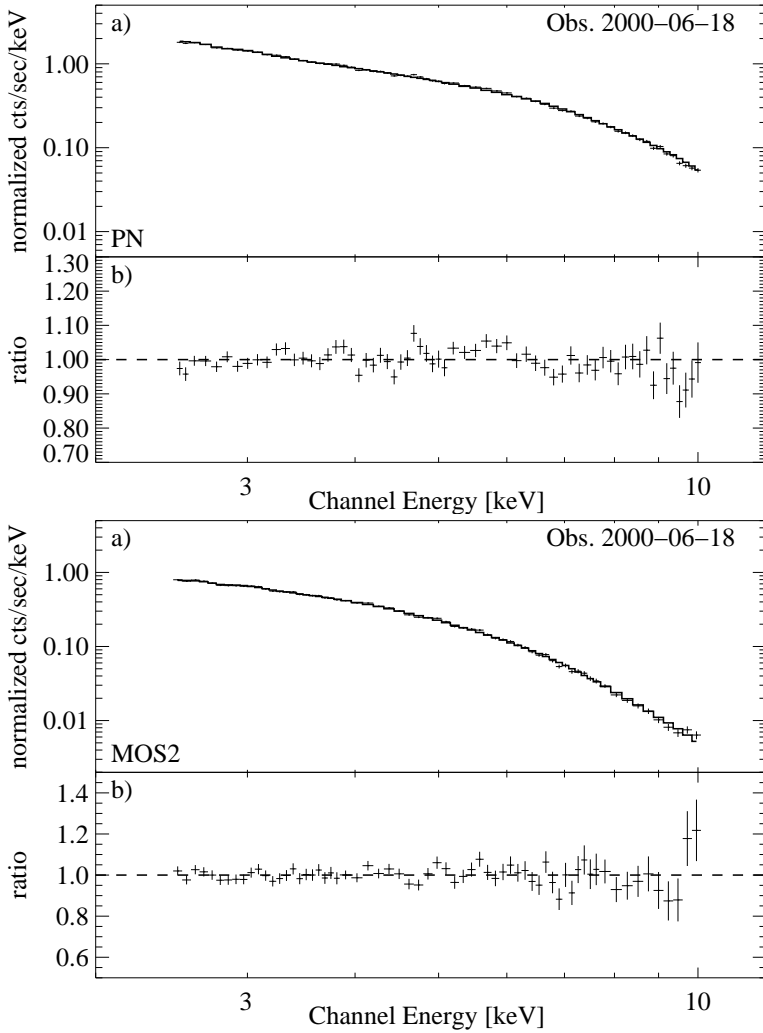


Figure B.7: PN (top) resp. MOS2 spectrum (bottom) of observation 0126700801 fitted by a single power law model including galactic absorption. Power law indices $\Gamma_{\text{PN}} = 1.63 \pm 0.01$; $\Gamma_{\text{MOS2}} = 1.62 \pm 0.02$.

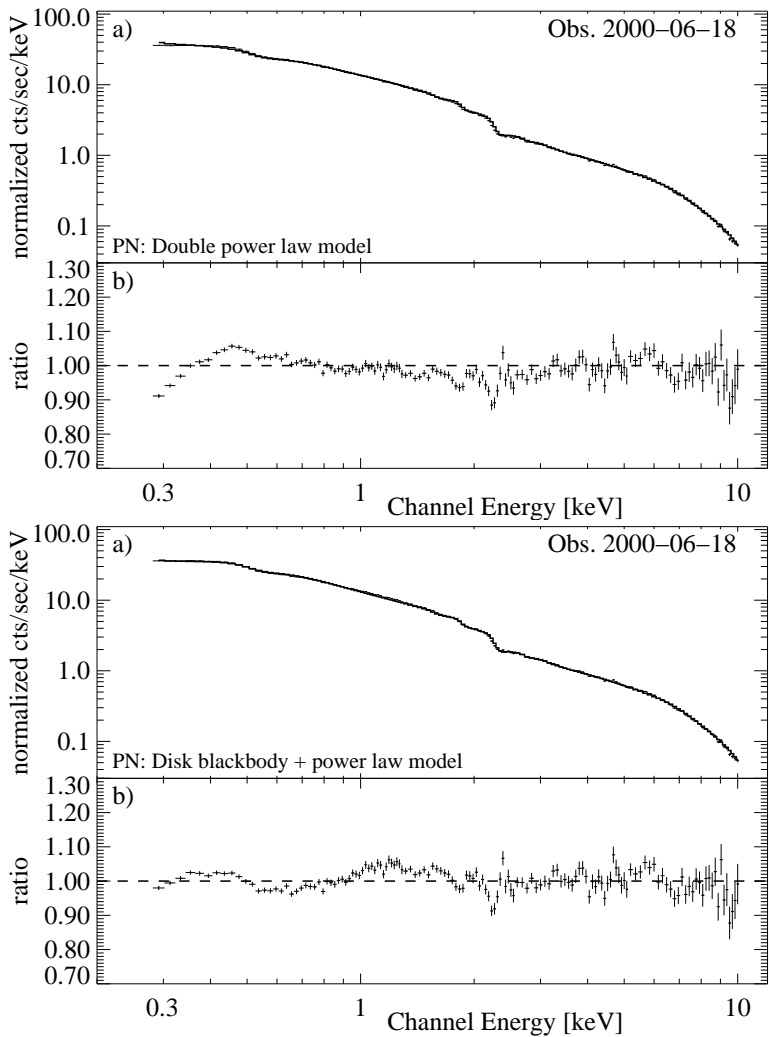


Figure B.8: PN soft excess characterisations of observation 0126700801. Top: double power law model; bottom: combined disk blackbody + power law model.

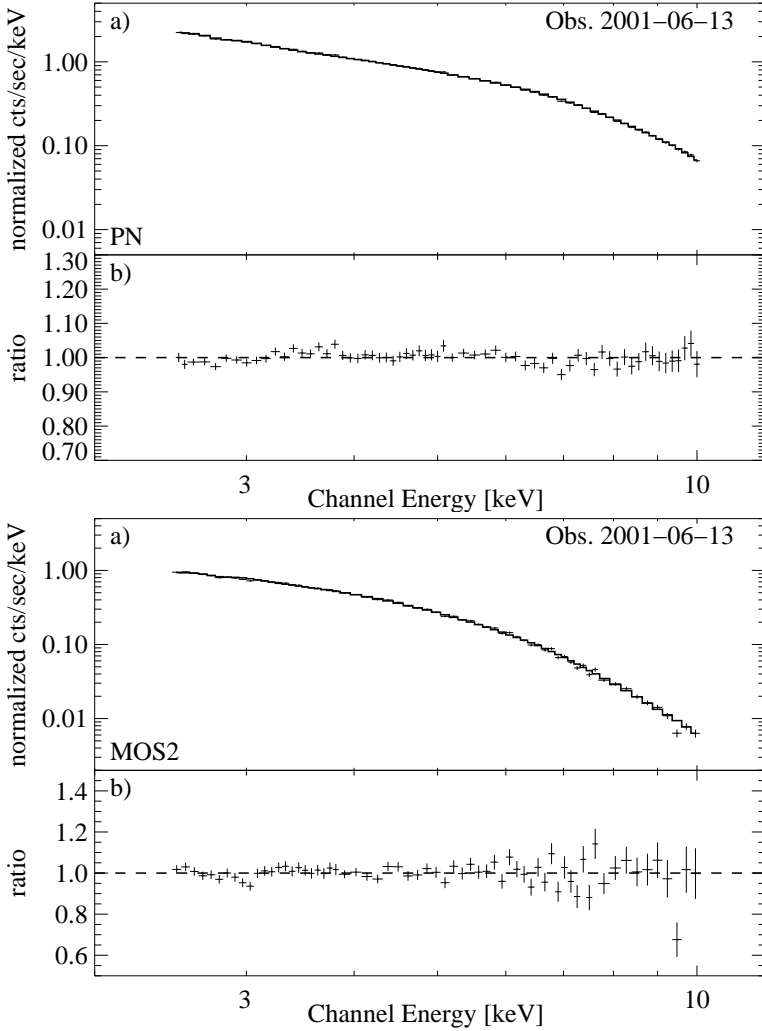


Figure B.9: PN (top) resp. MOS2 spectrum (bottom) of observation 0136550101 fitted by a single power law model including galactic absorption. Power law indices $\Gamma_{\text{PN}} = 1.61 \pm 0.01$; $\Gamma_{\text{MOS2}} = 1.61 \pm 0.02$.

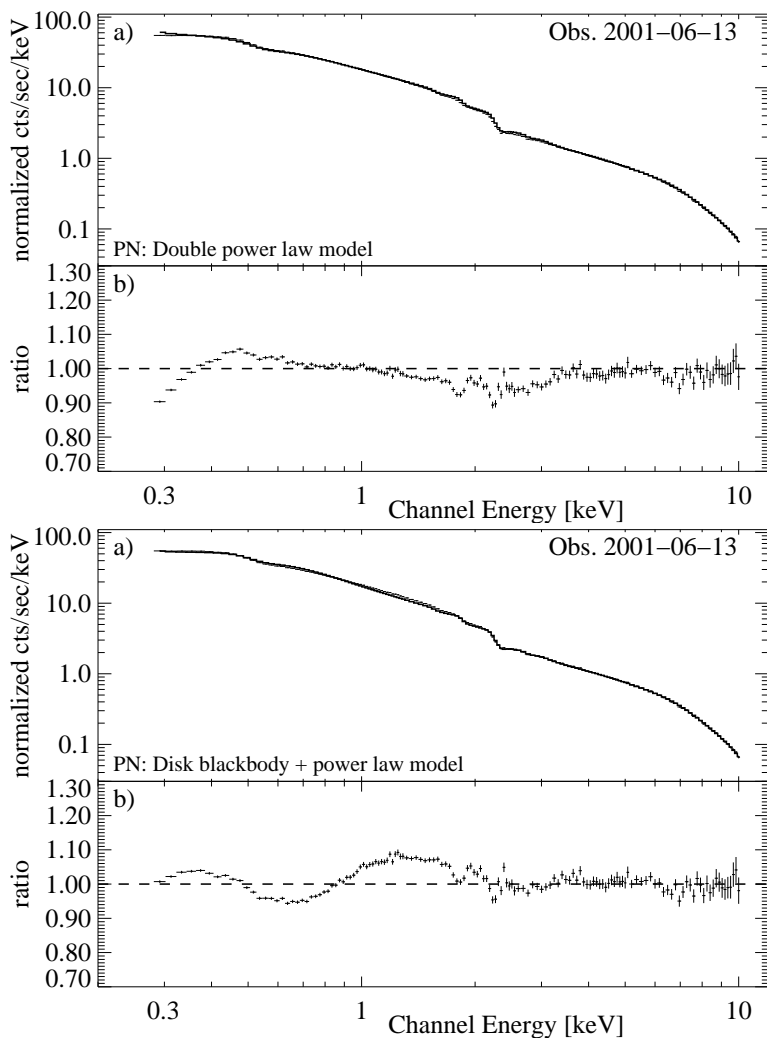


Figure B.10: PN soft excess characterisations of observation 0136550101. Top: double power law model; bottom: combined disk blackbody + power law model.

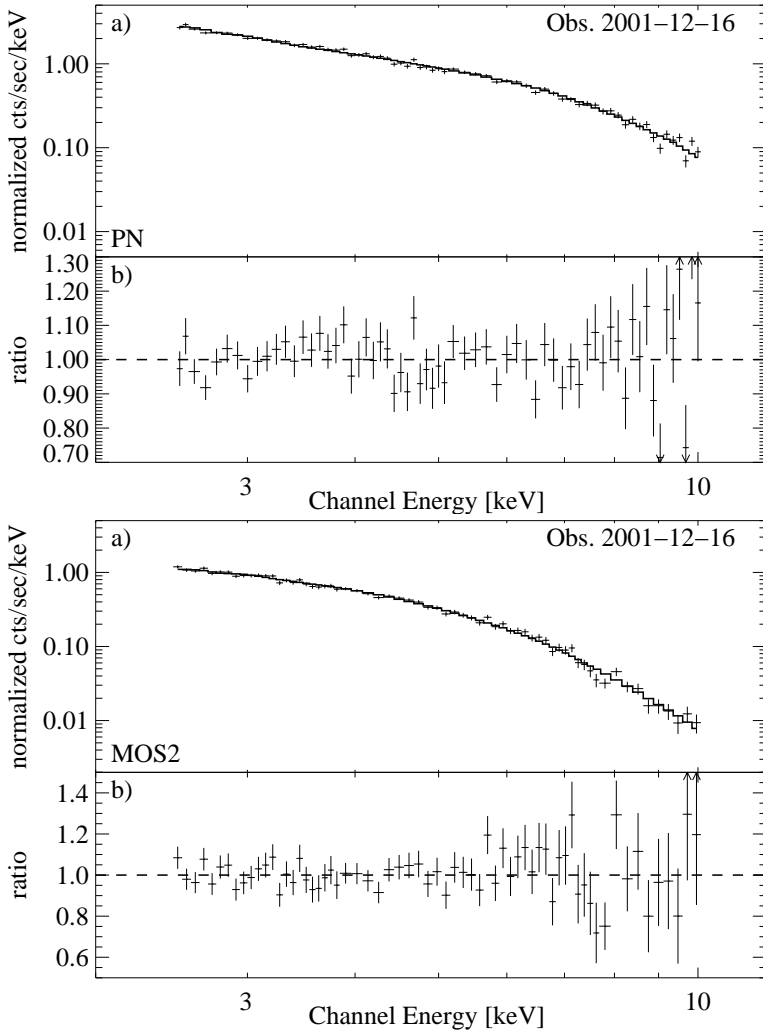


Figure B.11: PN (top) resp. MOS2 spectrum (bottom) of observation 0112770101 fitted by a single power law model including galactic absorption. Power law indices $\Gamma_{\text{PN}} = 1.67 \pm 0.04$; $\Gamma_{\text{MOS2}} = 1.57 \pm 0.05$.

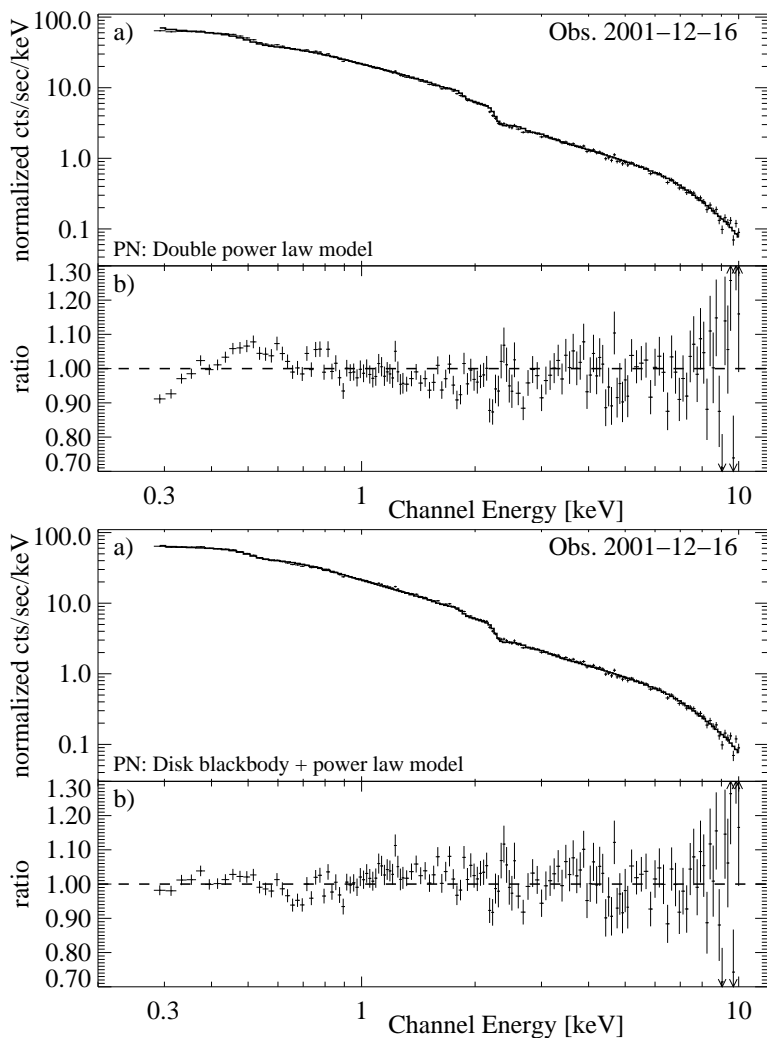


Figure B.12: PN soft excess characterisations of observation 0112770101. Top: double power law model; bottom: combined disk blackbody + power law model.

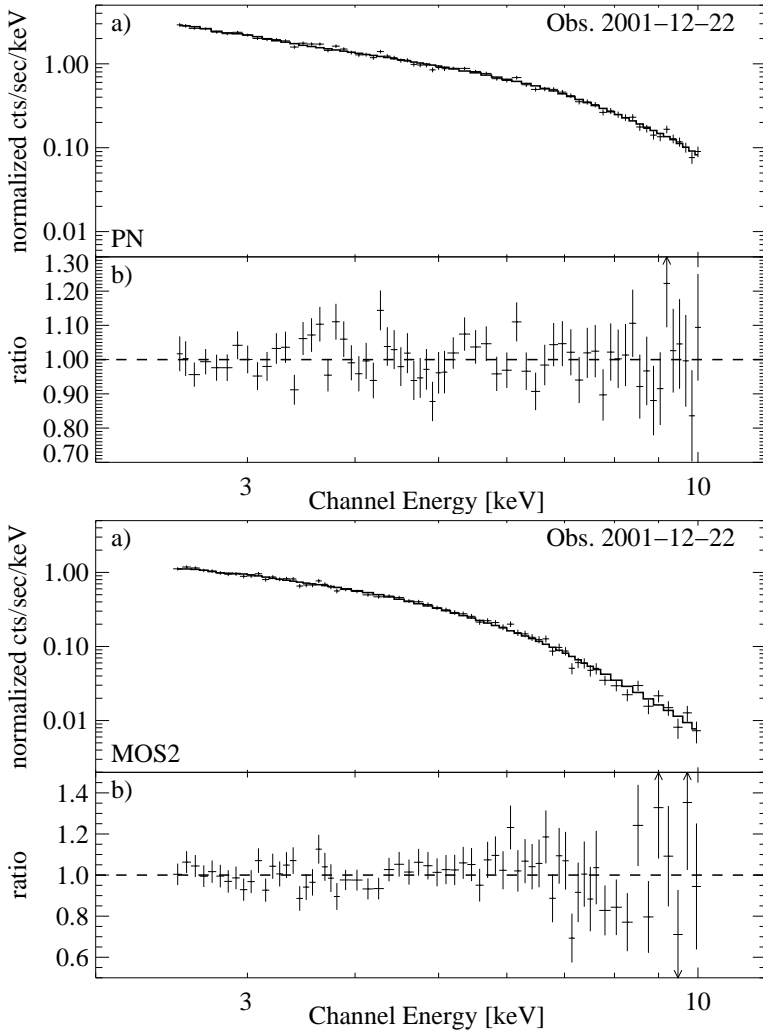


Figure B.13: PN (top) resp. MOS2 spectrum (bottom) of observation 0112770201 fitted by a single power law model including galactic absorption. Power law indices $\Gamma_{\text{PN}} = 1.64 \pm 0.03$; $\Gamma_{\text{MOS2}} = 1.59 \pm 0.05$.

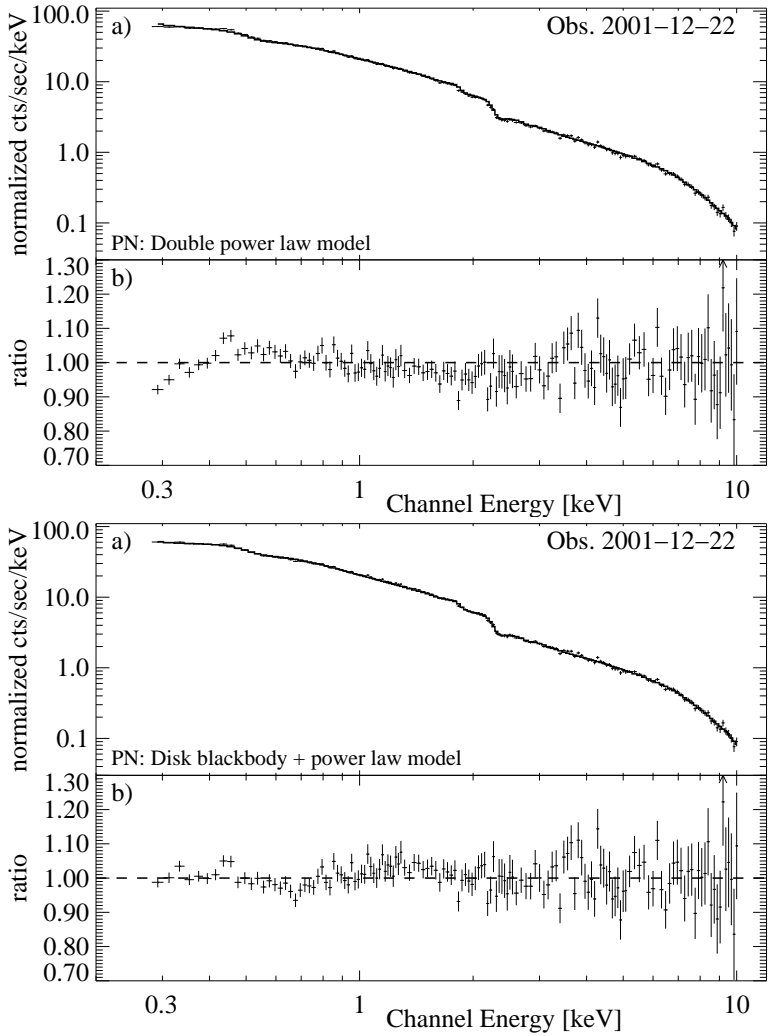


Figure B.14: PN soft excess characterisations of observation 0112770201. Top: double power law model; bottom: combined disk blackbody + power law model.

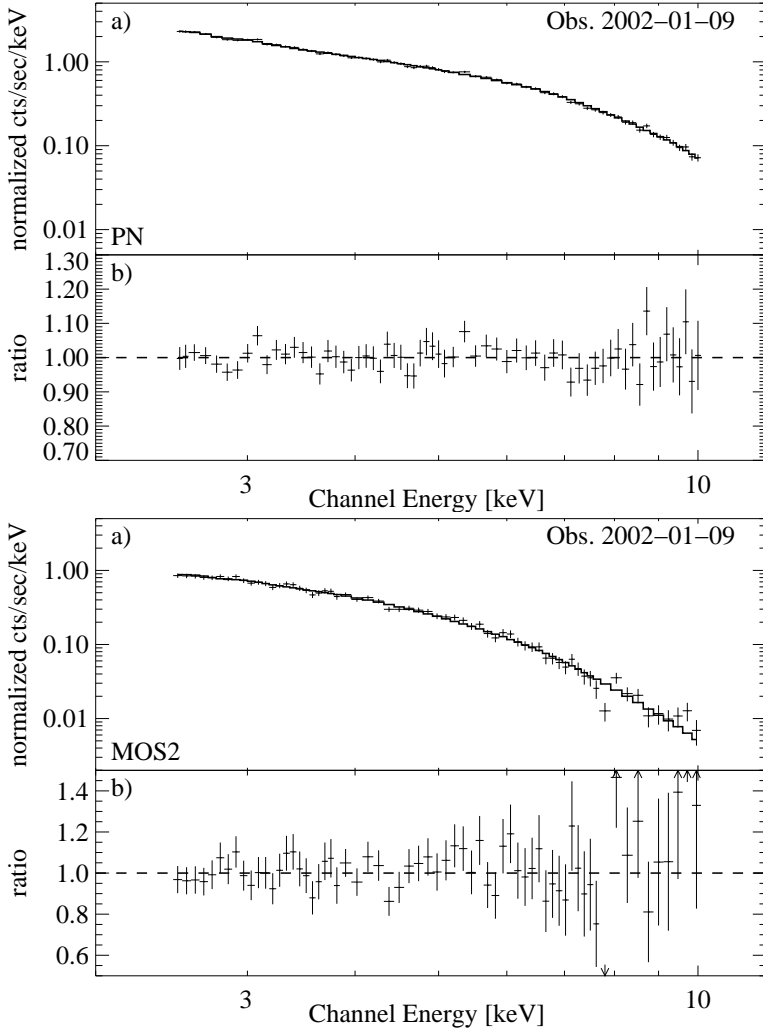


Figure B.15: PN (top) resp. MOS2 spectrum (bottom) of observation 0137551001 fitted by a single power law model including galactic absorption. Power law indices $\Gamma_{\text{PN}} = 1.71 \pm 0.02$; $\Gamma_{\text{MOS2}} = 1.71 \pm 0.06$.

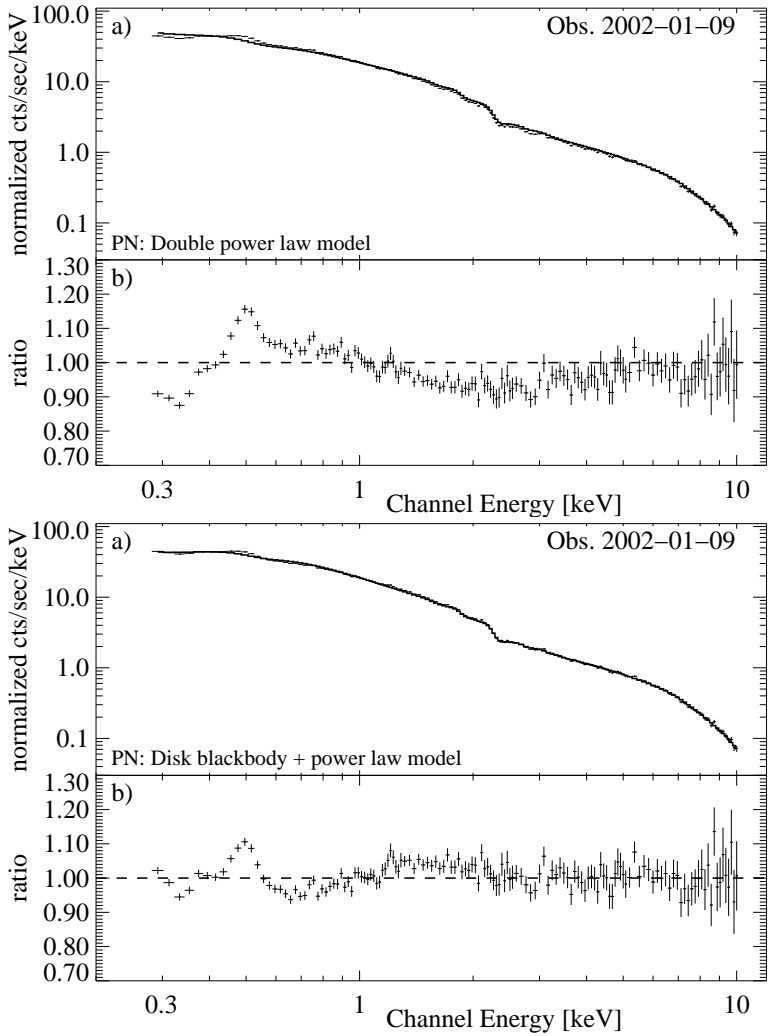


Figure B.16: PN soft excess characterisations of observation 0137551001. Top: double power law model; bottom: combined disk blackbody + power law model.

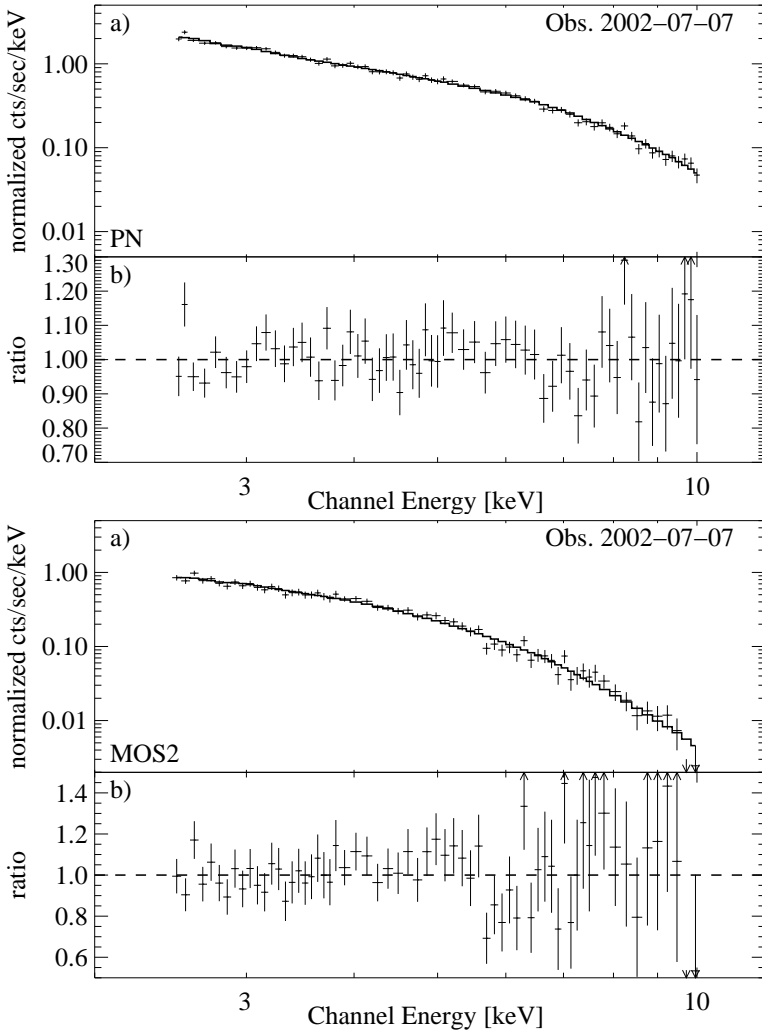


Figure B.17: PN (top) resp. MOS2 spectrum (bottom) of observation 0112770601 fitted by a single power law model including galactic absorption. Power law indices $\Gamma_{\text{PN}} = 1.77 \pm 0.04$; $\Gamma_{\text{MOS2}} = 1.78 \pm 0.08$.

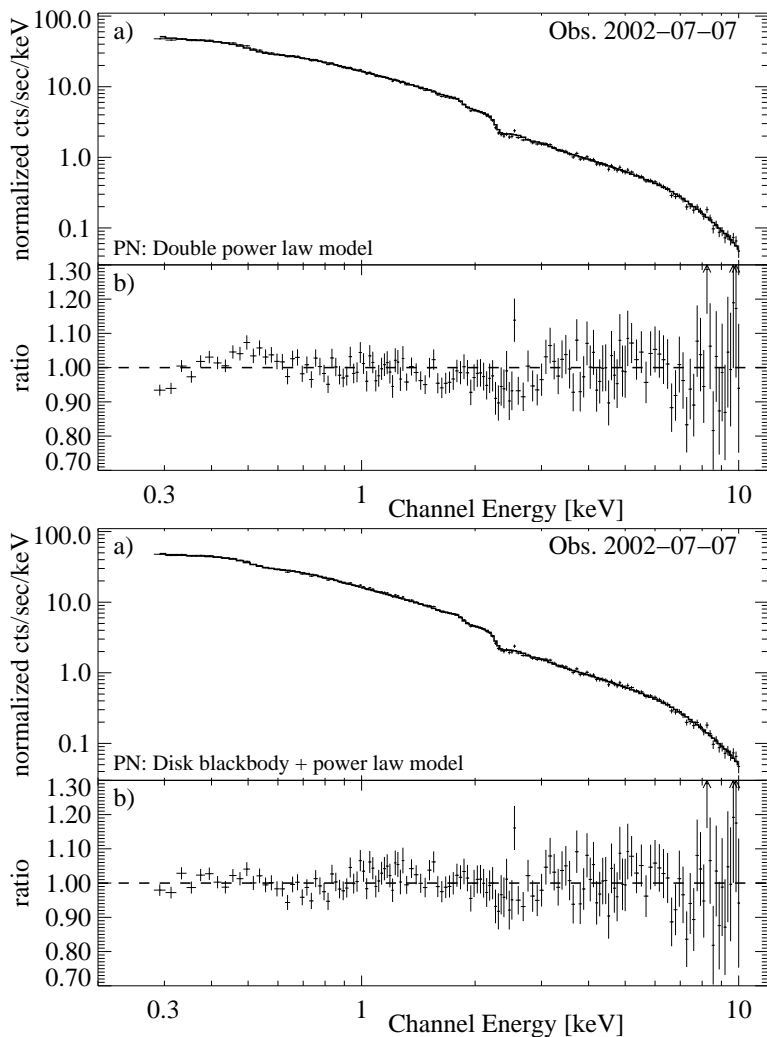


Figure B.18: PN soft excess characterisations of observation 0112770601. Top: double power law model; bottom: combined disk blackbody + power law model.

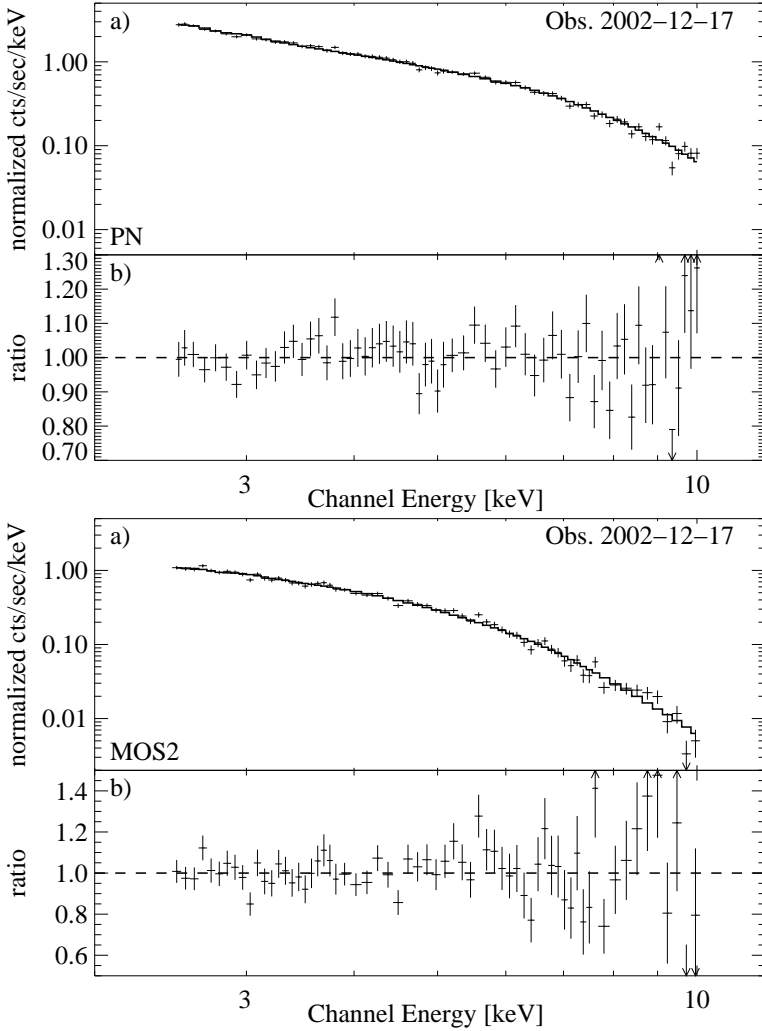


Figure B.19: PN (top) resp. MOS2 spectrum (bottom) of observation 0112770801 fitted by a single power law model including galactic absorption. Power law indices $\Gamma_{\text{PN}} = 1.79 \pm 0.04$; $\Gamma_{\text{MOS2}} = 1.72 \pm 0.05$.

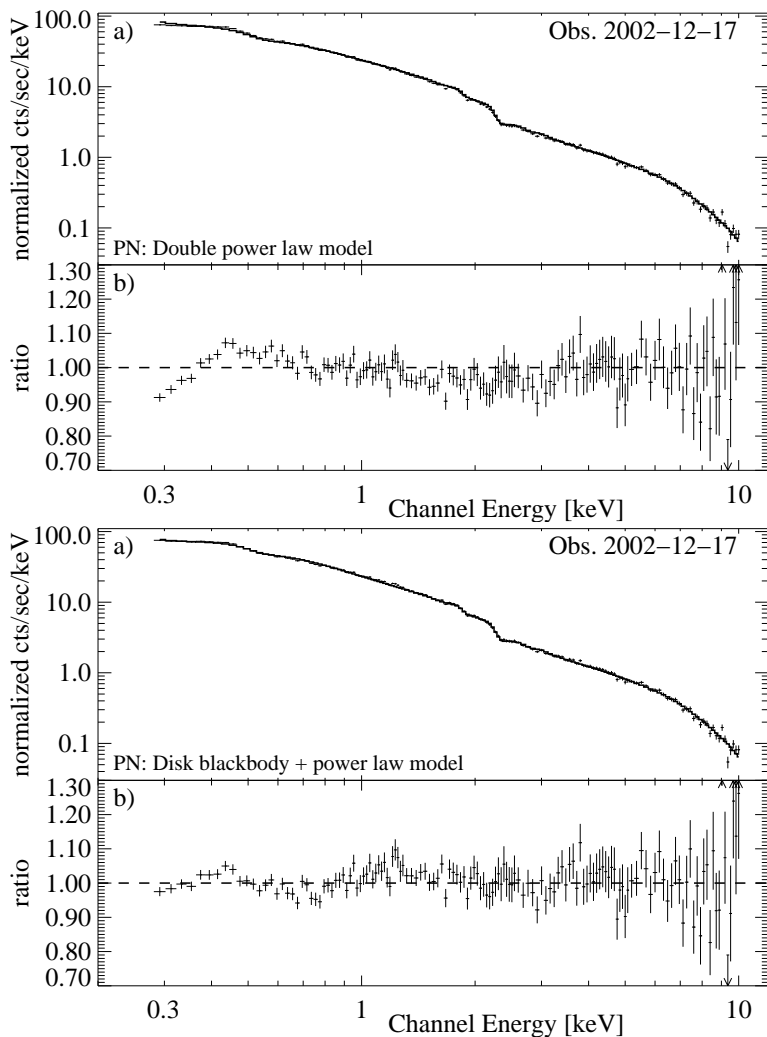


Figure B.20: PN soft excess characterisations of observation 0112770801. Top: double power law model; bottom: combined disk blackbody + power law model.

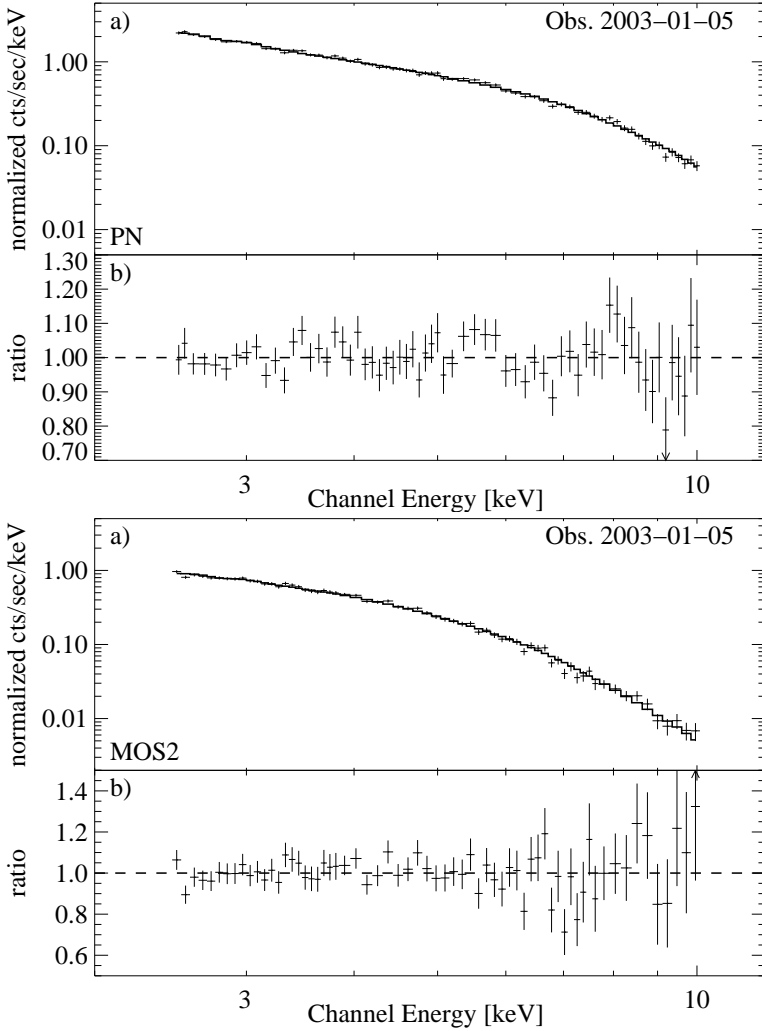


Figure B.21: PN (top) resp. MOS2 spectrum (bottom) of observation 0136550501 fitted by a single power law model including galactic absorption. Power law indices $\Gamma_{\text{PN}} = 1.74 \pm 0.03$; $\Gamma_{\text{MOS2}} = 1.74 \pm 0.05$.

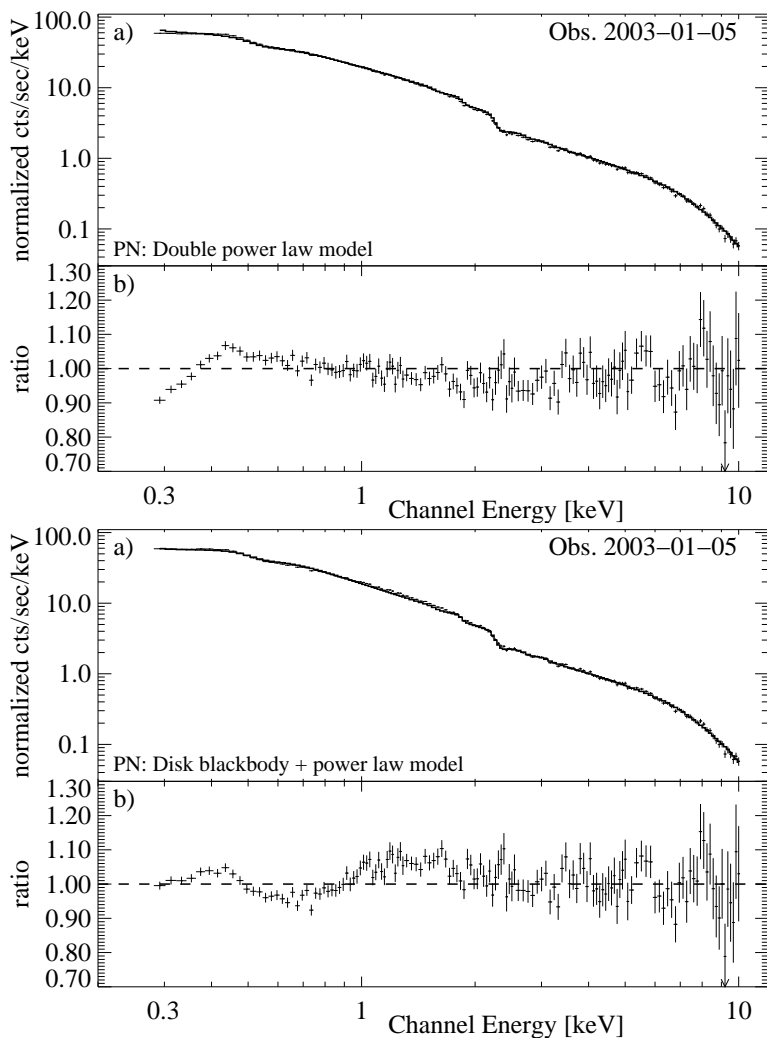


Figure B.22: PN soft excess characterisations of observation 0136550501. Top: double power law model; bottom: combined disk blackbody + power law model.

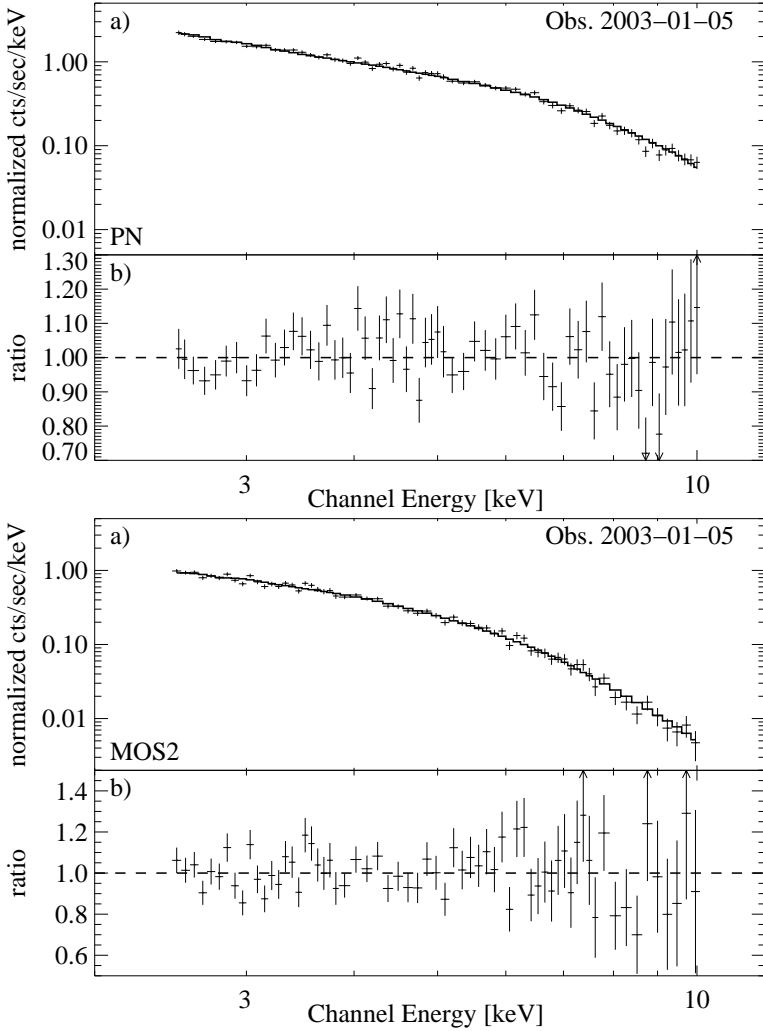


Figure B.23: PN (top) resp. MOS2 spectrum (bottom) of observation 0112770701 fitted by a single power law model including galactic absorption. Power law indices $\Gamma_{\text{PN}} = 1.73 \pm 0.04$; $\Gamma_{\text{MOS2}} = 1.75 \pm 0.06$.

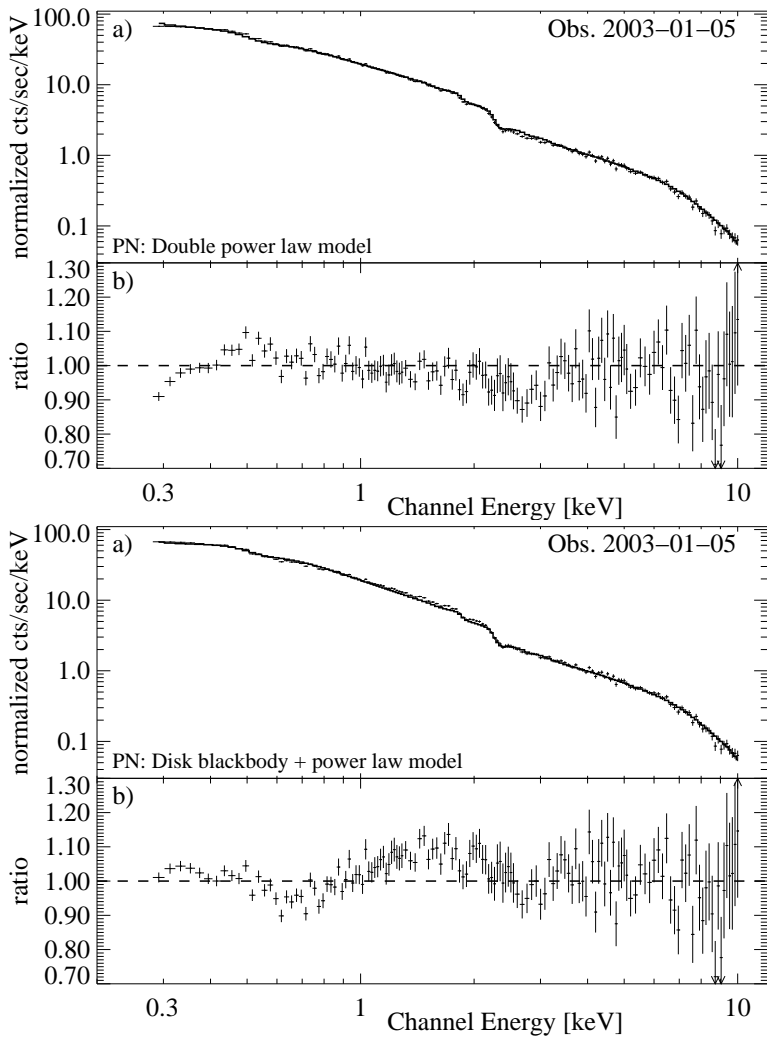


Figure B.24: PN soft excess characterisations of observation 0112770701. Top: double power law model; bottom: combined disk blackbody + power law model.

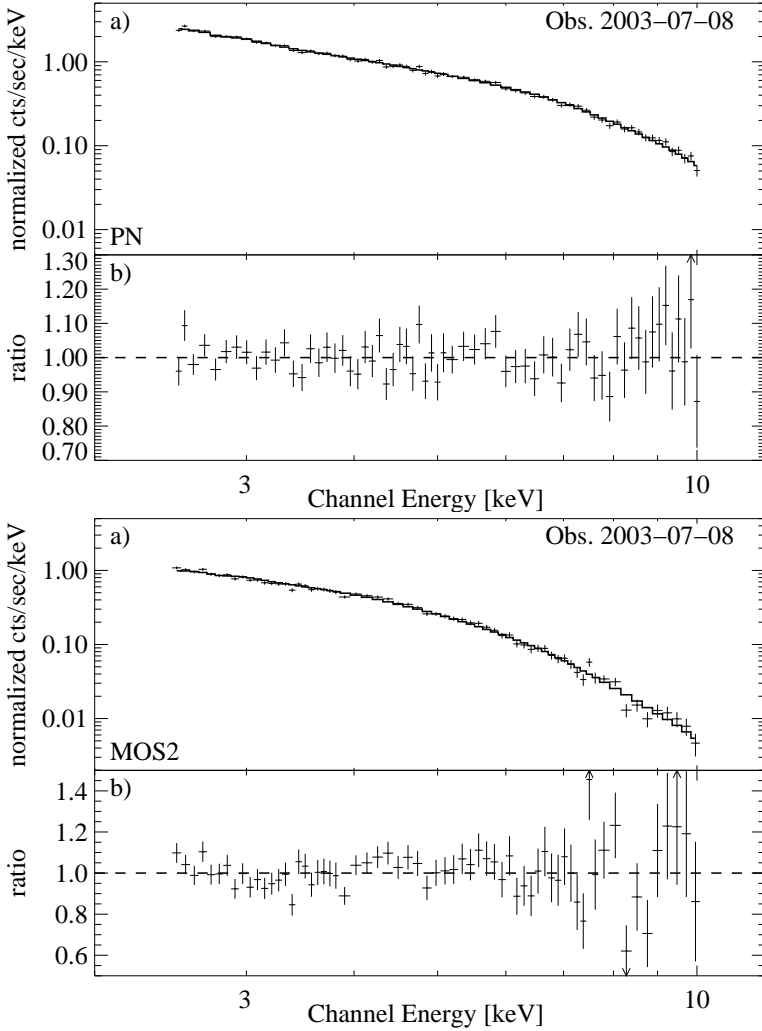


Figure B.25: PN (top) resp. MOS2 spectrum (bottom) of observation 0112770501 fitted by a single power law model including galactic absorption. Power law indices $\Gamma_{\text{PN}} = 1.78 \pm 0.03$; $\Gamma_{\text{MOS2}} = 1.76 \pm 0.05$.

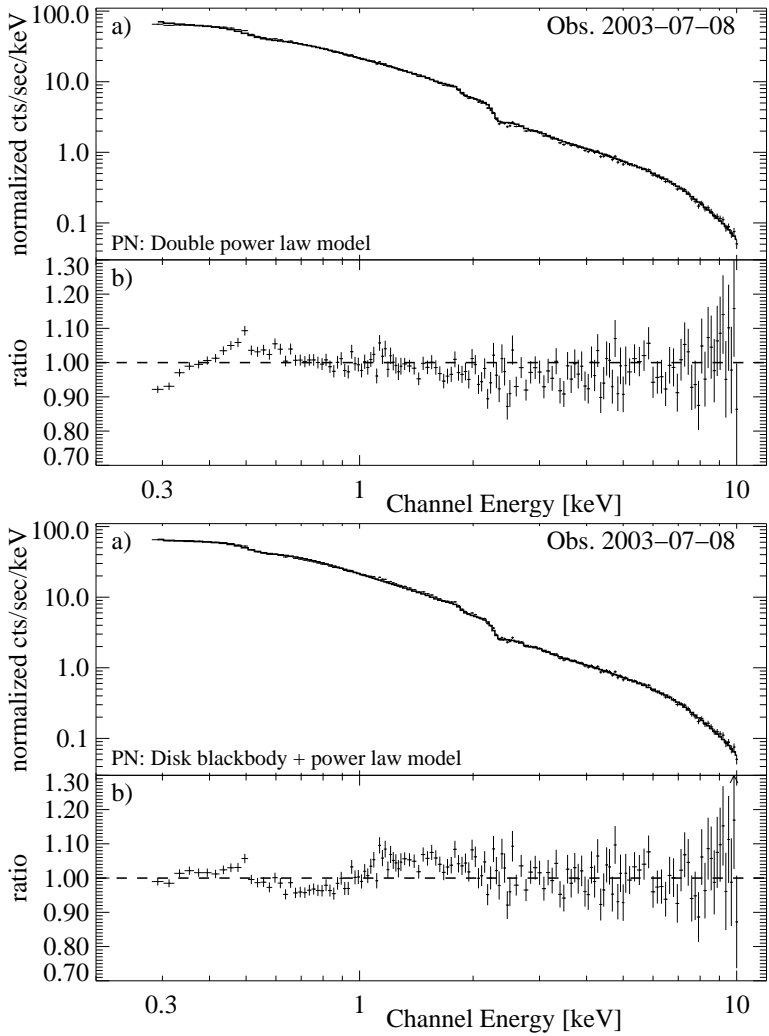


Figure B.26: PN soft excess characterisations of observation 0112770501. Top: double power law model; bottom: combined disk blackbody + power law model.

Bibliography

- Abraham, Z., Carrara, E. A., Zensus, J. A., & Unwin, S. C. 1996, *Astron. Astrophys. Suppl. Ser.*, 115, 543
- Abraham, Z. & Romero, G. E. 1999, *Astron. Astrophys.*, 344, 61
- Angione, R. J. & Smith, H. J. 1985, *Astron. J.*, 90, 2474
- Asada, K., Inoue, M., Uchida, Y., et al. 2002, *Publ. Astron. Soc. Jpn.*, 54, L39
- Bahcall, J. N., Kirhakos, S., Schneider, D. P., et al. 1995, *Astrophys. J.*, 452, L91
- Benlloch-Garçia, S. 2003, PhD thesis, IAA, Universität Tübingen
- Bowyer, C. S., Lampton, M., Mack, J., & de Mendonca, F. 1970, *Astrophys. J., Lett.*, 161, L1
- Bühler, P., Courvoisier, T. J.-L., & Staubert, R. 1994, *Astron. Astrophys.*, 287, 433
- Cappi, M., Matsuoka, M., Otani, C., & Leighly, K. M. 1998, *Publ. Astron. Soc. Jpn.*, 50, 213
- Collmar, W. 2001, in *Exploring the Gamma-Ray Universe*, ed. B. Batrick, A. Gimenez, V. Reglero, & C. Winkler, Vol. ESA SP-459, Noordwijk: ESA Publications Division, 241–248
- Collmar, W., Benlloch, S., Grove, J. E., et al. 2000, in *The Fifth Compton Symposium*, ed. M. L. McConnell & J. M. Ryan, Vol. 510, AIP Conference Proceedings, 303
- Courvoisier, T. J.-L. 1998, *Astron. Astrophys. Rev.*, 9, 1
- Courvoisier, T. J.-L., Robson, E. I., Blecha, A., et al. 1990, *Astron. Astrophys.*, 234, 73
- Czerny, B. & Elvis, M. 1987, *Astrophys. J.*, 321, 305

- Dickey, J. M. & Lockman, F. J. 1990, *Ann. Rev. Astron. Astrophys.*, 28, 215
- Dietrich, M., Wagner, S. J., Courvoisier, T. J.-L., Bock, H., & North, P. 1999, *Astron. Astrophys.*, 351, 31
- Edge, D. O., Shakeshaft, J. R., McAdam, W. B., Baldwin, J. E., & Archer, S. 1959, *Mem. R. Astron. Soc.*, 68, 37
- Fanaroff, B. L. & Riley, J. M. 1974, *Mon. Not. R. Astron. Soc.*, 167, 31P
- Fang, T., Sembach, K. R., & Canizares, C. R. 2003, *Astrophys. J.*, 586, 49
- Freedman, W. L., Be, A., Be, A., et al. 2001, *Astrophys. J.*, 553, 47
- Friedman, H. & Byram, E. T. 1967, *Astrophys. J.*, 147, 399
- Grandi, P., Guainazzi, M., Mineo, T., et al. 1997, *Astron. Astrophys.*, 325, L17
- Greenstein, J. L. & Schmidt, M. 1964, *Astrophys. J.*, 140, 1
- Haardt, F., Fossati, G., Celotti, A., et al. 1998, *Astron. Astrophys.*, 340, 35
- Hazard, C., MacKey, M. B., & Shimmins, A. J. 1963, *Nature*, 197, 1037
- Heap, S. R. & Williger, G. M. 2002, in *Extragalactic Gas at Low Redshift*, ed. J. S. Mulchaey & J. Stocke, Vol. 254, *ASP Conference Proceedings*, 63
- Hughes, P. A., Aller, H. D., & Aller, M. F. 1991, *Astrophys. J.*, 396, 469
- Jester, S., Röser, H.-J., Meisenheimer, K., & Perley, R. 2002, *Astron. Astrophys.*, 385, L27
- Jester, S., Röser, H.-J., Meisenheimer, K., Perley, R., & Conway, R. 2001, *Astron. Astrophys.*, 373, 447
- Johnson, W. N., Dermer, C. D., Kinzer, R. L., et al. 1995, *Astrophys. J.*, 445, 182
- Kataoka, J., Tanihata, C., Kawai, N., et al. 2002, *Mon. Not. R. Astron. Soc.*, 336, 932
- Kellogg, E., Gursky, H., Leong, C., et al. 1971, *Astrophys. J., Lett.*, 165, L49
- Khachikian, E. Y. & Weedman, D. W. 1974, *Astrophys. J.*, 192, 581
- Kirsch, M. 2003, EPIC status of calibration and data analysis, Tech. rep., EPIC Consortium (<http://xmm.vilspa.esa.es/>)
- Kriss, G. A., Davidsen, A. F., Zheng, W., & Lee, G. 1999, *Astrophys. J.*, 527, 683

- Leach, C. M. & McHardy, I. M. 1996, *Mon. Not. R. Astron. Soc.*, 278, 465
- Leach, C. M., McHardy, I. M., & Papadakis, I. E. 1995, *Mon. Not. R. Astron. Soc.*, 272, 221
- Leahy, D. A., Darbro, W., Elsner, R. F., et al. 1983, *Astrophys. J.*, 266, 160
- Lichti, G. G., Balonek, T., Courvoisier, T. J.-L., et al. 1995, *Astron. Astrophys.*, 298, 711
- Marscher, A. P. & Gear, W. K. 1985, *Astrophys. J.*, 298, 114
- McHardy, I., Lawson, A., Newsam, A., et al. 1999, *Mon. Not. R. Astron. Soc.*, 310, 571
- McNaron-Brown, K., Johnson, W. N., Dermer, C. D., & Kurfess, J. D. 1997, *Astrophys. J.*, 474, L85
- Minkowski, R. 1960, *Astrophys. J.*, 132, 908
- Miyamoto, S., Kimura, K., Kitamoto, S., Dotani, T., & Ebisawa, K. 1991, *Astrophys. J.*, 383, 784
- Molendi, S. & Sembay, S. 2003, Assessing the EPIC spectral calibration in the hard band with a 3C273 observation, Tech. rep., EPIC Consortium, (<http://xmm.vilspa.esa.es/>)
- Montigny, C. v., Aller, H., Aller, M., et al. 1997, *Astrophys. J.*, 483, 161
- Mould, J. R., Huchra, J. P., Freedman, W. L., et al. 2000, *Astrophys. J.*, 529, 786
- Neumann, M., Meisenheimer, K., & Röser, H.-J. 1997, *Astron. Astrophys.*, 326, 69
- Orr, A., Yaqoob, T., Parmar, A. N., et al. 1998, *Astron. Astrophys.*, 337, 685
- Osterbrock, D. E. 1993, *Astrophys. J.*, 404, 551
- Page, K. L., Turner, M. J. L., Done, C., et al. 2004, *Mon. Not. R. Astron. Soc.*, 349, 57
- Paltani, S., Courvoisier, T. J.-L., & Walter, R. 1998, *Astron. Astrophys.*, 340, 47
- Peterson, B. M. 1997, *An introduction to active galactic nuclei* (Cambridge University Press)
- Pflüger, B., Otterbein, K., & Staubert, R. 1996, *Astron. Astrophys.*, 305, 699

- Pottschmidt, K. 2002, PhD thesis, IAA, Universität Tübingen
- Protassov, R., van Dyk, D. A., Connors, A., Kashyap, V. L., & Siemiginowska, A. 2002, *Astrophys. J.*, 571, 545
- Romero, G. E., Chajet, L., Abraham, Z., & Fan, J. H. 2000, *Astron. Astrophys.*, 360, 57
- Röser, H.-J., Meisenheimer, K., Neumann, M., Conway, R., & Perley, R. 2000, *Astron. Astrophys.*, 360, 99
- Rybicki, G. B. & Lightman, A. P. 1979, *Radiative Processes in Astrophysics* (John Wiley & Sons, New York)
- Sambruna, R. M., Urry, C. M., Tavecchio, F., et al. 2001, *Astrophys. J.*, 549, L161
- Scargle, J. D. 1982, *Astrophys. J.*, 263, 835
- Schmidt, M. 1963, *Nature*, 197, 1040
- Seyfert, C. K. 1943, *Astrophys. J.*, 97, 28
- Shields, G. A. 1978, *Nature*, 272, 706
- Simonetti, J. H., Cordes, J. M., & Heeschen, S. S. 1985, *Astrophys. J.*, 296, 46
- Spergel, D. N., Verde, L., Komatsu, H. V. P. E., et al. 2003, *Astrophys. J., Suppl. Ser.*, 148, 175
- Stark, A. A., Gammie, C. F., Wilson, R. W., et al. 1992, *Astrophys. J., Suppl. Ser.*, 79, 77
- Staubert, R. 1992, in *X-ray Emission from Active Galactic Nuclei and the Cosmic X-ray Background*, MPI für Extraterrestrische Physik, 42–49
- Staubert, R., Fink, H., Courvoisier, T. J.-L., et al. 1992, in *Testing the AGN Paradigm*, ed. S. Hold & S. Neff, Vol. 254, AIP Conference Proceedings, 366–369
- Türler, M., Courvoisier, T. J.-L., & Paltani, S. 1999a, *Astron. Astrophys.*, 349, 45
- Türler, M., Courvoisier, T. J.-L., & Paltani, S. 2000, *Astron. Astrophys.*, 361, 850
- Türler, M., Paltani, S., Courvoisier, T. J.-L., et al. 1999b, *Astron. Astrophys. Suppl. Ser.*, 134, 89
- Turner, M. J. L., Courvoisier, T., Staubert, R., Molteni, D., & Trümper, J. 1985, *Space Sci. Rev.*, 40, 623

- Turner, M. J. L., Williams, O. R., Courvoisier, T. J.-L., et al. 1990, *Mon. Not. R. Astron. Soc.*, 244, 310
- Walter, R. 1994, *Astrophys. J., Suppl. Ser.*, 92, 619
- Walter, R. & Courvoisier, T. J.-L. 1992, *Astron. Astrophys.*, 258, 255
- Wilkes, B. J., Elvis, M. S., McDowell, J., Masnou, J.-L., & Arnaud, K. A. 1989, *Bull. Am. Astron. Soc.*, 21, 1225
- Williams, O. R., Bennett, K., Bloemen, H., et al. 1995, *Astron. Astrophys.*, 298, 33
- Wilms, J., Nowak, M. A., Dove, J. B., Fender, R. P., & Matteo, T. D. 1999, *Astrophys. J.*, 522, 460
- Wilson, A. S. & Baldwin, J. A. 1989, *Astron. J.*, 98, 2056
- Worrall, D. M., Mushotzky, R. F., Boldt, E. A., Holt, S. S., & Serlemitsos, P. J. 1979, *Astrophys. J.*, 232, 683
- XMM-PS-GM-14. 2003, *XMM-Newton Users' Handbook*, 2nd edn., XMM-Newton Science Operations Team
- Yaqoob, T. & Serlemitsos, P. 2000, *Astrophys. J., Lett.*, 544, 95
- Yaqoob, T., Serlemitsos, P., Mushotzky, R., et al. 1994, *Publ. Astron. Soc. Jpn.*, 46, L49

Acknowledgements

I thank Prof. Dr. Rüdiger Staubert for his offer to write a thesis in his working group, his support, the many helpful discussions and his patience. Many thanks also to Jörn Wilms, Katja Pottschmidt, Sarah Benlloch-Garçia, Ingo Kreykenbohm, Markus Kuster and Eckart Göhler for their assistance in the RXTE and XMM-*Newton* data reduction and scientific analyses.

Furthermore I thank the IBIS team, '*Chefe*' Reiner Volkmer, Eckard Kendziorra, Eckart Göhler, Claus Dreischer, Nikolai von Krusenstiern, Oliver Decker, Manfred Grünwald, Sarah Benlloch-Garçia and Jürgen Barnstedt for the very good team work in good and hard times as well as for the special project documentation sessions. Most of all I thank my office mate Eckard Göhler for his friendship and his continuous help for my daily (computer) problems.

I also thank all the institute members for the unique work climate with the 'Espresso-runde', the soccer team, the tennis players and many great LAN- and 'Schnitzel'-parties.

Many thanks to Prof. Dr. T. J.-L. Courvoisier for his invitation to the INTEGRAL Science Data Center in Geneva and for the scientific discussions about 3C 273. It was a great pleasure for me to see INTEGRAL working in space and to stay some months at this very nice place.

Finally I thank my parents for enabling me the study of physics and astronomy. Especially I thank my wife for proofreading my thesis, her support and for encouraging me during the hard times.

Curriculum vitae

Personal Data:

30.12.1970 born in Pforzheim as son of Gudrun Stuhlinger, née Schöttle,
and Hans-Andreas Stuhlinger

School:

1977–1981 Arlinger Grundschule, Pforzheim
1981–1990 Theodor–Heuss Gymnasium, Pforzheim
11.05.1990 Abitur

Civil service:

06.1990–08.1991 Labour Welfare, Pforzheim

Study:

10.1992–02.1999 Physics (Diplom), Eberhard–Karls–Universität Tübingen
22.09.1995 Vordiplom
11.02.1999 University diploma in physics (Dipl.–Phys.)
Diplom thesis at the Institut für Astronomie und Astro-
physik Tübingen (IAAT) on the subject: *Die Echtzeit–*
Datenverarbeitung des IBIS–Experiments auf INTEGRAL, su-
pervisor: Prof. Dr. R. Staubert
03.1999–09.2004 PhD thesis at IAAT on the subject: *Analyses of quasar 3C 273*
using XMM–Newton and RXTE, supervisor: Prof. Dr. R.
Staubert
08.2000 ASA (Austrian Space Agency) summer school *Extragalactic As-*
tronomy & Cosmology from Space, Alpbach, Austria
07.2001 NEON (Network of European Observatories in the North) sum-
mer school at Observatoire de Haute–Provence, France

Profession:

- 01.1992–09.1992 Worker, postman and truck driver at German Federal Mail, Pforzheim
- 03.1999–03.2004 Scientific employee at IAAT
- 05.2004–08.2004 Scientific employee at INTEGRAL Science Data Center, University of Geneva, Switzerland

Academic instructors:

M. Bässgen, M. Baumann, H. Clement, T. J.-L. Courvoisier, A. Fäßler, H. Fischer, K.-H. Gaukler, W.-D. Hartmann, R. Hübener, H. Kaul, D. Kern, O. Lutz, H. Mauder, G. Mertens, H. Müther, W. Nakel, H. Pfister, E. Plies, R. Schief, A. Schwenk, R. Staubert, G. Staudt, G. Wagner, K. Werner, J. Wilms, M. Wolff